

MINIMIZING TASK-SPECIFIC UNCERTAINTY IN CMM-BASED FREEFORM
OPTICS METROLOGY

by

Michael Uwakwe

A dissertation submitted to the faculty of
The University of North Carolina at Charlotte
in partial fulfillment of the requirements
for the degree of Doctor of Philosophy in
Optical Science and Engineering

Charlotte

2018

Approved by:

Dr. Christopher Evans

Dr. Angela Davies

Dr. Jimmie Miller

Dr. Matt Davies

Dr. Shaozhong Deng

©2018
Michael Uwakwe
ALL RIGHTS RESERVED

ABSTRACT

MICHAEL UWAKWE. Minimizing Task-Specific Uncertainty in CMM-Based Freeform Optics Metrology. (Under the direction of DR. CHRISTOPHER EVANS)

Measurements of surface form involve a comparison between the form of the test surface and a reference. In coordinate measuring machine (CMM) measurements, this reference is the machine geometry. The measurement results typically show a height map representation of the test surface but these contain machine error contributions. This research demonstrates and applies an in-situ self-calibration technique, Shift-Rotation, to CMM-based freeform optics metrology. This technique minimizes task-specific uncertainty by separating machine error contributions from test surface measurements.

Simulations were used to demonstrate the error separation of freeform measurements into components of the test surface and machine error contributions. Simulations also estimated uncertainties associated with applying the Shift-Rotation technique; these were Monte Carlo simulations that evaluated standard uncertainty contributions from potential sources inherent in the shift- and rotation-measurement process.

The Shift-Rotation technique was experimentally validated by measuring a freeform surface on a Zeiss F-25 micro-CMM and a Mahr MarSurf LD 260 surface profiler. Error separations of these measurement results led to best estimates of the freeform surface, without machine error contributions. Zernike coefficients of these best estimates from the tactile machines were compared to those from optical measurements of the same freeform surface. The optical measurements were from a Zygo Verifire Fizeau interferometer and a Zygo NexView Scanning White Light interferometer.

DEDICATION

To my mother, Irene Uwakwe, for her unconditional support and encouragement.

ACKNOWLEDGMENTS

My deepest gratitude goes to my adviser, Dr. Christopher Evans, for his guidance, support, and patience throughout this research. I am especially grateful for his generosity of knowledge and understanding, and his encouragement and patience while I learned at my pace. It has been a great privilege learning from him over the years.

I would like to thank my committee members, Dr. Angela Davies, Dr. Jimmie Miller, Dr. Matt Davies, and Dr. Shaozhong Deng for their input, encouragement, and for accepting to be part of my committee.

I would like to thank the Department of Physics and Optical Science, and the Center for Precision Metrology (CPM) at UNC Charlotte for providing research and experimental support in the form of laboratories, equipment, faculty and staff. I would also like to thank the Center for Freeform Optics (CeFO) for providing me the many opportunities to present this research and meet their faculty and affiliates.

I am very thankful for the National Science Foundation's sponsorship of this project, under NSF Award No. 1432990. I am also very thankful for the Graduate Assistant Support Plan (GASP) award from the graduate school at UNC Charlotte.

I would like to thank Mr. Greg Caskey for the CMM and optical measurements and for his support over the years. My gratitude also goes to Dr. William Kuhn for his explanations of the design matrix described in his patent. I am also very thankful for all the support I received from Mr. Mark Clayton and Mrs. Jennifer Chastain throughout this research.

Lastly, I would like to thank my siblings, Charles and Jennifer, for their humor, encouragement and always being there.

TABLE OF CONTENTS

LIST OF TABLES	x
LIST OF FIGURES	xi
LIST OF ABBREVIATIONS.....	xx
CHAPTER 1: INTRODUCTION	1
1.1 Freeform Surfaces	1
1.2 Freeform Surface Metrology.....	3
1.3 Motivation.....	7
1.4 Layout of the Dissertation.....	10
CHAPTER 2: SIMULATIONS OF THE SHIFT-ROTATION TECHNIQUE	11
2.1 Separation of the Rotationally Varying Components	15
2.2 Separation of the Rotationally Invariant Components.....	20
2.2.1 A Way around the Singularity of the Design Matrix	24
2.3 Separation of the Rotationally Invariant Components continued	30
2.4 Part Measurement without Machine Error Contributions.....	31
2.5 A More Robust Rotationally Invariant Solution.....	33
2.6 Influence of Random Machine Z-axis Errors on the Error Separation Process.....	37
2.6.1 Influence of 10% Random Machine Z-axis Errors	38
2.6.2 Summary of the Influences of Random Machine Errors	42

2.7 Summary	44
CHAPTER 3: MONTE CARLO UNCERTAINTY ESTIMATIONS	46
3.1 Uncertainty from the Rotation Angles	50
3.2 Uncertainty from a Moving Axis of Rotation.....	53
3.3 Uncertainty from the Translation Distance.....	56
3.4 Uncertainty from Electronic Noise and Vibrations	58
3.5 A Combined Standard Uncertainty.....	60
3.6 Summary	63
CHAPTER 4: ERROR SEPARATION OF MID-SPATIAL FREQUENCIES	64
4.1 Error Separation of Sinusoidal Mid-Spatial Frequency Errors.....	66
4.2 Error Separation of On-Axis Circular Mid-Spatial Frequency Errors.....	72
4.3 Error Separation of Off-Axis Circular Mid-Spatial Frequency Errors	77
4.4 Error Separation of Crosshatch Mid-Spatial Frequency Errors	82
4.5 Summary	86
CHAPTER 5: FREEFORM SURFACE MEASUREMENTS	87
5.1 The Freeform Surface to be Measured.....	88
5.1.1 Four Different Machines to Measure the Freeform Surface	89
5.2 Measurement of the Freeform Surface on the Zygo Fizeau Interferometer	90
5.3 Measurements of the Freeform Surface on the Zeiss F-25 CMM	91
5.3.1 Error Separations of the Rotationally Varying Components	95

5.3.2 Error Separations of the Rotationally Invariant Components	101
5.3.3 Best Estimate of the Freeform Surface from the Zeiss F-25	104
5.3.4 Uncertainty Estimations in the Best Estimate from the CMM	105
5.4 Measurements of the Freeform Surface on the Mahr Surface Profiler	108
5.4.1 Stages, Mounts and Fixtures that Maneuver the Freeform Part.....	108
5.4.2 Error Separations of the Rotationally Varying Components	111
5.4.3 Error Separations of the Rotationally Invariant Components.....	115
5.4.4 Best Estimate of the Freeform Surface from the Mahr LD 260	118
5.4.5 Uncertainty Estimations in the Best Estimate from the Mahr profiler	119
5.5 Measurement of the Freeform Surface on the Zygo NexView Interferometer.....	122
5.6 Comparisons between Freeform Measurements made on the Four Machines	123
5.7 Summary	125
CHAPTER 6: CONCLUSIONS AND FUTURE WORK.....	126
6.1 Conclusions.....	126
6.2 Future Work	129
6.2.1 A More Robust Noise-Modification of a Singular Matrix.....	129
6.2.2 Filtering Effect of Probe-Ball Radius	129
REFERENCES	130
APPENDIX A: FLOWCHART OF THE SHIFT-ROTATION TECHNIQUE	137
APPENDIX B: INFLUENCE OF RANDOM MACHINE Z-AXIS ERRORS	140

APPENDIX B.1 Influence of 1% Random Machine Z-axis Errors.....	140
APPENDIX B.2 Influence of 0.1% Random Machine Z-axis Errors.....	144
APPENDIX B.3 Influence of 0.01% Random Machine Z-axis Errors.....	148
APPENDIX C: ERROR SEPARATION OF ON-AXIS MSF ERRORS.....	151
APPENDIX D: ALTERNATE MEASUREMENT STRATEGY ON THE MAHR	156
APPENDIX D.1 Measurement Results	158
APPENDIX E: MATLAB CODES	162

LIST OF TABLES

TABLE 2.1:	Zernike terms, up to the 4 th order.	12
TABLE 2.2:	Linear system relationship between the slope profile (g) and the desired radial profile (f).	23
TABLE 2.3:	Effects of added random z-axis machine errors on separated surface components.	42
TABLE 3.1:	Potential sources of uncertainty associated with the Shift-Rotation process.	48
TABLE 5.1:	Zernike coefficients from the Fizeau measurement of the freeform surface.	91
TABLE 5.2:	Zernike coefficients of the Zernike fit to the corrected profiles (F-25 freeform measurement of the part in the initial position/orientation).	95
TABLE 5.3:	Zernike coefficients from the F-25 freeform surface measurements of the part in five angular orientations.	97
TABLE 5.4:	Zernike coefficients from a Zernike polynomial fit to the best estimate of the freeform surface.	104
TABLE 5.5:	Zernike coefficients from the Mahr LD 260 freeform surface measurements of the part in five angular orientations.	112
TABLE 5.6:	Zernike coefficients from a Zernike polynomial fit to the best estimate of the freeform surface.	118
TABLE 5.7:	Zernike coefficients of the NexView freeform measurement.	122
TABLE 5.8:	Zernike coefficients of the freeform measurement results from the four instruments.	124
TABLE 5.9:	Amplitude Zernike coefficients of the freeform surfaces from the four instruments.	124
TABLE D.1	Zernike coefficients from a Zernike fit to the 10 Polar-model profiles.	160

LIST OF FIGURES

FIGURE 2.1	Zernike aberration representations of the simulated test surface components and machine errors.	14
FIGURE 2.2	A simulated measurement of a freeform surface containing the part, as well as error contributions from the machine.	15
FIGURE 2.3	Simulated measurements after rotations of the freeform part.	16
FIGURE 2.4	An average of the four rotated part measurements.	17
FIGURE 2.5	The separated rotationally varying component of the freeform part.	17
FIGURE 2.6	Simulated measurements depicting rotations of the machine's RV errors.	18
FIGURE 2.7	Average of the height maps that depict machine rotations.	19
FIGURE 2.8	The separated rotationally varying component of the machine's errors.	20
FIGURE 2.9	Simulated measurement of the part in an initial position (<i>left</i>). Simulated measurement after the part was shifted 2 mm to the left (<i>right</i>).	21
FIGURE 2.10	The slope of the freeform part, evaluated after a 2-mm lateral translation.	22
FIGURE 2.11	Comparison between a pseudo-inverse output RI part and the output RI part from a noise-modified design matrix.	28
FIGURE 2.12	Difference between a Moore-Penrose output and the input RI component of the part (<i>left</i>). Difference between a noise-modified design matrix output and the input RI component of the part (<i>right</i>).	29
FIGURE 2.13	Radial profile of the rotationally invariant freeform surface.	30
FIGURE 2.14	The rotationally invariant component of the freeform part.	30
FIGURE 2.15	The rotationally invariant component of the machine errors.	31

FIGURE 2.16	Separation of the simulated freeform surface into its four constituent components.	32
FIGURE 2.17	A measurement of the freeform surface, without the RV and RI machine errors.	32
FIGURE 2.18	The task-specific machine error contributions.	33
FIGURE 2.19	Simulated measurement of the part in an initial position (<i>left</i>). Simulated measurement after the part was shifted 20 mm to the left (<i>right</i>).	34
FIGURE 2.20	Slope of the part, evaluated after a 20-mm lateral translation.	34
FIGURE 2.21	Radial profile of the part, obtained after a large translation distance of 20 mm (<i>left</i>). The RI component of the part, generated from this profile (<i>right</i>).	35
FIGURE 2.22	Improved radial profile of the part, obtained from simulated part measurements after 20 mm, 23 mm and 25 mm translations (<i>left</i>). The RI component of the part, generated from this profile (<i>right</i>).	35
FIGURE 2.23	Input minus output RI part components, after a 2-mm translation of the part (<i>left</i>). Input minus output RI part components, after multiple part-translations of 20-mm, 23-mm, and 25-mm (<i>middle</i>). A difference between the output P_{RI} solutions from single and multiple part-translations (<i>right</i>).	36
FIGURE 2.24	Simulated systematic machine errors (<i>left</i>). The machine's systematic errors with a random component in the z-direction; the random errors have a maximum amplitude of 10% the nominal systematic error. (<i>right</i>).	38
FIGURE 2.25	Input components to the Shift-Rotation technique (<i>left</i>). Output components obtained after the addition of random z-axis machine errors with maximum amplitudes of 10% deviation from the nominal (<i>right</i>).	40
FIGURE 2.26	Differences between output and input surface components, after the addition of 10% random machine z-axis errors.	41
FIGURE 2.27	Effects of added random z-axis machine errors on separated surface components.	43

FIGURE 3.1	Propagation of uncertainty, through the measurement model, to the output.	49
FIGURE 3.2	A flowchart of the Monte Carlo process, with rotation angle as the input parameter.	51
FIGURE 3.3	The convergence of the Monte Carlo to the freeform part height map (<i>left</i>). The uncertainty in the best estimate measurement, because of an uncertainty in the rotation angles (<i>right</i>).	52
FIGURE 3.4	Amplitude parametric representation of the 1,000 trials in the Monte Carlo, reported as: $\text{rms} = 5.7001 \pm 0.00003 \text{ mm (k} = 2\text{)}$.	53
FIGURE 3.5	Depictions showing rotations of the part about a moving axis of rotation.	54
FIGURE 3.6	Depiction of the freeform part allowed to translate randomly within a 300 μm square region (3-pixel square).	55
FIGURE 3.7	The convergence of the Monte Carlo to the estimated measurement of the freeform part, because of an uncertainty in the axis of rotation (<i>left</i>). The uncertainty in the best estimate measurement, because of an uncertainty in the axis of rotation (<i>right</i>).	56
FIGURE 3.8	Uniform distribution around the translation distance.	57
FIGURE 3.9	The convergence of the Monte Carlo to the estimated measurement of the freeform part, because of an uncertainty in the translation distance (<i>left</i>). The uncertainty in the best estimate measurement, because of an uncertainty in the translation distance (<i>right</i>).	57
FIGURE 3.10	Monte Carlo convergence from 100 trials with nominal input parameters (<i>left</i>). Intrinsic noise present in the Monte Carlo software, obtained from the 100 trials (<i>right</i>).	58
FIGURE 3.11	A simulation of electronic noise to be added to the Monte Carlo simulations.	59
FIGURE 3.12	Monte Carlo convergence after the addition of 30 nm P-V random noise to the input parameters (<i>left</i>). The output noise because of the random 30-nm P-V input noise (<i>right</i>).	59

FIGURE 3.13	Output noise from the RV portion of the Monte Carlo software.	60
FIGURE 3.14	The best estimate of the freeform surface (<i>left</i>), and its standard uncertainties (<i>right</i>).	61
FIGURE 3.15	The best estimate of the freeform surface (<i>left</i>) and its combined standard uncertainty (<i>right</i>).	62
FIGURE 4.1	Separation of a profile into frequency bands.	64
FIGURE 4.2	The freeform surface simulated with low-spatial frequency surface components.	65
FIGURE 4.3	The PSD of a profile from the simulated freeform surface.	65
FIGURE 4.4	A simulated sinusoidal mid-spatial frequency error (<i>left</i>). The simulated freeform surface, without mid-spatial frequency errors (<i>right</i>).	66
FIGURE 4.5	The freeform surface with a sinusoidal mid-spatial frequency error.	67
FIGURE 4.6	The power spectral density of the central horizontal profile, extracted from the simulated freeform surface with sinusoidal mid-spatial frequency errors.	67
FIGURE 4.7	The simulated freeform surface with sinusoidal mid-spatial frequency errors (<i>left</i>). The Shift-Rotation separation of the freeform into four components (<i>right</i>).	69
FIGURE 4.8	Sinusoidal mid-spatial frequency error (<i>left</i>). The Shift-Rotation separation of the mid-spatial frequency error, into rotationally varying, rotationally invariant, and residual components (<i>right</i>).	71
FIGURE 4.9	A simulated rotationally invariant mid-spatial frequency error (<i>left</i>). The simulated freeform surface without mid-spatial frequency errors (<i>right</i>).	72
FIGURE 4.10	The simulated freeform with on-axis circular mid-spatial frequency errors.	72
FIGURE 4.11	The power spectral density of the central horizontal profile extracted from the freeform surface with on-axis circular mid-spatial frequency errors.	73
FIGURE 4.12	The simulated freeform surface with on-axis circular	

	mid-spatial frequencies (<i>left</i>). The Shift-Rotation separation of the freeform into four components (<i>right</i>).	74
FIGURE 4.13	Simulated on-axis circular mid-spatial frequency errors (<i>left</i>). The Shift-Rotation separation of the circular mid-spatial frequency errors into rotationally varying, rotationally invariant, and residual components (<i>right</i>).	76
FIGURE 4.14	A simulated off-axis circular mid-spatial frequency error with multiple frequencies and amplitudes (<i>left</i>). The simulated freeform surface without mid-spatial frequency errors (<i>right</i>).	77
FIGURE 4.15	The simulated freeform surface with off-axis circular mid-spatial frequency errors.	78
FIGURE 4.16	The freeform surface with off-axis circular mid-spatial frequencies (<i>left</i>). Shift-Rotation error separation of the freeform into four components (<i>right</i>).	79
FIGURE 4.17	Off-axis circular mid-spatial frequency errors (<i>left</i>). Shift-Rotation separation of the mid-spatial frequency errors, into rotationally varying, rotationally invariant, and residual components (<i>right</i>).	81
FIGURE 4.18	A Blanchard ground part showing a crosshatch pattern.	82
FIGURE 4.19	A simulated crosshatch mid-spatial frequency error (<i>left</i>). The simulated freeform surface without mid-spatial frequency errors (<i>right</i>).	82
FIGURE 4.20	The simulated freeform surface with crosshatch mid-spatial frequency error.	83
FIGURE 4.21	The simulated freeform surface with crosshatch mid-spatial frequencies (<i>left</i>). The Shift-Rotation error separation of the freeform into four components (<i>right</i>).	84
FIGURE 4.22	Crosshatch mid-spatial frequency errors (<i>left</i>). Shift-Rotation separation of the mid-spatial frequency errors, into rotationally varying, rotationally invariant, and residual components (<i>right</i>).	85
FIGURE 5.1	The freeform surface to be measured.	88
FIGURE 5.2	Four machines to measure the freeform surface.	90

FIGURE 5.3	A Fizeau measurement of the freeform surface.	91
FIGURE 5.4	Cartesian measurement strategy employed on the Zeiss F-25 CMM.	92
FIGURE 5.5	Profiles scanned across the freeform surface, measured on the F-25 CMM with the part in an initial position/orientation.	93
FIGURE 5.6	Low-pass filtered, cropped, and slope-corrected profiles from the first set of F-25 CMM measurements.	94
FIGURE 5.7	F-25 CMM freeform measurement of the part in the initial position.	95
FIGURE 5.8	F-25 CMM freeform measurements of the part at five angular orientations.	96
FIGURE 5.9	An average of the F-25 measurements of the freeform surface at the five angular orientations.	98
FIGURE 5.10	The separated rotationally varying component of the freeform surface.	98
FIGURE 5.11	N-Rotations to extract the machine's rotationally varying error contributions.	99
FIGURE 5.12	Average of the height maps that depict machine rotations. This average drops out the rotationally varying components of the machine errors.	100
FIGURE 5.13	The separated rotationally varying component of the machine's errors.	100
FIGURE 5.14	Measurement of the freeform surface in an initial position (<i>left</i>). Measurement after the part was shifted upwards by 1 mm (<i>right</i>).	101
FIGURE 5.15	The slope of the freeform part evaluated after a 1-mm lateral translation.	102
FIGURE 5.16	The solved radial profile of the rotationally invariant component of the freeform surface.	103
FIGURE 5.17	The solved rotationally invariant component of the freeform surface (<i>left</i>). The solved rotationally invariant component of the machine error contributions (<i>right</i>).	103

FIGURE 5.18	Best estimate of the freeform surface, separated from the Zeiss F-25 measurement results.	104
FIGURE 5.19	Best estimate of the freeform from F-25 measurements (<i>left</i>). Its standard uncertainties (<i>right</i>).	106
FIGURE 5.20	The best estimate of the freeform surface from F-25 measurements (<i>left</i>) and its combined standard uncertainty ($k = 2$) (<i>right</i>).	107
FIGURE 5.21	The MarSurf LD 260 surface profiler with the affixed rotary stage.	109
FIGURE 5.22	The arrangement of the cylindrical pairs (<i>top left</i>) and spheres (<i>top right</i>) of the kinematic mount. The assembled kinematic mount (<i>bottom</i>).	109
FIGURE 5.23	The x-y translation stage fastened to a kinematic mount.	110
FIGURE 5.24	Assembly of the freeform part, translation stage, and rotary stage on the Mahr surface profiler.	111
FIGURE 5.25	Mahr LD 260 freeform measurements of the part at five angular orientations.	112
FIGURE 5.26	An average of the Mahr LD 260 freeform surface measurements at the five angular orientations.	113
FIGURE 5.27	The separated rotationally varying component of the freeform surface.	113
FIGURE 5.28	N-Rotations to extract the machine's rotationally varying error contributions.	114
FIGURE 5.29	Average of the height maps that depict machine rotations. This average drops out the rotationally varying components of the machine errors.	114
FIGURE 5.30	The separated rotationally varying component of the machine's errors.	115
FIGURE 5.31	Measurement of a profile on the freeform surface in an initial position (<i>top</i>). Measurement after the freeform part was shifted 1-mm to the left (<i>right</i>).	116
FIGURE 5.32	The slope of the freeform surface evaluated after a 1-mm	

	lateral translation.	116
FIGURE 5.33	The solved rotationally invariant component of the freeform surface (<i>left</i>). The solved rotationally invariant component of the machine error contributions (<i>right</i>).	117
FIGURE 5.34	Best estimate of the freeform surface separated from the Mahr LD 260 measurement results.	118
FIGURE 5.35	Best estimate of the freeform from the Mahr LD 260 measurements (<i>left</i>). Its standard uncertainties (<i>right</i>).	120
FIGURE 5.36	The best estimate of the freeform surface from Mahr LD 260 measurements (<i>left</i>) and its combined standard uncertainty ($k = 2$) (<i>right</i>).	121
FIGURE 5.37	A NexView measurement of the freeform surface.	122
FIGURE 5.38	Freeform surface measurements from four measuring instruments.	123
FIGURE B.1	Simulated systematic machine errors (<i>left</i>). The machine's systematic errors with a random component in the z-direction. The random errors have a maximum amplitude of 1% the nominal systematic error (<i>right</i>).	140
FIGURE B.2	Input components to the Shift-Rotation technique (<i>left</i>). Output components obtained after the addition of random z-axis machine errors with maximum amplitudes of 1% deviation from the nominal (<i>right</i>).	142
FIGURE B.3	Differences between output and input surface components, after the addition of 1% random machine z-axis errors.	143
FIGURE B.4	Simulated systematic machine errors (<i>left</i>). The machine's systematic errors with a random component in the z-direction. The random errors have a maximum amplitude of 0.1% the nominal systematic error (<i>right</i>).	144
FIGURE B.5	Input components to the Shift-Rotation technique (<i>left</i>). Output components obtained after the addition of random z-axis machine errors with maximum amplitudes of 0.1% deviation from the nominal (<i>right</i>).	146
FIGURE B.6	Differences between output and input surface components after the addition of 0.1% random machine z-axis errors.	147

FIGURE B.7	Simulated systematic machine errors (<i>left</i>). The machine's systematic errors with a random component in the z-direction. The random errors have a maximum amplitude of 0.01% the nominal systematic error (<i>right</i>).	148
FIGURE B.8	Input components to the Shift-Rotation technique (<i>left</i>). Output components obtained after the addition of random z-axis machine errors with maximum amplitudes of 0.01% deviation from the nominal (<i>right</i>).	149
FIGURE B.9	Differences between output and input surface components, after the addition of 0.01% random machine z-axis errors.	150
FIGURE C.1	A simulated on-axis circular mid-spatial frequency error comprised of multiple frequencies and amplitudes (<i>left</i>). The simulated freeform surface without mid-spatial frequency errors (<i>right</i>).	151
FIGURE C.2	The simulated freeform surface with multi-frequency circular mid-spatial frequency errors.	152
FIGURE C.3	The power spectral density of the central horizontal profile extracted from the freeform surface with multi-frequency circular mid-spatial frequency errors.	152
FIGURE C.4	The freeform surface with multi-frequency circular mid-spatial frequencies (<i>left</i>). The Shift-Rotation separation of the freeform into four components (<i>right</i>).	153
FIGURE C.5	Multi-frequency circular mid-spatial frequency errors (<i>left</i>). The Shift-Rotation separation of the mid-spatial frequency errors, into rotationally varying, rotationally invariant, and residual components (<i>right</i>).	155
FIGURE D.1	Freeform surface measurement strategy on a Mahr surface profiler.	156
FIGURE D.2	Polar-model freeform surface profiles measured on the Mahr surface profiler.	159
FIGURE D.3	Azimuthal profile measured to correct for tilt.	160
FIGURE D.4	Surface fit to the 10 Polar-model profiles measured on the Mahr profiler.	161

LIST OF ABBREVIATIONS

CAD	computer-aided drawing
CGH	computer-generated hologram
CMM	coordinate measuring machine
M_{RI}	rotationally invariant component of the machine
M_{RV}	rotationally varying component of the machine
MSF	mid-spatial frequency
PDF	probability density function
P_{RI}	rotationally invariant component of the part
P_{RV}	rotationally varying component of the part
PSD	power spectral density
PV	peak-to-valley
PV_T	robust peak-to-valley
RI	rotationally invariant
RMS	root mean square
RV	rotationally varying
SWLI	scanning white-light interferometer
U_C	combined standard uncertainty
VCMM	virtual coordinate measuring machine

CHAPTER 1: INTRODUCTION

1.1 Freeform Surfaces

Conventional optical elements usually have surfaces that are rotationally symmetric, often planar, spherical, or aspheric. These surfaces have axes of rotational symmetry and can be conveniently designed, fabricated, and measured to within tight tolerances. On the other hand, freeform optical surfaces have no axis of rotational symmetry on or outside the surface and can be designed to have any shape [1-4]. Wills (2017) defines a freeform optical surface as “one that lacks translational or rotational symmetry”. In the same paper [5], a freeform surface was mathematically defined as “an optical surface whose surface function requires two variables – angle and radius, for example, or x and y - rather than one”; and went on to state that the definition of a freeform might depend on whom you talk to.

This lack of rotational symmetry gives freeform surfaces a design flexibility which makes them more complicated than their conventional counterparts, but offers several advantages including an improvement in optical quality, and a reduction in size, weight and number of required components [1, 4]. Freeform surfaces were used to improve the optical quality of the Polaroid SX-70 folding Single Lens Reflex camera in 1972 [6]. In that camera, a freeform surface corrected for field tilt, power, and astigmatic errors while a second freeform corrected for coma and spherical aberration.

Another example of a freeform surface was an invention in 1926 that superimposed two or more cylindrical lenses to obtain the effect of a spherical lens, a cylindrical lens, or a combination of spherical and cylindrical lenses with a variable focal power. These superimposed cylindrical lenses were movable longitudinally with respect to one another and had regularly increasing refractive indices across their lengths [7]. Over two decades later, in 1949, another freeform lens of gradually varying focal power was invented to correct for distortion [8]. One surface of the lens had a progressively changing curvature of involute form, along the medial plane of the lens. Almost two decades after this invention, the surface was mathematically described by Luis Alvarez and presented as a two-element variable-power spherical lens which is now known as an Alvarez lens [9]. The lens assembly is composed of two thin lens elements arranged in tandem, with at least one of the lens elements movable in a direction transverse to the optical axis. Multiple design forms requiring variable-focus optics have incorporated the Alvarez lens [10-12]. Smilie, et al. [13] designed a diamond micro-milled germanium Alvarez lens pair and characterized its optical performance in the mid-infrared. A more recent application of the Alvarez lens extended its application from lenses to arbitrary optical devices like tunable gratings and spiral phase plates [14].

For functional or aesthetic reasons, these freeform surfaces play an increasing number of roles in industries such as aerospace, automotive, optics, and medicine [2, 3, 15-17]. This growing demand drives the need to improve the design, manufacture, and performance of the freeform surfaces. These freeform surfaces include freeform optics and freeform mechanical components (like gear teeth, turbine blades, car bodies, compressor scrolls) and these improvements are closely connected to the metrology (the scientific

study of measurements) of the freeform surfaces. Metrology of freeform surfaces plays a vital role because it enhances quality control and process troubleshooting in the design and fabrication stages, but the complexity of freeform surfaces introduces some difficulty to the metrology.

1.2 Freeform Surface Metrology

Optical surfaces comprise a superposition of high-, mid-, and low-spatial frequency components referred to as roughness, waviness, and form error, respectively. Surface metrology includes the measurement of these spatial frequency classifications but this project focuses on form error, rather than mid-spatial frequencies and roughness. Form error measurements of optical surfaces typically involve measurements of flat, spherical, aspheric, or freeform surfaces, and there are different instruments and techniques for making these measurements. Some of these techniques are discussed below. Most of them are well suited to measuring flat and spherical optics, and in many cases, can be extended to the measurement of aspheric surfaces but the difficulty increases as one moves onto freeform surfaces.

A measurement of an optical flat or spherical surface can be obtained after it is matched to the accurate surface of a reference flat or a correspondingly opposite spherical reference surface, respectively. Newton interferometers use this arrangement of two surfaces in contact, illuminated by a short coherence length light source. The thickness of the air gap between the surfaces is usually a few wavelengths of light, and by observing its non-uniformity, interpretations of the surface under test can be obtained [18].

Aspherical surfaces can also be measured by contacting a reference spherical surface with the asphere of nearly the same radius of curvature, then counting the fringes,

provided the pattern is centered [19]. One difficulty in applying this technique to the measurement of freeform surfaces arises from the lack of symmetry on freeform surfaces, which results in decentered fringe patterns. Other potential problems with this test include the availability of the reference surface and its quality, which affects the accuracy of the measurement. Even though calibration techniques like 3-plate test for flat surfaces, 3-position test for spherical surfaces [20], and shift-rotation test for plane and spherical surfaces [21], exist to separate the measurements into system errors and test piece errors, the accuracy could still be limited by the reference surface as well as the calibration procedure [22].

Fizeau and other types of interferometric tests also involve a comparison between the surface under test and a reference surface, but with air gap thicknesses much larger than in the case of the Newton interferometer. These interferometric measurements of aspheric and freeform surfaces are also not as simple as in the case of flat and spherical surfaces.

Interferometric null tests can also be used to measure aspheric surfaces [23]. These use transmissive null optical elements to counteract the asphericity of the test surface and produce a fringe-free (or “null”) field when the aspheric surface meets specification. One drawback is the production of the appropriate transmissive null corrector plate can be as challenging as the fabrication of the actual aspheric test surface [24]. Alternatively, null correction can be achieved using a computer-generated hologram (CGH) [25]. CGH nulls are diffractive optics written by e-beam or laser lithography and yield fringe-free interferograms. They are often simpler to align, can be designed for off-axis segments, and do not become more difficult to produce as more aspheric terms are added. On the other

hand, CGH nulls can produce spurious diffraction orders which should be separated to prevent ghost fringes [26].

Non-null tests also exist for testing aspheric surfaces; these include tests like Foucault, Ronchi or Hartmann tests that mathematically calculate the surface deformation with respect to the closest sphere [18]. These processes are generally time-consuming and the accuracy of the results are frequently not high enough if the aspheric deformation is strong. Some other techniques for measuring aspheric surfaces include wavefront stitching techniques [27-30], two-wavelength holography [31], phase shifting interferometry [32], contact and optical profilometry [33-41].

The techniques discussed above for measuring aspheric and freeform surfaces can broadly be classified into direct and indirect comparisons [15]. The direct comparisons involve measuring the deviations between a freeform surface and a master template. The indirect comparisons do not require master templates but involve comparing measured coordinate points to some reference coordinate points and, implicitly, the quality of the reference coordinate system of the metrology system. This method is based on coordinate measurements and is an approximation technique which represents a continuous profile as discrete surface coordinate points. A measurement of a freeform surface or profile, in this discretized form, can be represented in a Cartesian or polar coordinate system. The difference between this coordinate measurement and a reference coordinate model, then represents the geometrical errors in the freeform surface [42], subject to alignment of the model and the measurement data. The reference coordinate model, which represents the nominal geometry of a freeform surface, is typically defined by a Computer-Aided

Drawing (CAD) model or a prescription based on a mathematical description of the desired surface.

In the indirect comparison method, the most frequently used instruments to measure freeform surface coordinates are coordinate measuring machines (CMM) and profilometers [2, 3, 15, 43, 44]. These instruments are more flexible and have higher measuring speeds than conventional mechanical gauging methods but much slower than full aperture interferometry. They can measure thousands of points across complex freeform surfaces including surface features with high slopes.

In profilometer or CMM measurements of freeform surface coordinates, it is essential to measure a sufficient number of points optimally distributed across the surface. These points can be measured by a point-mode strategy where each data point is obtained after contact is made between the instrument's probe and the surface, or by a scanning-mode strategy where multiple data points are acquired as the probe scans across profiles on the surface. The difference between these measured points and a reference model, represents the geometrical errors in the freeform. The reference model is typically the exact shape or nominal surface topography of the freeform part, but the measured surface coordinates are usually not. This exact surface, or "true value" of the surface coordinates, cannot be known but the closeness of the measured coordinates to the "true" coordinates largely depends on the geometry, operation and condition of the instrument and its probing system. Precision surface measurements estimate the gap between measured surface coordinates and the "true" values of the surface coordinates, and this entails estimations of the errors within the machine. This leads to the need for calibrations of CMMs.

In addition to the uncertainties that arise from random noise in the instruments [45], the uncertainty associated with profilometer or CMM measurements largely depends on the magnitudes of the error sources within the instrument and these error sources can be classified as being geometric or computational [46]. Geometric errors are errors in the measured position of points on the surface and are determined by several factors including the accuracy of the components of the CMM, the environmental conditions around and within the CMM, the probing strategies, and the material characteristics of the workpiece. The computational errors are errors in estimations of the dimensions and form deviations of the workpiece and are determined by the CMM's software and its precision, as well as the number and relative distribution of measured points across the surface. The magnitudes of these CMM errors can be determined from CMM calibrations.

1.3 Motivation

Metrologists investigate CMMs by carrying out calibrations [47]. These CMM calibrations are tasks or tests carried out to determine the magnitudes of all kinematic error sources (twenty-one kinematic error sources for a 3-axis machine) in the machine, and are often referred to as error mapping of the CMM. There are many calibration methods available for evaluating these machine errors [48-52], after which software compensations or error corrections may be carried out to reduce measurement uncertainties. However, these machine errors obtained from direct calibration methods, estimate the machine's errors at the time of calibration, at a point density determined by the time needed to do the calibration, and at an uncertainty appropriate to the general use case of the instrument. During freeform optical surface measurements, the machine errors could be different from

those observed while measuring calibrated artifacts; the direct calibrations give machine error maps that are not specific to the measurement tasks.

In this research, task-specific measurement uncertainty is minimized by applying an in-situ self-calibration technique, known as Shift-Rotation, to freeform surface measurements. Shift-Rotation is an absolute testing procedure developed in interferometric optical surface metrology to separate measurement results into system errors and test piece errors [20, 21, 53-64]. This calibration method requires rotational and translational measurements and relies on the decomposition of surface departures into rotationally varying (RV) and rotationally invariant (RI) components.

The “rotation” portion of the Shift-Rotation technique used in this research is an N-rotation technique used to obtain the RV components of the test surface and reference. It involves measurements of the test surface at N systematically chosen positions (where $N = 2, 3, 4, \dots$) spaced at $360/N$ degree intervals; the average of these measurements reduces to zero all RV components of the test surface except those of order $kN\theta$, where k is an integer [65]. There are also a body of techniques that use incommensurate angles and Fourier techniques to obtain the rotationally varying components. Repeating the N-rotation test at incommensurate angles provides information on errors of angular order $kN\theta$, but this approach requires the errors could be fit to a polynomial in R and θ , although no fitting is done [65].

The “shift” portion of the Shift-Rotation technique involves measurements of the test surface before and after a lateral shift by a known translation distance. A difference between the initial and sheared measurement data leads to the RI components of the test surface and reference errors. The literature shows a variety of ways the shift technique has

been used to obtain the RI components. Song, et al. [55] obtained the RI components by making two translational measurements with different translations in the x and y directions. In a different study [57], the RI component of the test surface was derived from the finite-difference equation of the RI component of the reference surface, after displacing the shifted measurement data back to the original coordinate and canceling out the test surface components. Kuhn [66] solved for the RI component of the test part from a system of linear equations that included the difference between the sheared and initial test part measurements; this difference canceled the measurement system bias and left behind an estimate of the derivative of the test surface.

This research applies this Shift-Rotation calibration technique, which was developed in interferometry, to CMM measurements of freeform surfaces. The machine errors separated by this self-calibration technique are not generic machine errors obtained from measurements of calibrated artifacts but are specific to the measurement task at hand. These task-specific machine errors can be obtained anywhere within the machine's measurement volume. Therefore, with the Shift-Rotation self-calibration, it is unnecessary to directly measure the CMM errors, which include the parametric errors (21 D. o. F for a 3-axis machine). These errors can be obtained on a task-specific basis from a predetermined sequence of rotated and translated freeform part measurements. Also, since this self-calibration method requires stability only over the measurement cycle time, effects of machine drifts are reduced to the timescale of the measurement rather than the interval between machine calibrations.

1.4 Layout of the Dissertation

In Chapter 2, simulations and equations describe and demonstrate the Shift-Rotation error separation process. They detail how surface deviations from measurements of freeform surfaces can be separated into components of the freeform surface, and components which arise from the CMM errors. Also with the aid of simulations, Chapter 3 evaluates task-specific uncertainties associated with applying the Shift-Rotation technique to the measurements of freeform surfaces. The uncertainty evaluations are carried out by using Monte Carlo simulations to evaluate uncertainty contributions from various sources.

The Shift-Rotation technique is primarily applicable to the separation of surface form errors, and not mid-spatial frequencies or roughness; Chapter 4 investigates the technique's error separations of some mid-spatial frequencies. It shows the complete or partial error separations of mid-spatial frequencies, and how mid-spatial frequency errors affect the separation of form errors. Chapter 5 then demonstrates the error separation process, applied to actual freeform surface measurements. Rotational and translational measurements of a freeform surface were carried out on a Zeiss CMM and a Mahr surface profiler. These measurement results were decomposed into RV and RI components of the freeform surface, as well as RV and RI components of the machine error contributions. Estimates of the freeform surface, without machine error contributions, were then deduced and compared.

CHAPTER 2: SIMULATIONS OF THE SHIFT-ROTATION TECHNIQUE

All measurements of surface form involve a comparison between the form of the surface under test, and a reference. In coordinate measuring machine (CMM) measurements, this reference is the machine geometry. The measurement results typically show a height map representation of the test surface, but also contain error contributions from the machine. This Chapter demonstrates simulations of an in-situ self-calibration technique, Shift-Rotation, which minimizes task-specific uncertainty in freeform measurements by separating machine errors from part surface measurements. The discussion here does not differentiate between a classical Cartesian CMM (such as the F-25) or a multi-axis profilometer, such as the Mahr LD-260 with added Y- and/or theta axes as used in this work.

As the name implies, the Shift-Rotation technique comprises two parts: “Shift” and “Rotation”. The “Rotation” portion of the Shift-Rotation technique, stems from an N-rotation method used to solve for rotationally varying (RV) components of a part. These RV components are extracted after averaging the measurement data acquired after multiple predetermined rotations of the part. The “Shift” portion of the technique stems from a lateral shear method that requires part measurements before and after the part has been laterally shifted by a known translation distance. This portion solves for the rotationally invariant (RI) surface components. The “Shift” and the “Rotation” are techniques that have been in use in interferometry for testing optical surfaces [21, 57, 67, 68] and the ideas are here, extended to measurements from CMMs and tactile profilers.

Some potential uncertainty sources are associated with this error separation technique, and these uncertainties can be expressed as maps that show the spatial distribution of the uncertainty within the aperture. Task-specific uncertainty analyses, using Monte Carlo, will be used in Chapter 3 to evaluate these uncertainty contributions.

Simulations of the Shift-Rotation technique were carried out in MATLAB to demonstrate the calibration process as well as to provide a software platform for the error separation of form measurements. In these simulations, freeform surfaces were generated on grids with aperture diameters of 1001 pixels by using combinations of Zernike polynomials. Decomposition of freeform surfaces into Zernike polynomials was

TABLE 2.1 Zernike terms, up to the 4th order.

n	m	Zernike function	Common name
0	0	1	Piston
1	1	$\rho \cos \theta$	Tilt x
1	-1	$\rho \sin \theta$	Tilt y
2	0	$2\rho^2 - 1$	Defocus
2	2	$\rho^2 \cos 2\theta$	Astigmatism x
2	-2	$\rho^2 \sin 2\theta$	Astigmatism y
3	1	$(3\rho^3 - 2\rho) \cos \theta$	Primary x coma
3	-1	$(3\rho^3 - 2\rho) \sin \theta$	Primary y coma
3	3	$\rho^3 \cos 3\theta$	Trefoil x
3	-3	$\rho^3 \sin 3\theta$	Trefoil y
4	0	$6\rho^4 - 6\rho^2 + 1$	Primary spherical
4	2	$(4\rho^4 - 3\rho^2) \cos 2\theta$	Secondary astigmatism x
4	-2	$(4\rho^4 - 3\rho^2) \sin 2\theta$	Secondary astigmatism y
4	4	$\rho^4 \cos 4\theta$	Tetrafoil x
4	-4	$\rho^4 \sin 4\theta$	Tetrafoil y

appropriate because the Zernike coefficients are easily determined and represent combinations of primary (Seidel) and higher-order aberrations observed on optical surfaces [69]. In this Chapter, four Zernike terms were used while up to fifteen Zernike terms are used in Chapter 5. The lowest order Zernikes were chosen in these Shift-Rotation simulations but the method can be applied to higher orders. The fitting in Chapter 5 is limited to 4th order given the relatively sparse measurement data. The Zernike ordering scheme used in this work is based on Noll's concept [70], and Table 2.1 lists the fifteen Zernike terms [18, 71, 72] used in Chapter 5.

The simulated surfaces were considered as comprising rotationally varying (RV) and rotationally invariant (RI) components of the test part and machine errors. These components were represented as P_{RV} , P_{RI} , M_{RV} , and M_{RI} respectively. The Shift-Rotation calibration technique was then used to decompose the simulated surface measurements into four output height maps: Output P_{RV} , Output P_{RI} , Output M_{RV} , and Output M_{RI} . From these separated components, a combination of the separated part components, Output P_{RV} and Output P_{RI} , was used to represent a measurement of the part without the machine's error contributions.

The first step in the simulations involved generating a freeform height map from known inputs (part and machine error components). If, for example, "MP" depicts this height map, it can be expressed as shown in Equation 2.1.

$$MP = P_{RV} + P_{RI} + M_{RV} + M_{RI} \quad (2.1)$$

Zernike primary x coma was used to represent P_{RV} (the RV component of the test surface), Zernike primary spherical aberration (SA3) represented P_{RI} (the RI component of the test surface), Zernike primary astigmatism x represented M_{RV} (the RV component of the machine errors), and Zernike defocus represented M_{RI} (the RI component of the machine errors). The maps of these input components are shown in Figure 2.1.

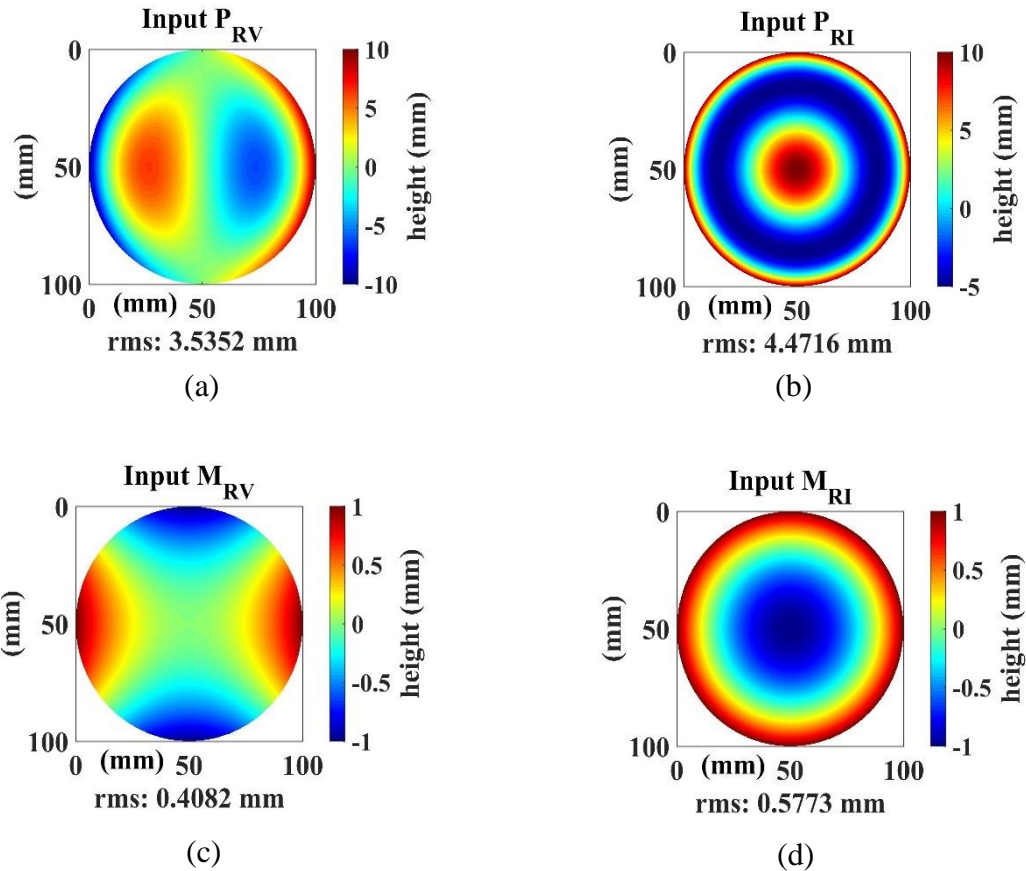


FIGURE 2.1 Zernike aberration representations of the simulated test surface components and machine errors. (a) Primary coma represents P_{RV} . (b) Primary spherical represents P_{RI} . (c) Primary astigmatism represents M_{RV} . (d) Defocus represents M_{RI} .

These input components were then superposed to generate the freeform height map shown in Figure 2.2. Since the freeform part was generated with known inputs, after the Shift-Rotation technique was used to decompose the freeform into four output components,

the separated output components were compared to the known inputs to demonstrate the separation technique.

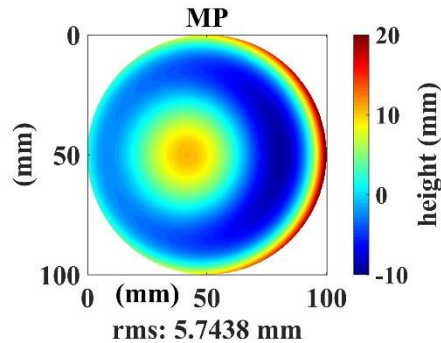


FIGURE 2.2 A simulated measurement of a freeform surface containing the part, as well as error contributions from the machine.

Figure 2.2 represents a measurement of a freeform part with a 100.1-mm-diameter circular aperture (10 pixels were used to represent a 1-mm length). This simulated measurement result depicts the freeform surface and also includes errors from the measuring machine. This simulated surface was deliberately generated with large form deviations and the amplitudes of the simulated machine errors were also deliberately large.

To separate the components in the above height map, the “Rotation” portion of the Shift-Rotation technique was used to solve for the RV components of the part and machine, while the “Shift” portion solved for the RI components. The following sections show how simulated measurement results, obtained after multiple part rotations and translations, can be used to obtain the RV and RI components of the part and machine.

2.1 Separation of the Rotationally Varying Components

The N-rotation is used to solve for the RV components of the part. This N-rotation technique has been in use in interferometry (the first publication containing proof was in 1996) and has the advantage of being noise tolerant and computationally simple [65]. Here, measurements of the part are made after the part is rotated (about the optical axis) to N

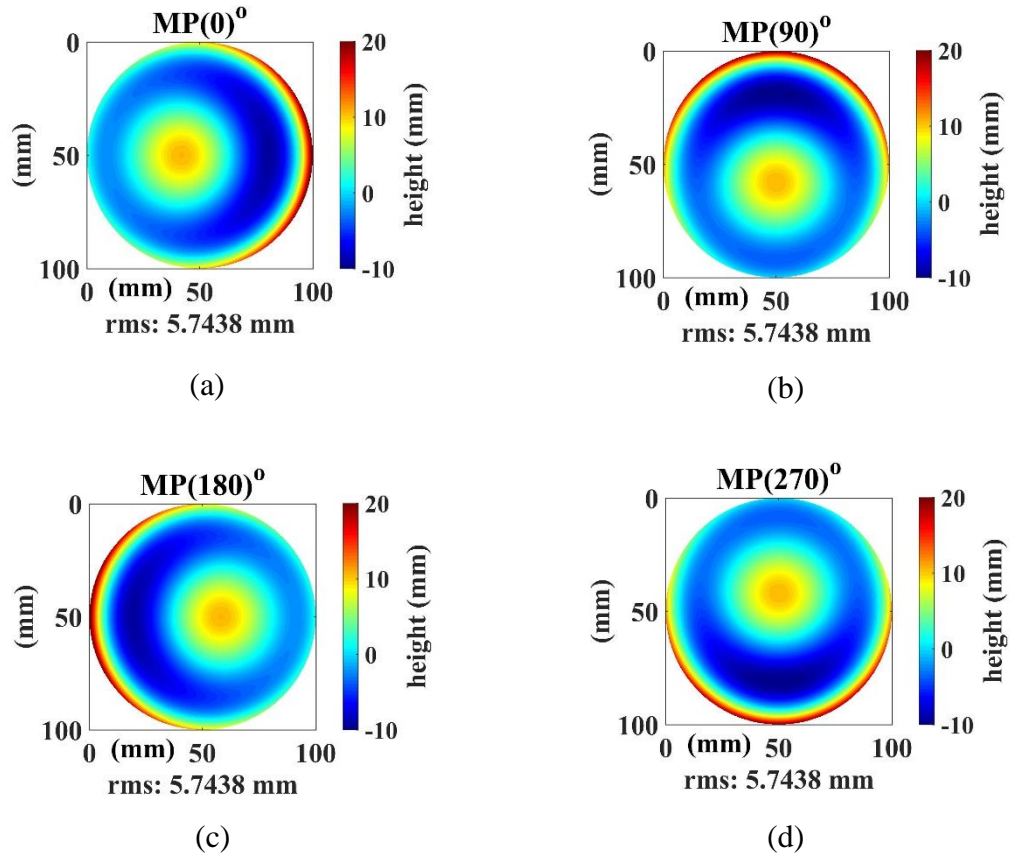


FIGURE 2.3 Simulated measurements after rotations of the freeform part.
 (a) Measurement at an initial position and orientation of the freeform part.
 (b) Measurement after rotating the part 90 degrees from the initial orientation.
 (c) Measurement after rotating the part 180 degrees from the initial orientation.
 (d) Measurement after rotating the part 270 degrees from the initial orientation.

positions, separated by $360^\circ/N$. The average of these measurements would then contain none of the RV components of the part, except those with angular orders that are harmonics of $360^\circ/N$ [65]. The number of rotations required would be higher than the highest angular order expected to be of significant amplitude on the part. Since these simulated height maps were generated with a highest Zernike angular order of 2θ , three rotations were sufficient to solve for the RV components. However, in these simulations, the part was rotated to 4 positions separated by 90° and this shows numerically that sub-harmonics are properly separated. Simulated measurements at the four rotated positions of the part are shown in

Figure 2.3. The average of the four height maps in Figure 2.3, would then be a height map without the RV components of the part. If this average is denoted by $Mean_{P(rot)}$, it can be expressed as shown in Equation 2.2, and Figure 2.4.

$$Mean_{P(rot)} = P_{RI} + M_{RV} + M_{RI} \quad (2.2)$$

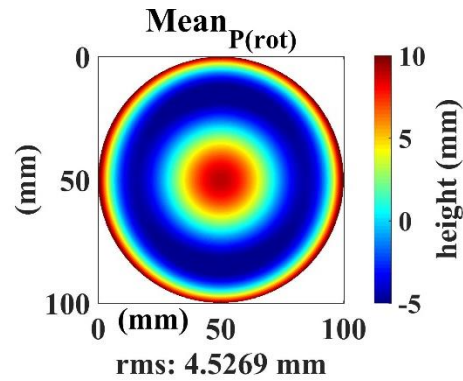


FIGURE 2.4 An average of the four rotated part measurements.

The RV component of the part, dropped out by the averaging process, can be obtained by the subtracting in Equation 2.2 from Equation 2.1 (or subtracting the map in Figure 2.4 from that in Figure 2.2); and the resulting map is shown in Figure 2.5.

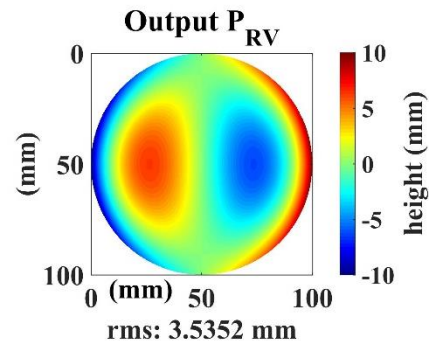


FIGURE 2.5 The separated rotationally varying component of the freeform part.

The map in Figure 2.5, ‘Output P_{RV} ’, represents the first of the four desired separated components (as listed in Equation 2.1) and is stored for later use. The next surface

component to be solved is the RV component of the machine's errors. No additional measurement is required to solve for this, as it can be deduced from Equation 2.2.

If the RV components of the part were completely separated and expressed in the Output P_{RV} map, any residual RV component in Equation 2.2 (and Figure 2.4) must be from the machine's error contribution. This machine RV component can be obtained by applying the same rotation and averaging process, used to solve for the RV component of the part, on the height map in Figure 2.4. The maps obtained after rotating 'Mean $P_{(rot)}$ ' to four positions, separated by 90° , are shown in Figure 2.6. Alternatively, the RV component of the machine can be obtained by rotating the raw rotated measurements (in Figure 2.3) to the same orientation, and averaging.

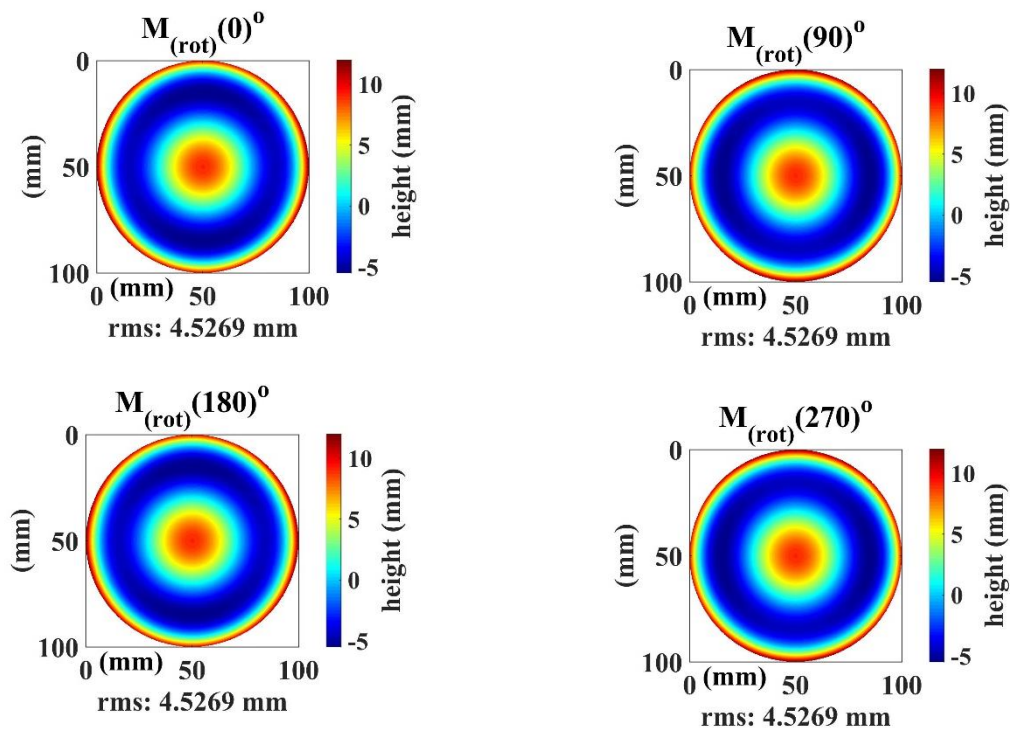


FIGURE 2.6 Simulated measurements depicting rotations of the machine's RV errors.

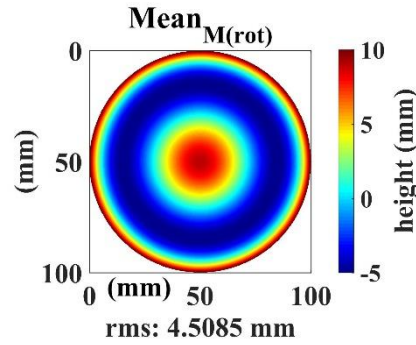


FIGURE 2.7 Average of the height maps that depict machine rotations. This average drops out the rotationally varying components of the machine errors.

The RV components of the machine errors rotate with the rotations in Figure 2.6. These rotated RV components are not noticeable in the above figure because their amplitudes are small, compared to the amplitudes of the RI part. Nonetheless, an average of the four height maps drops out these RV error components and the resulting average can be expressed as shown in Equation 2.3 and Figure 2.7.

$$Mean_{M(rot)} = M_{RI} + P_{RI} \quad (2.3)$$

The RV machine error component dropped out by the averaging process, can be obtained by the subtracting Equation 2.3 from Equation 2.2; the resulting map from this subtraction is shown in Figure 2.8.

$$M_{RV} = Mean_{P(rot)} - Mean_{M(rot)} \quad (2.4)$$

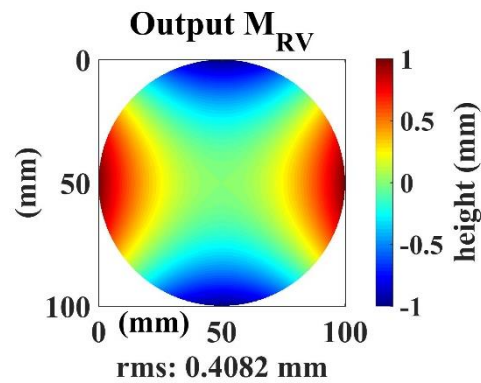


FIGURE 2.8 The separated rotationally varying component of the machine's errors.

This height map, 'Output M_{RV} ', represents the second of the four desired separated components and should be stored for later use. Since the RV components of the part and machine errors have been separated, the resulting 'Mean $M_{(rot)}$ ' height map in Figure 2.7 should contain only RI components of the freeform part and the machine's errors. These RI components can be obtained from the 'Shift' portion of the Shift-Rotation technique, as shown in the next section.

2.2 Separation of the Rotationally Invariant Components

The 'Shift' section of the Shift-Rotation technique is used to separate the RI components of the part and machine errors. At least, two measurements are required. Measurements of the part are required before and after the part has been laterally shifted by a known translation distance, Δ , with respect to the machine. If an additional translated measurement is required, it could be made after a further translation of the part. Certain situations give rise to the need for this additional translated part measurement, and these situations will be mentioned after solving for the RI components from only two measurements. The benefits of this additional measurement will also be demonstrated.

To begin, we will illustrate the scenario requiring only two measurements; here, the translation distance should be small, compared to the aperture size, limited by signal to noise considerations. For example, Figure 2.9 (*left*) shows a simulated measurement of the part in an initial position, and after the part was translated 2 mm to the left, its simulated measurement was as depicted in Figure 2.9 (*right*).

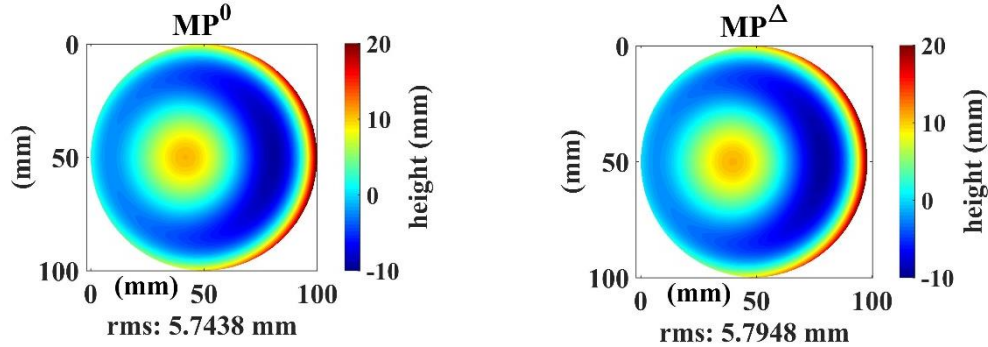


FIGURE 2.9 Simulated measurement of the part in an initial position (*left*). Simulated measurement after the part was shifted 2 mm to the left (*right*).

If the measurement of the part in the initial position is expressed as shown in Equation 2.5, where the superscripts, ‘0’, indicate an initial position, then, the measurement after a lateral shift of the part can be expressed as shown in Equation 2.6. The superscripts, Δ , indicate the translated components.

$$MP^0 = P^0_{RV} + P^0_{RI} + M^0_{RV} + M^0_{RI} \quad (1.5)$$

$$MP^\Delta = P^\Delta_{RV} + P^\Delta_{RI} + M^0_{RV} + M^0_{RI} \quad (2.6)$$

Equation 2.6 indicates that the measurement of the translated part, MP^Δ , should be made in the same region of the machine’s measuring volume as the initial measurement, MP^0 . In other words, MP^Δ should feature a translated part under test without a ‘translation’ of the machine’s error contributions. Since the RV components of the part and machine have already been obtained, these can be subtracted (in their respective orientations) from

MP^0 and MP^Δ . Then, a difference between the resulting maps would drop out the RI machine errors and leave behind the slope of the part (Equation 2.7) evaluated at the separation and in the direction Δ . The height map representation of this slope is shown in Figure 2.10.

$$MP^\Delta - MP^0 - (P_{RV}^\Delta - P_{RV}^0) = P_{RI}^\Delta - P_{RI}^0 \quad (2.7)$$

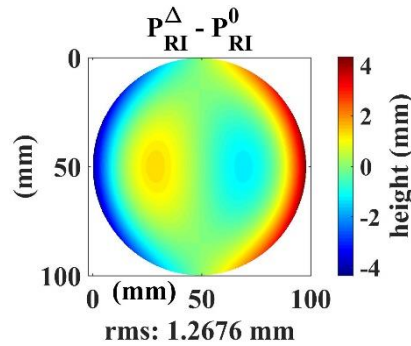


FIGURE 2.10 The slope of the freeform part, evaluated after a 2-mm lateral translation.

The goal of the following steps is to obtain the RI component of the part from the slope map in Figure 2.10. If a profile, \mathbf{g} , is extracted from the part center to the edge in the $-\Delta$ direction, each point in \mathbf{g} would be a height difference between two points (a distance Δ apart) in the desired radial profile, \mathbf{f} . The relationship between profiles \mathbf{f} and \mathbf{g} can be expressed as a system of linear equations: $\mathbf{g} = \mathbf{H} * \mathbf{f}$, where \mathbf{g} is an $m \times 1$ column vector, \mathbf{f} is an $n \times 1$ column vector, and \mathbf{H} is an $m \times n$ design matrix to be built [66].

This design matrix can be explained with an example, where column elements g_1 to g_5 represent an extracted profile from a slope map after a 1-pixel lateral translation. This column vector can be expressed as shown in Equations 2.8a – 2.8e.

$$g_1 = f_1 - f_2 \quad (2.8a)$$

$$g_2 = f_2 - f_1 \quad (2.8b)$$

$$g_3 = f_3 - f_2 \quad (2.8c)$$

$$g_4 = f_4 - f_3 \quad (2.8d)$$

$$g_5 = f_5 - f_4 \quad (2.8e)$$

This can be further expressed in matrix form as shown in Table 2.2.

TABLE 2.2 Linear system relationship between the slope profile (\mathbf{g}) and the desired radial profile (\mathbf{f}).

$$\begin{bmatrix} \mathbf{g} \\ g_1 \\ g_2 \\ g_3 \\ g_4 \\ g_5 \end{bmatrix} = \begin{bmatrix} 1 & -1 & 0 & 0 & 0 \\ -1 & 1 & 0 & 0 & 0 \\ 0 & -1 & 1 & 0 & 0 \\ 0 & 0 & -1 & 1 & 0 \\ 0 & 0 & 0 & -1 & 1 \end{bmatrix} \mathbf{H} * \begin{bmatrix} \mathbf{f} \\ f_1 \\ f_2 \\ f_3 \\ f_4 \\ f_5 \end{bmatrix}$$

Elements g_1 to g_5 represent profile points extracted from the slope obtained from measurement data, and \mathbf{f} is the radial profile to be solved for. If the design matrix, \mathbf{H} , is a square matrix with dimension $m = n$, the profile, \mathbf{f} , can be solved from Equations 2.9.

$$\mathbf{g} = \mathbf{H}\mathbf{f} \quad (2.9a)$$

$$\mathbf{H}^{-1}\mathbf{g} = \mathbf{H}^{-1}\mathbf{H}\mathbf{f} \quad (2.9b)$$

$$\mathbf{f} = \mathbf{H}^{-1}\mathbf{g} \quad (2.9c)$$

If the design matrix, \mathbf{H} , is non-square, with $m \neq n$, the solution of the profile, \mathbf{f} , can then be obtained via Equations 2.10.

$$\mathbf{g} = \mathbf{H}\mathbf{f} \quad (2.10a)$$

$$\mathbf{H}^T\mathbf{g} = \mathbf{H}^T\mathbf{H}\mathbf{f} \quad (2.10b)$$

$$(\mathbf{H}^T\mathbf{H})^{-1}\mathbf{H}^T\mathbf{g} = (\mathbf{H}^T\mathbf{H})^{-1}\mathbf{H}^T\mathbf{H}\mathbf{f} \quad (2.10c)$$

$$\mathbf{f} = (\mathbf{H}^T \mathbf{H})^{-1} \mathbf{H}^T \mathbf{g} \quad (2.10d)$$

\mathbf{H}^{-1} and \mathbf{H}^T represent the inverse and transpose of \mathbf{H} , respectively, while $\mathbf{H}^T \mathbf{H}$ is an $n \times n$ square matrix. Regardless of which of the above (Equations 2.9 or 2.10) applies, neither can directly be used to solve for the radial profile, \mathbf{f} , if the design matrix (\mathbf{H}) is singular (non-invertible). At this juncture, a possible way forward involves searching for a suitable approximate solution of the linear equation, $\mathbf{g} = \mathbf{H}^* \mathbf{f}$, by way of a pseudo-inverse of the singular matrix \mathbf{H} (or $\mathbf{H}^T \mathbf{H}$). Another approach involves searching for ways to make the \mathbf{H} (or $\mathbf{H}^T \mathbf{H}$) matrix become non-singular. Both approaches are discussed in the next section.

2.2.1 A Way around the Singularity of the Design Matrix

The design matrix, \mathbf{H} , is singular (non-invertible) because its determinant, $|\mathbf{H}|$, is zero; a matrix whose determinant is zero is said to be singular [73, 74]. A singular matrix has no inverse because if an inverse exists when \mathbf{H} is singular, then, $|\mathbf{H}^{-1}| \times |\mathbf{H}| = |\mathbf{H}^{-1}| \times 0 = 0$, and $|\mathbf{H}^{-1}| \times |\mathbf{H}| = |\mathbf{H}^{-1} \mathbf{H}| = |\mathbf{I}| = 1$, and this results in a contradiction [73]. Furthermore, the adjoint method for calculating the inverse of a square matrix is shown in Equation 2.11, where it shows how zero-determinant results in a singularity [73-77].

$$\mathbf{H}^{-1} = \frac{\text{adj } \mathbf{H}}{|\mathbf{H}|} \quad (2.11)$$

This singularity can also be explained by the presence of linear dependencies or relationships between the rows or columns of the \mathbf{H} matrix. In other words, if any column (or row) in a matrix is repeated, or if any column (or row) is a multiple of another column (or row), the matrix becomes singular [74-76]. This \mathbf{H} matrix singularity makes it

challenging to obtain a direct solution of column vector \mathbf{f} , from Equation 2.9c (or Equation 2.10d).

One approach that could be used to solve Equation 2.9c, involves calculating a generalized inverse or pseudo-inverse of \mathbf{H} (or $\mathbf{H}^T\mathbf{H}$), and this leads to a pseudo-solution of the column vector \mathbf{f} [75, 78]. One method of obtaining a pseudo-inverse is the Moore-Penrose generalized inverse [75, 77, 79, 80]; this decomposes the \mathbf{H} matrix into a product of matrices, whose dimensions are related to the rank, r , of the \mathbf{H} matrix. This rank, r , of the \mathbf{H} matrix is the size of the largest square sub-matrix of \mathbf{H} which is non-singular. If \mathbf{H} is $m \times m$ and non-singular, it is said to be full-rank with a rank equal to m [73, 77]. With the Moore-Penrose pseudo-inverse decomposition, if \mathbf{H} is $m \times n$ with a rank $r > 0$, then there exists $m \times r$ and $n \times r$ matrices \mathbf{P} and \mathbf{Q} respectively, such that

$$\mathbf{P}^T\mathbf{P} = \mathbf{Q}^T\mathbf{Q} = \mathbf{I}_r \quad (2.12a)$$

$$\mathbf{H} = \mathbf{P}\mathbf{\Delta}\mathbf{Q}^T \quad (2.12b)$$

where $\mathbf{\Delta}$ is an $r \times r$ diagonal matrix with positive diagonal elements [75, 81, 82]. The right-hand side of Equation 2.12b is a singular value decomposition of \mathbf{H} , from which the Moore-Penrose pseudo-inverse can be obtained and expressed as:

$$\mathbf{H}^+ = \mathbf{Q}\mathbf{\Delta}^{-1}\mathbf{P}^T \quad (2.13)$$

This Moore-Penrose pseudo-inverse could then be used to obtain a pseudo-solution of the column vector \mathbf{f} . The Moore-Penrose inverse explained above, is one of several generalized inverses which could be used to obtain the pseudo-inverse of a singular matrix. Other factorization methods could be used to produce pseudo-inverses, but these are not suited for singular matrices. They decompose the singular matrix into a product of lower-dimensional matrices, and some examples of these include QR factorization, Cholesky

factorization, and LU factorization. The QR factorization decomposes a matrix into the form: $\mathbf{H} = \mathbf{QR}$, where \mathbf{Q} is a unitary matrix and \mathbf{R} is an upper triangular matrix [77, 83]. The Cholesky factorization decomposes a symmetric matrix into the form: $\mathbf{H} = \mathbf{BB}^T$, where \mathbf{B} is a real lower triangular matrix [83], while the LU factorization decomposes a matrix into the form: $\mathbf{H} = \mathbf{LU}$, where \mathbf{L} is a lower triangular matrix and \mathbf{U} is an upper triangular matrix [83, 84]. From any of these factorizations, a pseudo-inverse might be obtained, but since they are not designed for singular matrices, results can vary widely between methods.

Alternatively, a different approach can be used to solve Equation 2.9c. This alternative approach does not seek a pseudo-inverse solution, instead, it focuses on converting the singular \mathbf{H} matrix into a non-singular (invertible) matrix. In the first place, if the \mathbf{H} matrix was invertible, the unique solution of vector \mathbf{f} would be obtainable. Via this alternative approach, if the \mathbf{H} matrix is made invertible, and is well-behaved, there would also be one unique solution of vector \mathbf{f} . However, this unique solution would most likely approximate the exact solution and the approximation depends on how the \mathbf{H} matrix is made invertible.

This approach to solving the singularity, deals with perturbing the linear dependencies between the rows and columns of the matrix, and offsetting the symmetry within the singular matrix in such a way that the singular matrix becomes a well-behaved non-singular matrix. Elementary operations like permuting the rows or columns, adding a multiple of one row or column to another, or multiplying the elements of a row or column by a non-zero constant, change neither the determinant nor rank of the singular matrix, and hence, do not make the matrix invertible [73, 75, 77]. The required perturbation can be achieved by adding a small amount of non-symmetric noise to the singular matrix to offset

its symmetry. This converts the singular \mathbf{H} matrix into a matrix whose set of vectors have no zero-valued linear combination relationship (except the trivial one with all the coefficients equal to zero). This conversion makes the columns and rows linearly independent, and hence, non-singular [73].

Instead of the linear system in Equation 2.9a, the modified-matrix is represented as shown in Equation 2.14, where matrix \mathbf{E} represents the noise added to the singular matrix, \mathbf{H} .

$$\mathbf{g} = (\mathbf{H} + \mathbf{E})\mathbf{f} \quad (2.14)$$

The modified-matrix $(\mathbf{H} + \mathbf{E})$ would have a full rank and a unique real-inverse but has a limitation that depends on the elements in \mathbf{E} , their design, and their relationship with the elements in \mathbf{H} . For example, when a noise of 1×10^{-12} was added to the 1's in the \mathbf{H} matrix, it was sufficient to make the matrix invertible. The output solution of the vector \mathbf{f} , obtained after this perturbation, was approximately equal to the ideal vector \mathbf{f} input to the simulation. The following example compares the solution from the inverse of a noise-modified singular matrix to that from a pseudo-inverse of the singular matrix.

Simulations were used to compare a modified-matrix solution to a pseudo-inverse solution. An ideal radial profile \mathbf{f} was extracted from the known rotationally invariant surface in Figure 2.1(b). From the slope height map in Figure 2.10 (obtained after a part translation distance of $\Delta = 2$ mm), a \mathbf{g} profile was extracted (from the part center to the edge in the $-\Delta$ direction). After generating the required design matrix \mathbf{H} which was singular, the Moore-Penrose pseudo-inverse method was used to obtain a pseudo-inverse \mathbf{H}^+ from which the pseudo-solution of column vector \mathbf{f} was obtained. Also, a modified \mathbf{H}

matrix (noise of 1×10^{-12} added to the diagonal of \mathbf{H}) was used to obtain a solution of column vector \mathbf{f} . Both solutions are compared to the ideal radial profile in Figure 2.11.

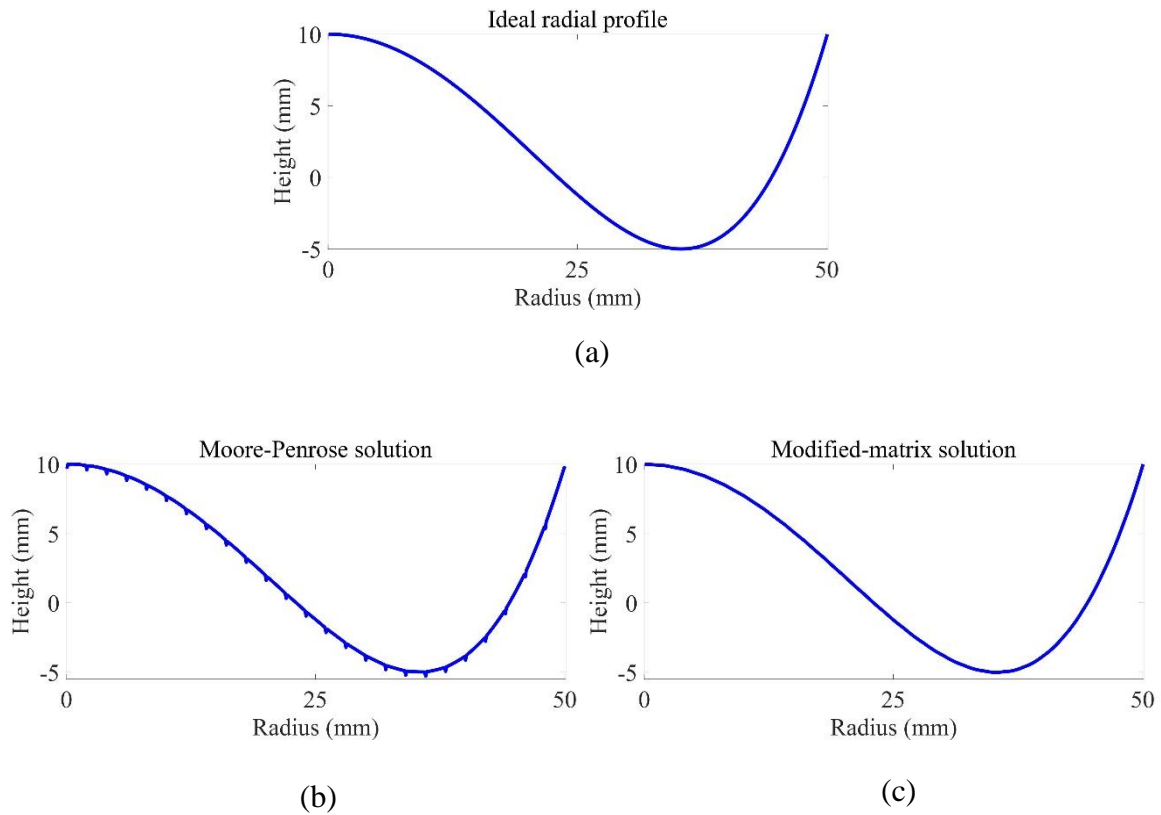


FIGURE 2.11 Comparison between a pseudo-inverse RI solution and the solution from a noise-modified design matrix. (a) The input radial profile used as a bench-mark for the comparison. (b) Output profile from a pseudo-inverse solution. (c) Output profile from a noise-modified design matrix solution.

Figure 2.11 shows the input radial profile, a profile obtained from a Moore-Penrose pseudo-inverse, and a profile from a noise-modified \mathbf{H} matrix. Subtracting the ideal radial profile from both solutions yielded the residuals shown in Figure 2.12. These show the modified matrix solution having lower peak-valley deviations than the pseudo-inverse.

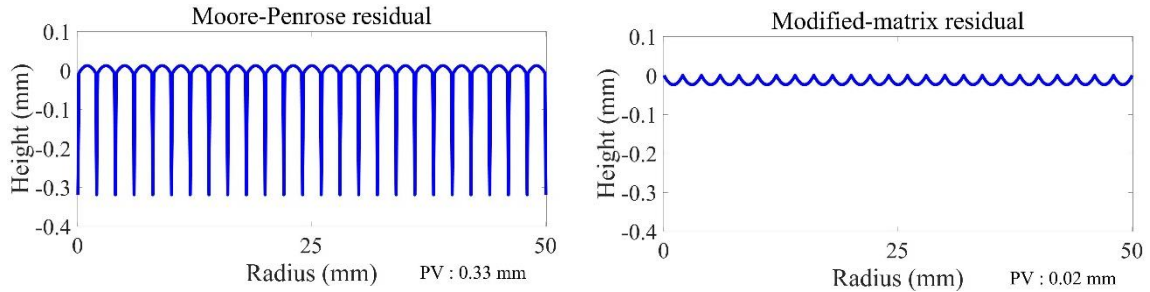


FIGURE 2.12 Difference between a Moore-Penrose output and the ideal profile (*left*). Difference between a noise-modified design matrix output and the ideal profile (*right*).

It should also be noted that the amplitudes of the residuals shown in Figure 2.12 change proportionally with respect to the translation distance. At a small translation distance of 100 μm , both approaches agreed with the ideal solution; their residual rms differences were 1.65 nm. The residuals from both approaches increase with increase in translation distance; but the residual errors from the pseudo-inverse were consistently larger than those from the noise-modified inverse. For example, at a large translation distance of 5.5 mm, the residual rms difference from the pseudo-inverse was 0.31 mm while that from the noise-modified inverse was 0.06 mm.

Since these comparisons demonstrate that the modified design matrix leads to output RI components which are closer to the input RI components than those from a pseudo-inverse, the modified design matrix was used to obtain the outputs of the RI part and machine error components, in this chapter. Now that an approach to solving the singularity of the design matrix has been selected, the next section returns to the separation of the RI components of the machine and part.

2.3 Separation of the Rotationally Invariant Components continued

From the slope map in Figure 2.10, a profile, \mathbf{g} , was extracted from the translated part center to the edge in the $-\Delta$ direction. Each point in \mathbf{g} represents a height difference between two points (a distance Δ apart) in the desired radial profile, \mathbf{f} , and can be expressed as $\mathbf{g} = \mathbf{H}\mathbf{f}$. The modified design matrix, \mathbf{H} , was then used to solve for the radial profile \mathbf{f} , and this profile was graphed as shown in Figure 2.13.

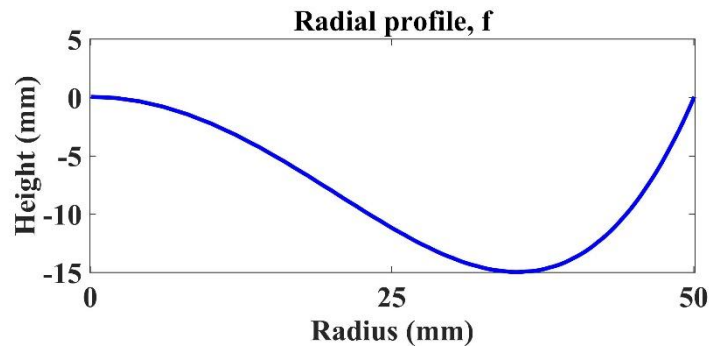


FIGURE 2.13 Radial profile of the rotationally invariant freeform surface.

The RI component of the test surface can then be obtained by generating a surface from the solved radial profile in Figure 2.13. The pixel-data on the left end of this profile becomes the center of the desired RI component of the part. This generated RI component of the part is shown in Figure 2.14 and represents the third of the four desired output components.

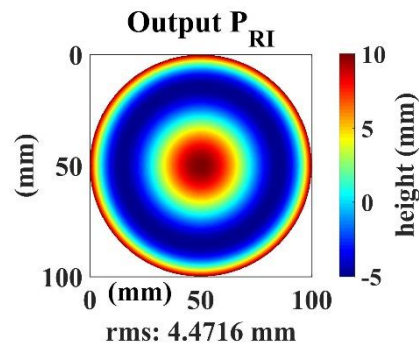


FIGURE 2.14 The rotationally invariant component of the freeform part.

The fourth separated component, the RI component of the machine's error, can then be obtained by subtracting the three previously solved components from any measurement of the part, for example, that shown in Figure 2.2. This fourth output component is shown in Figure 2.15.

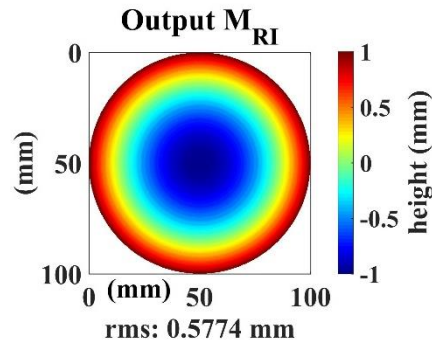


FIGURE 2.15 The rotationally invariant component of the machine errors.

2.4 Part Measurement without Machine Error Contributions

At this point, the simulated freeform surface in Figure 2.2 has been separated into four components: Output P_{RV} , Output M_{RV} , Output P_{RI} , and Output M_{RI} , as summarized in Figure 2.16. The sum of the decomposed components of the test part, Output P_{RV} + Output P_{RI} , should represent a measurement of the freeform surface without the error contributions from the machine.

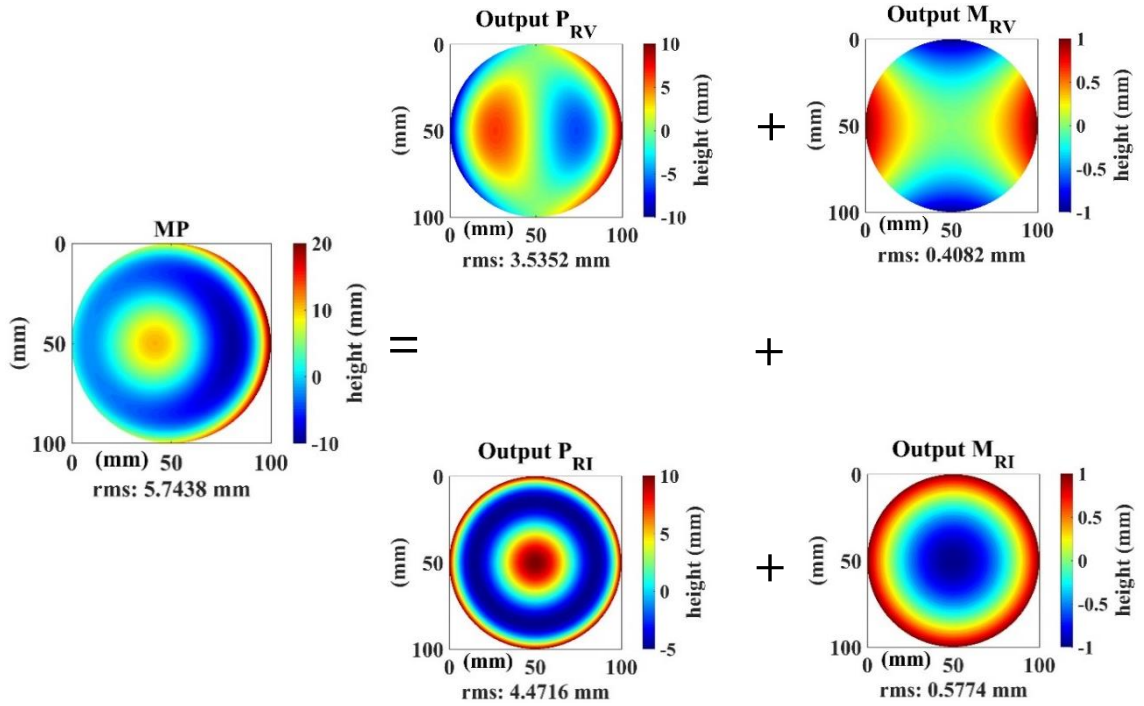


FIGURE 2.16 Separation of the simulated freeform surface into its four constituent components.

This sum is shown in Figure 2.17 and represents a part measurement with a minimized uncertainty because the RV and RI machine error contributions have been removed. The task-specific machine error contributions can then be obtained by the sum

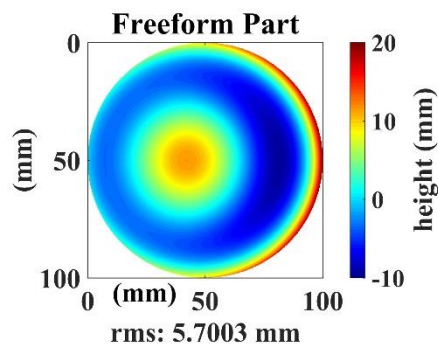


FIGURE 2.17 A simulated measurement of the freeform surface, without the RV and RI machine errors.

of the separated RV and RI machine errors, or by subtracting the solution in Figure 2.17 from the input part in Figure 2.2. This machine error contribution is shown in Figure 2.18.

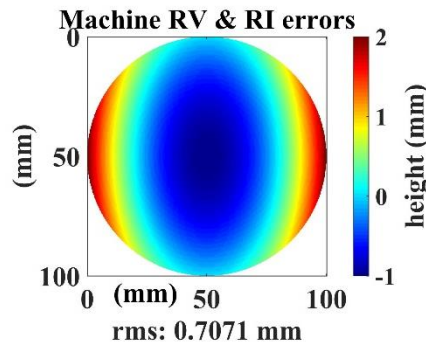


FIGURE 2.18 The simulated task-specific machine error contributions.

2.5 A More Robust Rotationally Invariant Solution

In solving for the above RI components, only one lateral translation was used. If only one translation is to be used, the translation distance should be small, compared to the aperture size, limited by signal to noise considerations. In the above example, a translation distance of 2 mm was used (the part had an aperture-diameter of 100.1 mm). If a large translation distance is used, or if the solved radial profile (Figure 2.13) is not a continuous curve, two or three lateral translations of the part might be necessary to solve for the RI components. In this case, the linear system described in Table 2.2 would become a combination obtained from the multiple lateral translations.

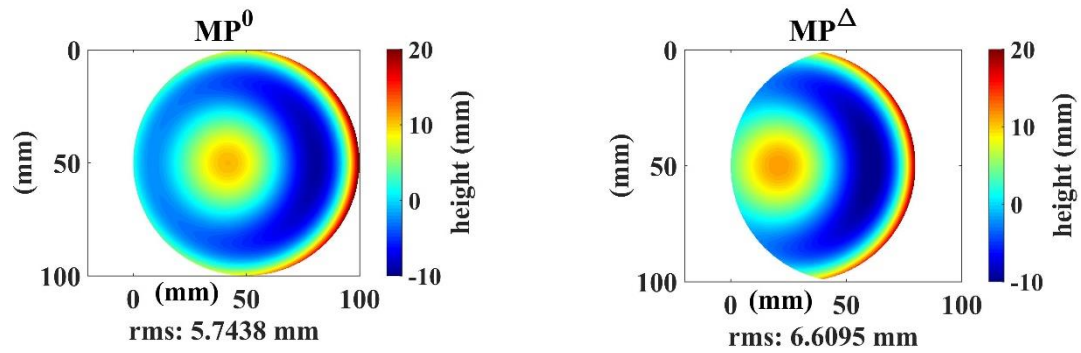


FIGURE 2.19 Simulated measurement of the part in an initial position (*left*). Simulated measurement after the part was shifted 20 mm to the left (*right*).

For example, if a 20-mm translation was used instead of the 2-mm translation distance previously used, the before and after-simulated shear measurements would be as represented in Figure 2.19.

After subtracting the RV component of the part (which was previously separated) from the height maps in Figure 2.19, the resulting slope of the part evaluated at this 20-mm separation and in the direction Δ , would be obtained as shown in Figure 2.20.

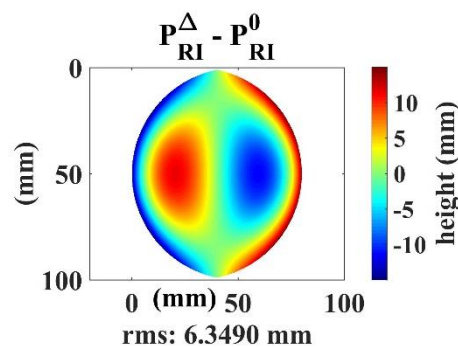


FIGURE 2.20 Slope of the part, evaluated after a 20-mm lateral translation.

From this illustration with a translation distance of 20 mm, the radial profile, \mathbf{f} , solved from a profile, \mathbf{g} (extracted from the slope of the part), is shown in Figure 2.21 (*left*). This solved profile appears segmented, with segments having a period of the translation distance. The height map generated from this profile is shown in Figure 2.21 (*right*).

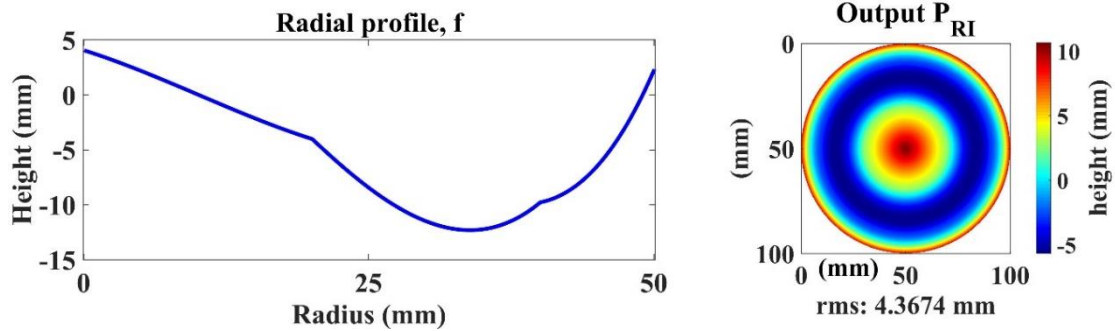


FIGURE 2.21 Radial profile of the part, obtained after a large translation distance of 20 mm (*left*). The RI component of the part, generated from this profile (*right*).

This segmentation that appears in the radial profile, obtained after employing a large translation of the part, modifies the radial profile from its ideal form. A radial profile, closer to the ideal, can be obtained by incorporating measurements after additional translations of the part. When simulated part measurements were made after part translations of 20 mm, 23 mm, and 25 mm, their combined extracted \mathbf{g} profiles, along with their combined design matrices, were used to solve for the radial profile of the part. This radial profile, with its generated height map, is shown in Figure 2.22. This shows an improvement in the solved RI component of the part can be obtained from multiple translations of the part (different translation distances), instead of just one large translation.

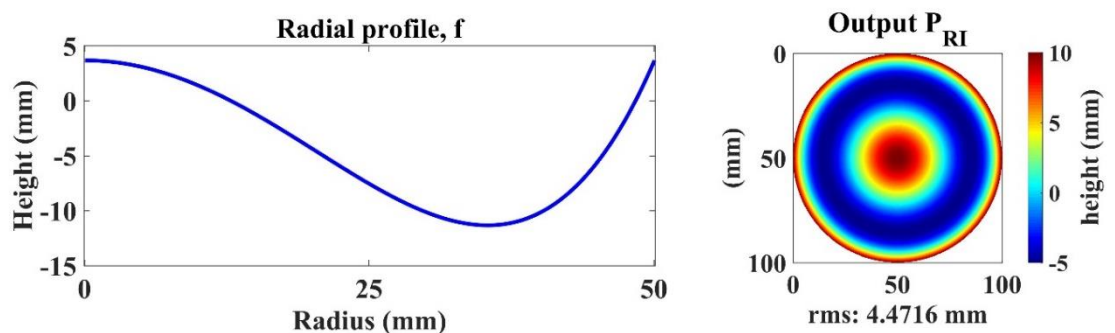


FIGURE 2.22 Improved radial profile of the part, obtained from simulated part measurements after 20 mm, 23 mm and 25 mm translations (*left*). The RI component of the part, generated from this profile (*right*).

The rms of the Output P_{RI} height map obtained here, matches that obtained when a small translation distance of 2 mm was used.

A comparison was made between the Output P_{RI} solution obtained after the initial 2-mm translation distance, and that obtained from the combination of multiple translation distances of 20-mm, 23-mm, and 25-mm. Both RI solutions were subtracted from the part RI input to the system and are shown in Figure 2.23. Figure 2.23 (*left*) shows the residual after a 2-mm part-translation while Figure 2.23 (*middle*) shows the residual after the multiple part-translations of 20-mm, 23-mm, and 25-mm. The difference between the RI solutions from the single and multiple translations is shown in Figure 2.23 (*right*).

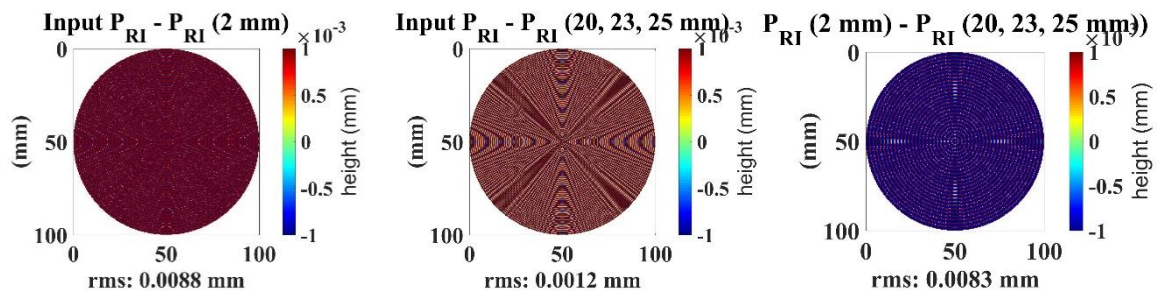


FIGURE 2.23 Input minus output RI part components, after a 2-mm translation of the part (*left*). Input minus output RI part components, after multiple part-translations of 20-mm, 23-mm, and 25-mm (*middle*). A difference between the output P_{RI} solutions from single and multiple part-translations (*left*).

The comparison shows that besides a reduction in the translation distance, a combination from shear-measurements of the part at multiple translation distances can yield an improvement in the solution of its RI components.

2.6 Influence of Random Machine Z-axis Errors on the Error Separation Process

So far in Chapter 2, the simulated machine errors have all been systematic. These systematic errors are functions of position in the x- and y- axes, and were assumed to have unique amplitudes with respect to position within the measuring volume. This chapter investigates a possible scenario that could arise when the previous assumption does not hold. Here, the machine's systematic errors were simulated not just as functions of position in the x- and y- axes, but also to have random components in the z-direction. In these simulations, the +z-axis points out of the page. The influence of these random z-axis errors on the error separation process were investigated by comparing separated RV and RI output components to the respective input components.

The influence of machine errors that change systematically in the z-direction were not simulated. If these are present in a measuring machine, the machine errors would be different between rotated freeform part measurements. Nonetheless, the Shift-Rotation would separate these errors as rotationally varying machine error components.

The random z-axis machine errors were simulated to be components of the systematic errors and the effects of four sets of these random errors were investigated. The four sets contained uniformly-distributed random z-axis errors (that change on every rotation) with maximum amplitudes of 10%, 1%, 0.1%, and 0.01% deviations from the nominal systematic errors, on a pixel-by-pixel basis. Results from the 10% deviations are shown below while results from the 1%, 0.1%, and 0.01% deviations are in Appendix B; their summary is in Chapter 2.6.2.

2.6.1 Influence of 10% Random Machine Z-axis Errors

Figure 2.24 (*left*) shows a simulated systematic machine error, without random errors in the z-axis. After the addition of a random z-axis error with a maximum amplitude

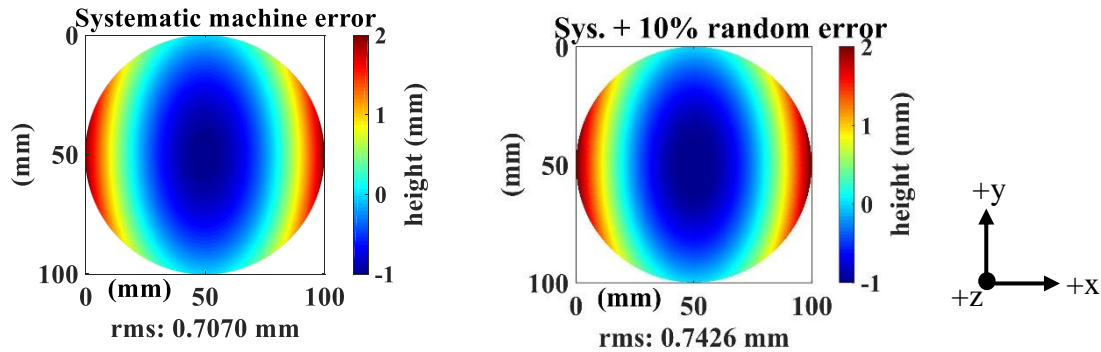


FIGURE 2.24 Simulated systematic machine errors (*left*). The machine's systematic errors with a random component in the z-direction; the random errors have a maximum amplitude of 10% the nominal systematic error. (*right*).

of 10% deviation from the nominal, the resulting machine error is plotted in Figure 2.24 (*right*). An effect of the added random error can be noticed by the change in the rms of the height maps.

To evaluate the effects of the added random errors on the error separation process, the Shift-Rotation error separations were carried out on the simulated surface with the systematic and random errors shown in Figure 2.24 (*right*). After Shift-Rotation error separations (4 rotations in the N-Rotation technique, and a 200 μm part translation in the Shift-technique) of the part that included the random machine errors, the separated output components were compared to the input components, as shown in Figure 2.25. The comparison between the output and input RV components shows that even with the added 10% random machine errors, the N-Rotation technique correctly separated the RV components of the part and machine. The rms of the Output P_{RV} height map equals that of

the Input P_{RV} , while the rms of the Output M_{RV} height map differed from the Input M_{RV} by 5%.

On the other hand, more significant changes were observed between the output and input RI components. After the addition of 10% random machine errors, the Shift technique incorrectly solved for the RI components of the part and machine. There was a 60% rms deviation between the Output and Input P_{RI} height maps, and a 900% rms deviation between the Output and Input M_{RI} height maps. Naturally, these large deviations in the RI components, got transferred to the estimate of the part (without machine error contributions). The rms of this part estimate differed from its corresponding input by 40%.

The differences between these output- and input-separated components can be seen as height maps, after subtracting the inputs in Figure 2.25 (*left*) from the outputs in Figure 2.25 (*right*). These difference height maps, which result from the addition of 10% random machine z-axis errors, are shown in Figure 2.26. Comparing the rms values (or the peak-to-valleys) of the RV differences, to those of the RI differences, shows that the addition of the 10% random machine z-axis errors, had negligible effect on the separation of the RV components but had a significant effect on the separation of the RI components. The summary in Chapter 2.6.2 explains why.

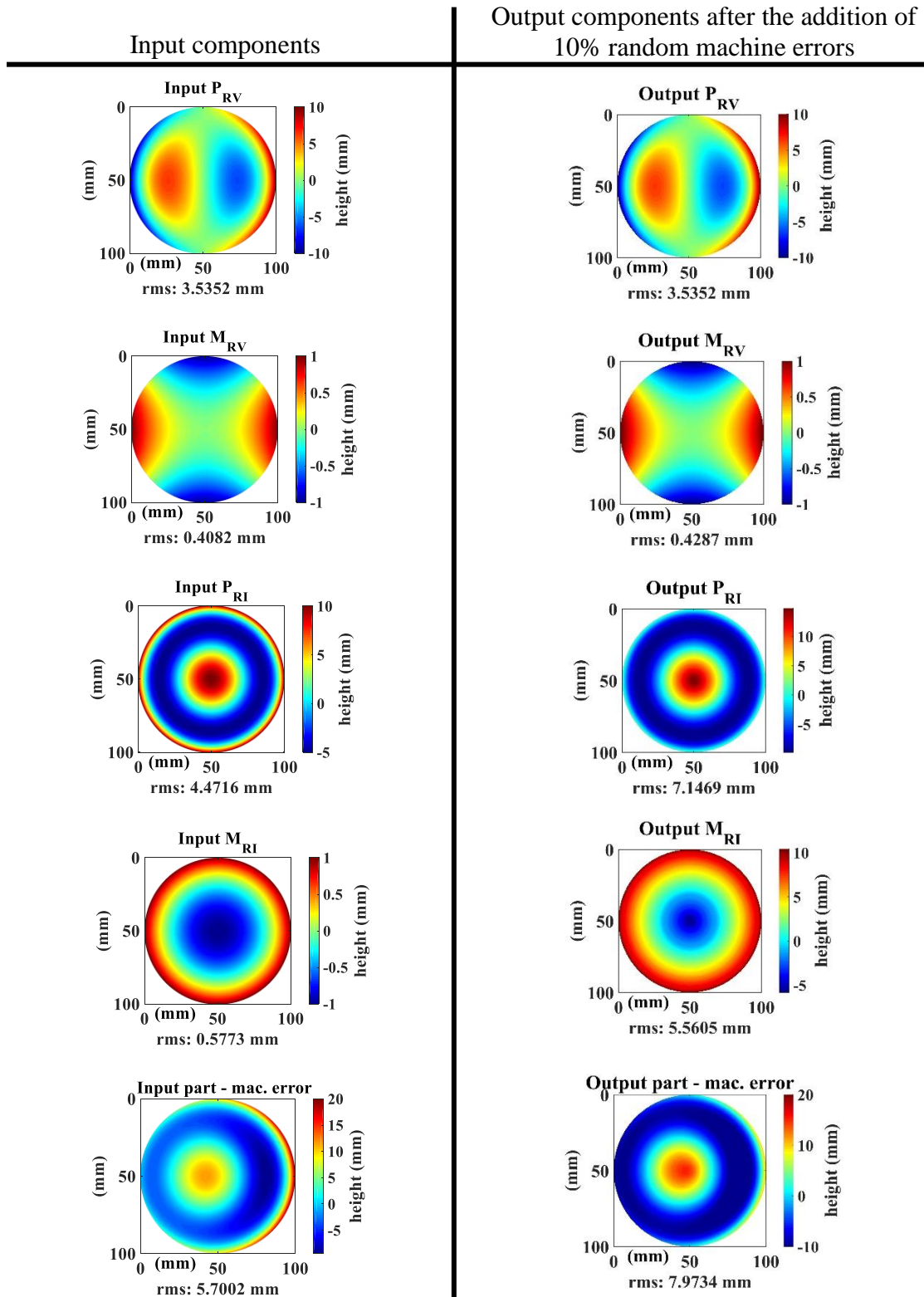
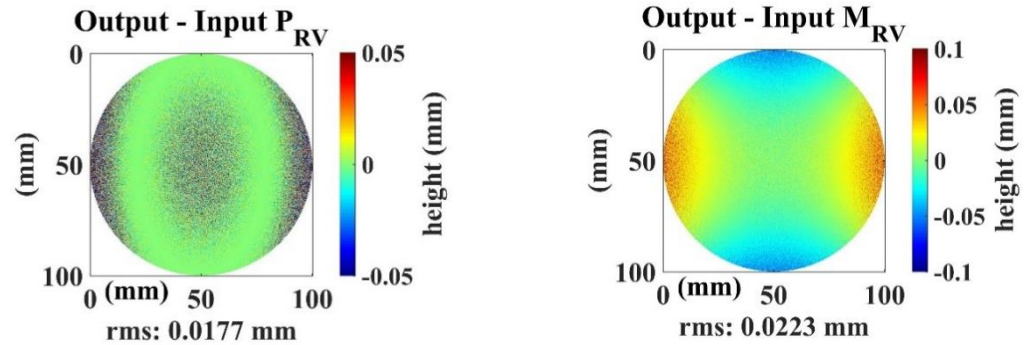


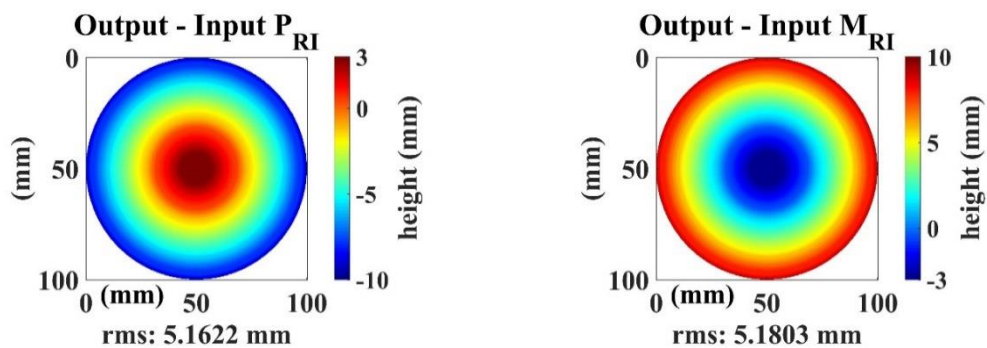
FIGURE 2.25 Input components to the Shift-Rotation technique (*left*). Output components obtained after the addition of random z-axis machine errors with maximum amplitudes of 10% deviation from the nominal (*right*).

Differences between output and input surface components, after the addition of 10% random machine z-axis errors

Differences between rotationally varying components



Differences between rotationally invariant components



Difference between output and input best estimates of the part

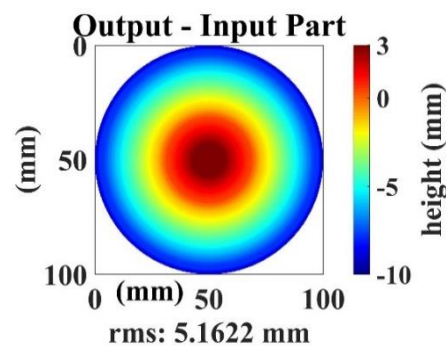


FIGURE 2.26 Differences between output and input surface components, after the addition of 10% random machine z-axis errors.

2.6.2 Summary of the Influences of Random Machine Errors

Random machine z-axis errors with maximum amplitudes of 10%, 1%, 0.1%, and 0.01% the nominal systematic machine errors, were added to simulated measurements of the part (results from the 1%, 0.1%, and 0.01% deviations are in Appendix B). The effects of these added errors on the Shift-Rotation error separation process were observed by comparing the error-separation outputs, to their corresponding inputs. The rms deviations between the output components and their corresponding inputs are summarized as percentages in Table 2.3 and graphed in Figure 2.27.

TABLE 2.10 Effects of added random z-axis machine errors on separated surface components.

		Maximum random errors added to the machine			
		+10%	+1%	+0.1%	+0.01%
RMS deviations (%)	Output – Input P _{RV}	0.5007	0.0509	0.0057	0.0006
	Output – Input M _{RV}	5.4630	0.6614	0.3920	0.3920
	Output – Input P _{RI}	115.44	6.3892	0.3824	0.0649
	Output – Input M _{RI}	897.33	49.091	2.9274	0.4850

The blue and black lines in Figure 2.27 represent the deviations between input and output RV components, while the red and green represent deviations between input and output RI components. The figure shows that random z-axis machine errors have a greater impact on the separation of RI components than on RV components because the N-Rotation averaging is noise-tolerant, but the Shift-technique is noise-sensitive as explained below.

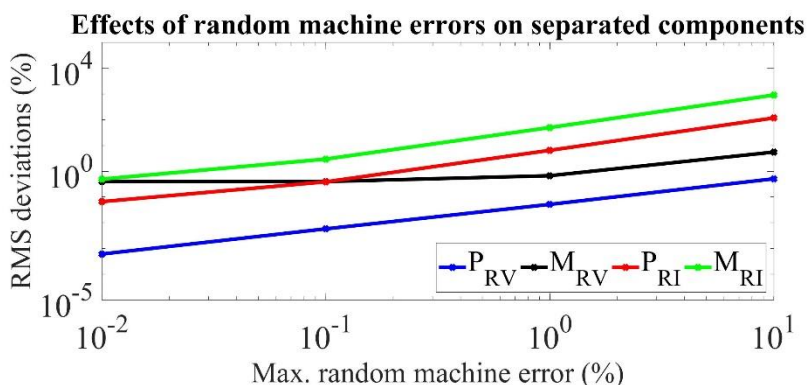


FIGURE 2.27 Effects of added random z-axis machine errors on separated surface components.

In all four cases (maximum machine errors of 10%, 1%, 0.1%, and 0.01% nominal), the N-Rotation technique correctly solved for the RV components of the part; the solutions of the Output P_{RV} were insensitive to random z-axis errors in the machine. Also, the N-Rotation technique had no trouble solving for the RV components of the machine errors. In the four cases, the separated Output M_{RV} maps changed slightly, because of the RV components of the added random machine errors. These reiterate that the N-Rotation technique is very tolerant to noise.

On the other hand, in the presence of large random machine errors, the Shift technique had trouble solving for the RI component of the part. Reduction in the amplitudes of the simulated random machine z-axis errors led to improved error separations from the Shift-Technique. This points to the Shift-technique's sensitivity to noise. This noise-

sensitivity of the Shift-technique arises because, in calculating the slope of the part, the equations (and the design matrix) assume that all machine errors have been cancelled out, leaving behind the slope of the part, a difference between part radial profiles, only. For example, in the Shift-technique, if two measurements of a part, before and after a lateral translation of the part, are MP^0 and MP^Δ , respectively, they can be represented as:

$$MP^0 = P^0_{RV} + P^0_{RI} + M^0_{RV} + M^0_{RI} \quad (2.15)$$

$$MP^\Delta = P^\Delta_{RV} + P^\Delta_{RI} + M^0_{RV} + M^0_{RI} \quad (2.16)$$

MP^0 represents a measurement of the part in an initial position, while MP^Δ represents a measurement after translating the part by a distance, Δ . A difference between these two measurement results, Equations 2.15 and 2.16, gives the slope of the part as shown in Equation 2.17.

$$MP^\Delta - MP^0 - (P^\Delta_{RV} - P^0_{RV}) = P^\Delta_{RI} - P^0_{RI} \quad (2.17)$$

Equation 2.17 (and subsequently, the design matrix) expects all machine errors to cancel out after the subtractions. The introduction of random z-axis machine errors unbalances this equation and explains why the Shift technique is very sensitive to random noise. Considering this, it is advisable to filter out measurement noise before applying Shift-Rotation error separations.

2.7 Summary

Simulations were used to describe an in-situ self-calibration technique, Shift-Rotation, which minimizes task-specific uncertainty in freeform measurements by separating machine error contributions from part surface measurements. The simulated

surface measurements were decomposed into four output height maps: rotationally varying (RV) component of the part, rotationally invariant (RI) component of the part, RV and RI components of the machine errors. From these separations, a combination of the separated part components represented a simulated measurement of the part without machine error contributions. The task-specific machine error contributions were then obtained by the sum of the separated machine error components.

Simulations were also used to investigate the influence of random machine z-axis errors on the error separation process. The influence of machine errors that change systematically in the z-direction were not simulated. If these are present in a measuring machine, the machine errors would be different between rotated freeform part measurements. Nonetheless, the Shift-Rotation would separate these errors as rotationally varying machine error components. The simulations showed random z-axis machine errors have a greater impact on the separation of RI components than on RV components, indicating the N-Rotation averaging is noise-tolerant while the Shift-technique is noise-sensitive.

CHAPTER 3: MONTE CARLO UNCERTAINTY ESTIMATIONS

This chapter evaluates task-specific uncertainties associated with applying the Shift-Rotation technique to measurements of freeform surfaces. Several methods exist to estimate the uncertainty in CMM measurements and Wilhelm et al. [85] divided these methods into six categories: sensitivity analysis, expert judgement, experimental method using calibrated objects, computer simulation, statistical estimations from measurement history, and hybrid methods. Computer simulations were used in this project to evaluate task-specific uncertainties.

The simulation methods that estimate task specific uncertainty begin with some model of the machine and measurement process. These methods include the “Virtual CMM” (VCMM) [86-88], “Virtual Instrument” [89], “Simulation by Constraints” [90], the “Expert CMM” [91], and Monte Carlo simulation [92]. The VCMM performs a point-by-point simulation of measurements, emulating the measurement strategy and physical behavior of the CMM with the dominating uncertainty contributions. The results from simulated measurements, with and without the uncertainty influences, are compared to yield the measurement uncertainty specific for each measurand. These uncertainty influences consist of known systematic influences, unknown systematic influences, and random influences, which are assessed either by measurements or by estimations. The simulations take these effects into account by performing each virtual measurement several times [86].

Simulation by constraints is a generalization of the VCMM that simulates CMMs by generating all possible sets of parametric errors within known constraints. The Expert CMM is a modified version of a VCMM that computes the uncertainty of individual point coordinates and propagates this uncertainty through the part program to obtain the final uncertainty of the measurand [86].

The uncertainty evaluations in this project were carried out using Monte Carlo, a computer simulation method that can evaluate uncertainty contributions from various sources. The Monte Carlo simulation also began with some model of the machine and measurement process and the uncertainty evaluations were grouped into three main stages: formulation, propagation, and summarizing [93].

The formulation stage defined an output quantity to be measured, referred to as the measurand. In these simulations, the simulated measurement height map of the part, after removal of the machine's error contributions, was the measurand. From this height map, additional measurands can also be extracted, for example, amplitude representations of the surface like rms, skew, kurtosis, and PVr [94], or spatial parameter such as autocorrelation length. Within the formulation stage, input quantities also need to be defined. These inputs are the quantities upon which the measurand depends. The input quantities used in this Monte Carlo simulation are some of the potential uncertainty sources associated with the Shift-Rotation error separation process. The uncertainties from these sources can be expressed as maps that show the spatial distribution of the uncertainty within the aperture, and some of these uncertainty sources are listed in Table 3.1.

TABLE 3.1 Potential sources of uncertainty associated with the Shift-Rotation process.

Uncertainty sources	Measurand	Output uncertainty
Rotation angles	A surface parameter evaluated by using the height map, Output P_{RV} + Output P_{RI} .	Task-specific uncertainty map
Translation distance		
Moving axis of rotation		
CMM parametric errors		
Electronic noise, Z-axis noise, and vibrations		

The Monte Carlo simulation is performed by building a model that generates many possible outcomes which could arise from the variations of input parameters. The measurement model defines the relationship between these input parameters and the measurand. Here, the measurement model relating the input quantities to the measurand is the Shift-Rotation process described in Chapter 2. This model was incorporated into the Monte Carlo simulation in a way that generated many possible outcomes which could arise from the distributions of input parameters. These distributions are governed by random selections within preassigned probability density functions (PDF). A PDF, $f(x)$, is the first differential coefficient of a distribution function, $F(x)$, with respect to x (where this differential exists). This can be written as $f(x) = \frac{d(F(x))}{dx}$. For a given random variable, X , the area between two points in the range, x_L and x_U , under the probability density curve, is equal to the probability that an as yet unrealized random number of X will

lie between the points x_L and x_U [95, 96]. These PDFs, for example, Gaussian or uniform distributions, are assigned to the inputs based on a priori knowledge of their characteristics [93]. Since the inputs are represented as PDFs, the Monte Carlo process reports the measurand with a joint PDF which depends on the PDFs of the input quantities, and on the measurement model.

This PDF report of the measurand, constitutes the propagation stage of the uncertainty evaluation. Here, the input PDFs propagate through the model to yield a joint PDF of the output quantity. This propagation process from the inputs, through the model, to the outputs, can be represented as shown in Figure 3.1 [93].

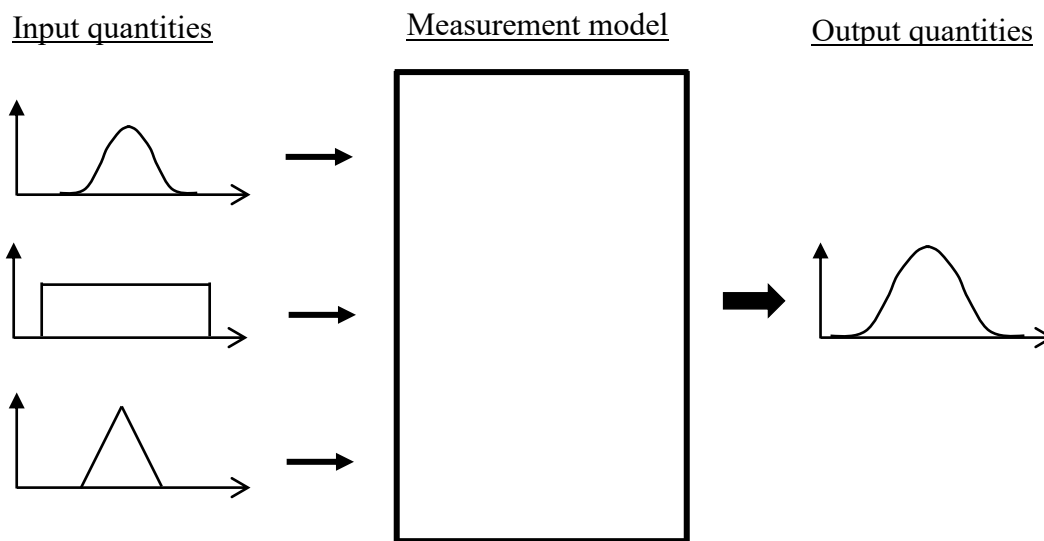


FIGURE 3.1 Propagation of uncertainty, through the measurement model, to the output.

The summary stage of the uncertainty evaluation involves obtaining an expectation of the measurand, as well as its uncertainty (reported with an appropriate coverage factor), from the joint PDF. In Chapter sections 3.1 – 3.4, different input parameters from Table

3.1 were used, separately, as inputs to the Monte Carlo. Each input parameter led to a standard uncertainty and from a combination of these standard uncertainties, a combined standard uncertainty was obtained under the assumption that no correlation existed between the standard uncertainties. Table 3.1 lists the potential uncertainty sources and the following sections show the Monte Carlo generation of standard uncertainty maps from these sources.

3.1 Uncertainty from the Rotation Angles

In this section, the Monte Carlo simulation will be illustrated by an example where the rotation angle is used as the input parameter. In the rotation technique discussed in Chapter 2.1, it was assumed that each rotation angle was an exact integer multiple of 90° . This led to a height map representation of the freeform surface without the machine's error contributions (Figure 2.17), and this height map was further represented by an amplitude parametric surface specification ($\text{rms} = 5.7003 \text{ mm}$). In using the Monte Carlo, instead of assuming we have perfect rotation angles, we presume that each rotation angle can fall anywhere within some distribution.

For example, the flowchart in Figure 3.2 shows the Monte Carlo simulation process when the rotation angle is used as the input parameter; and shows uniform distributions with upper and lower limits of $\pm 0.05^\circ$ used around each nominal rotation angle. Uniform distributions were chosen to represent the rotation angle (random distribution) because each point within the rotation angle's range had an equal probability. The upper and lower limits of $\pm 0.05^\circ$ were chosen for convenience to show the effect, not to indicate the likely consequence on the specific measurements discussed in later chapters.

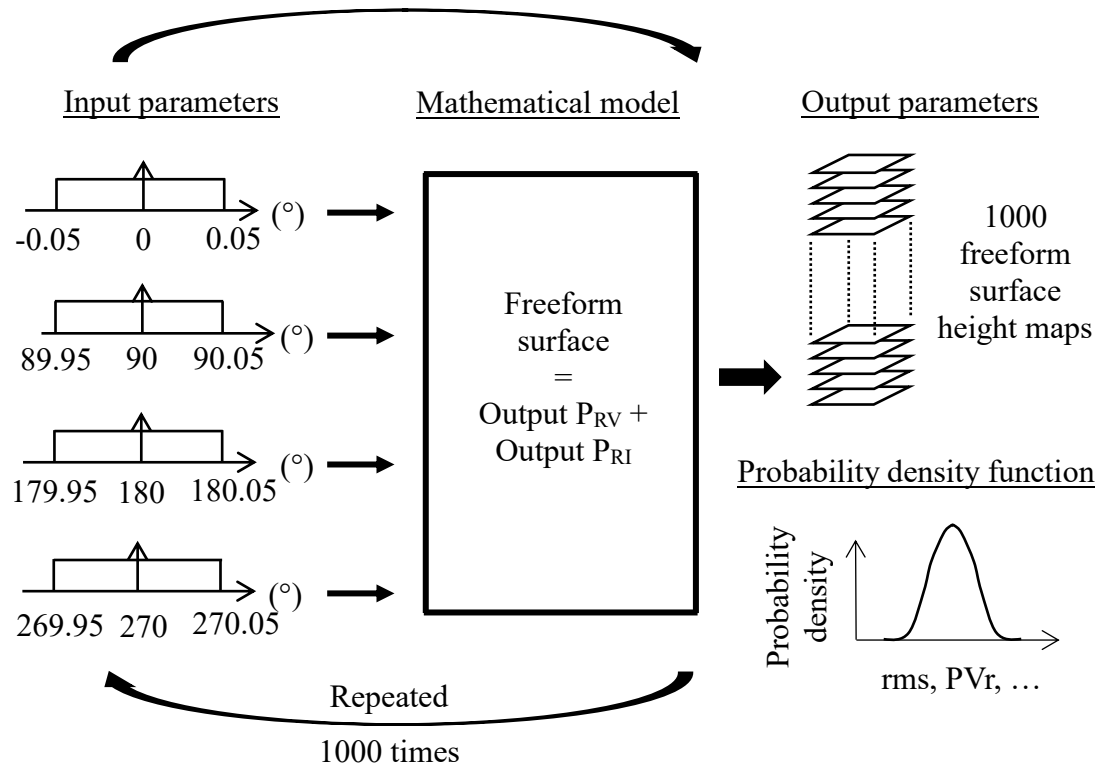


FIGURE 3.2 A flowchart of the Monte Carlo process, with rotation angle as the input parameter.

The flowchart in Figure 3.2 shows the Monte Carlo simulation process when the rotation angle was used as the input parameter. In one forward loop, four random rotation angles were selected (one from each of the uniform distributions). Instead of using the nominal rotation angles, these four random angles were used as the input rotation angles in the Monte Carlo's Shift-Rotation process. This then resulted in one output height map representation of the part (Output P_{RV} + Output P_{RI}), and any amplitude parametric description (for example, rms, PVr , roughness average, etc.).

After running the Monte Carlo loop many times, such that each trial had random angles from the input distributions, an array of possible outcomes of the freeform surface measurement was obtained. The average of the height maps in this array, when compared

with the best estimate part in Figure 2.17, gave an estimate of how well the Monte Carlo converged, while the standard deviation across the array led to a standard uncertainty. The standard uncertainty, u , was calculated from [97]:

$$u = \frac{s}{\sqrt{n}} \quad , \quad (3.1)$$

where n was the number of possible outcomes in the array, and s was the standard deviation across the array of possible outcomes, expressed as:

$$s = \sqrt{\frac{\sum_{i=1}^n (x_i - \bar{x})^2}{(n - 1)}} \quad (3.2)$$

After this process was applied to the simulated height maps from the previous sections, the Monte Carlo converged to the height map shown in Figure 3.3 (*left*). Since the best estimate part measurement shown in Figure 2.17, reports an rms of 5.7003 mm, Figure 3.3 (*left*) shows the Monte Carlo converged to approximately one part in 50,000. The standard uncertainty in the best estimate of the output part, because of an uncertainty in the rotation angle, is shown as the map in Figure 3.3 (*right*). This uncertainty is a map,

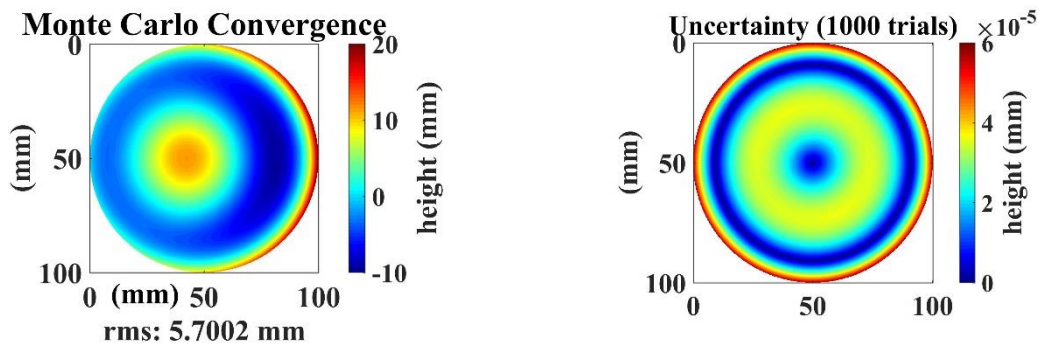


FIGURE 3.3 The convergence of the Monte Carlo to the freeform part height map (*left*). The uncertainty in the best estimate measurement, because of an uncertainty in the rotation angles (*right*).

the same size and data density as the measurand, and shows the spatial distribution of the uncertainty in the measurand because of uncertainty in the rotation angles.

The amplitude parametric representation of the possible measurement outcomes in the array, was expressed as the probability distribution in Figure 3.4.

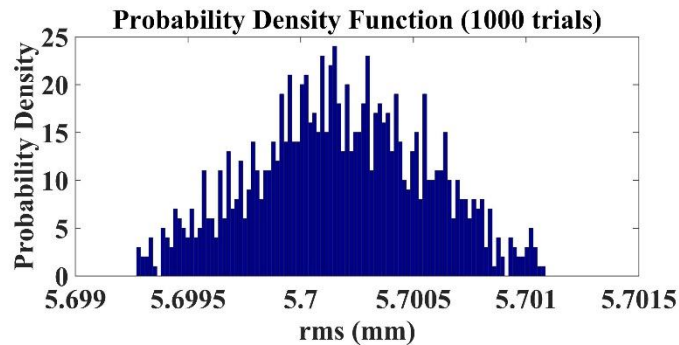


FIGURE 3.4 Amplitude parametric representation of the 1,000 trials in the Monte Carlo, reported as: $\text{rms} = 5.7001 \pm 0.00003 \text{ mm}$.

The uncertainty map shown in Figure 3.3 (*right*), was obtained from an uncertainty in the rotation angles, only. The next section estimates uncertainty contributions from of a moving axis of rotation.

3.2 Uncertainty from a Moving Axis of Rotation

In separating the RV component of the part, multiple measurements of the part were made after the part was rotated about an optical axis. Ideally, this rotation axis should be constrained against translations in the plane perpendicular to the axis of rotation. However, if the rotation axis of the part is not aligned to that of the rotary stage, the rotations of the part might not be about a fixed point. This section estimates uncertainty contributions which arise because of this moving axis of rotation.

The freeform part rotations shown in Figure 2.3 were simulated about a common axis of rotation. An example showing freeform part rotations about a moving axis is shown in Figure 3.5. Here, the moving axis can be observed, between rotations, by the inconsistent spacing between the freeform part and the surrounding box of each graph.

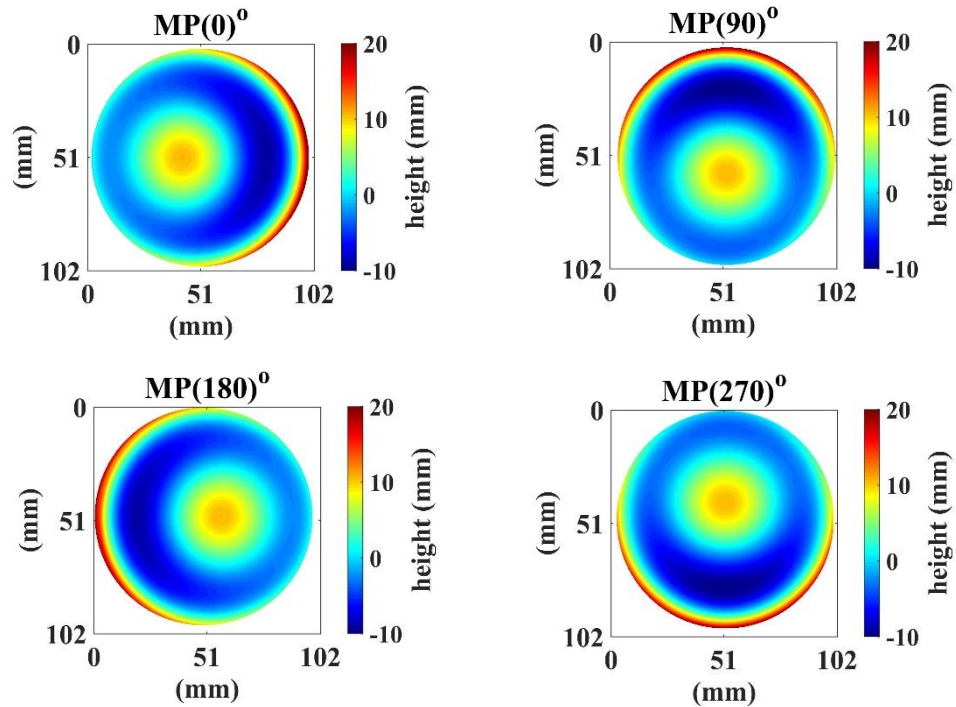


FIGURE 3.5 Depictions showing rotations of the part about a moving axis of rotation.

To estimate uncertainty contributions from a moving axis of rotation, this moving axis was used as an input parameter to the Monte Carlo simulation. In these simulations, it was assumed that the part translated in the plane perpendicular to the axis of rotation. Uncertainty contributions that might arise because of tip/tilt about the optical axis were not considered.

Between rotations, the rotation axis translated freely and randomly within a square region with a 300- μm length (3-pixel square). Figure 3.6 depicts the freeform part and the allowed translations. The dashed lines on the periphery show the upper and lower limits of

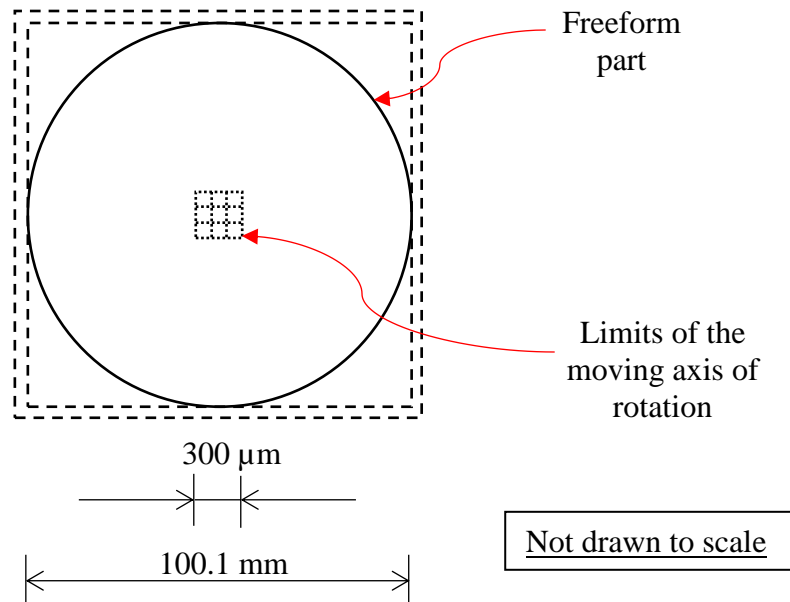


FIGURE 3.6 Depiction of the freeform part allowed to translate randomly within a 300 μm square region (3-pixel square).

the allowed part translation, while the dashed lines in the center show the bounds of the allowed optical axis translation. As a reminder, the freeform part was simulated on a matrix grid with a 1001-pixel aperture diameter.

With the rotation axis as the input parameter, a Monte Carlo simulation like the flowchart described in Figure 3.2 was used to estimate the uncertainty contributions from the moving rotation axis. In one forward loop, each rotation of the part had a rotation axis whose position was random within the 300- μm square center. This resulted in one possible output of the part (Output P_{RV} + Output P_{RI}). Then, after many Monte Carlo iterations, the Monte Carlo converged to the height map shown in Figure 3.7 (*left*). Since the best estimate

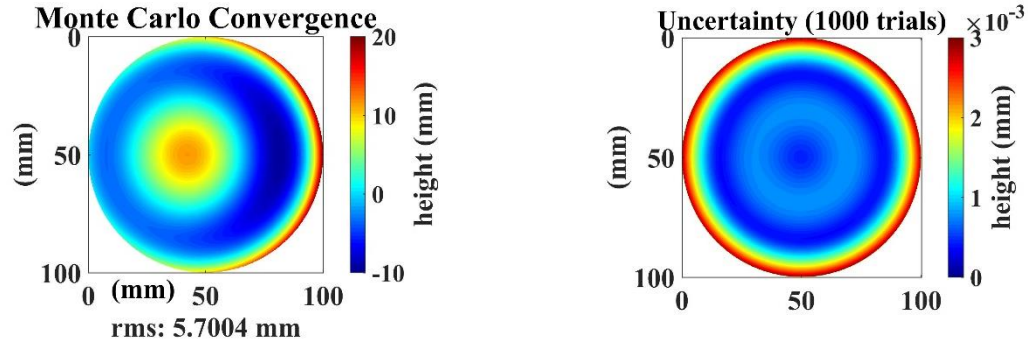


FIGURE 3.7 The convergence of the Monte Carlo to the estimated measurement of the freeform part, because of an uncertainty in the axis of rotation (*left*). The uncertainty in the best estimate measurement, because of an uncertainty in the axis of rotation (*right*).

part measurement shown in Figure 2.17, reported an rms of 5.7003 mm, Figure 3.7 (*left*) shows the Monte Carlo converged to approximately one part in 50,000. The standard uncertainty in the estimate of the output part, because of an uncertainty in the rotation axis, is shown in Figure 3.7 (*right*). This shows the uncertainty in the estimate of the measurand because of an uncertainty in the location of the rotation axis.

In solving for the RI component of the freeform part, one or more translations of the part are required. These translation distances are possible sources of uncertainty; therefore, the next section uses Monte Carlo analyses to estimate uncertainty contributions from translation distances.

3.3 Uncertainty from the Translation Distance

In Chapter 2.2, simulated measurements of the part were made, before and after it was laterally shifted by a known translation distance, Δ , with respect to the machine. A translation distance of 2 mm was used in the simulations. To estimate its uncertainty contributions, the translation distance was used as the input parameter to the Monte Carlo, and a uniform distribution was used around the nominal value. This uniform distribution is depicted in Figure 3.8 with upper and lower limits of $\pm 200 \mu\text{m}$ (± 2 pixels).

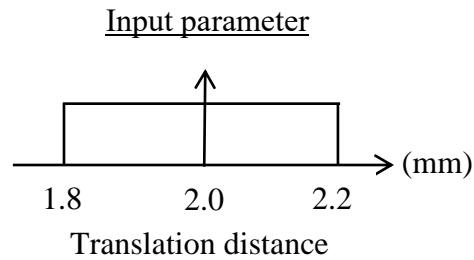


FIGURE 3.8 Uniform distribution around the translation distance.

Instead of using an exact translation distance of 2 mm, the translation distance randomly fell anywhere within the uniform distribution. From a random translation distance, the Monte Carlo generated a possible output of the freeform surface (Output P_{RV} + Output P_{RI}). This was then repeated 1000 times to yield 1000 possible outputs. From these outputs, the Monte Carlo converged to the output part shown in Figure 3.9 (*left*). The rms of this graph shows the Monte Carlo converged to 2 parts in 50,000. Also from the 1000 possible outputs, the standard uncertainty in the best estimate output part is shown as the map in Figure 3.9 (*right*).

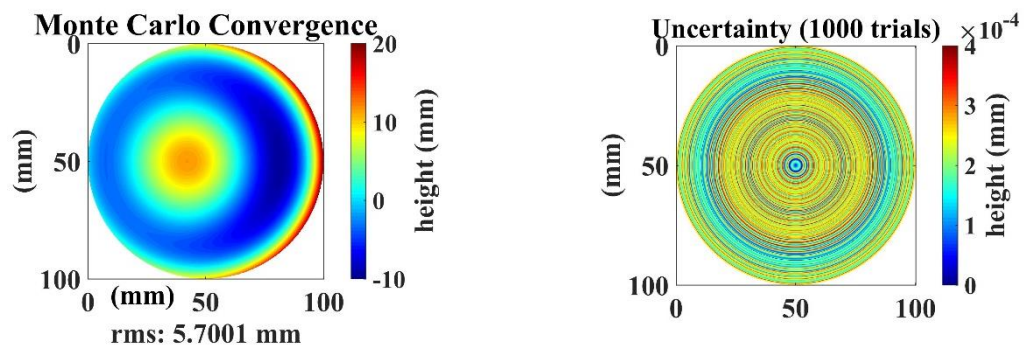


FIGURE 3.9 The convergence of the Monte Carlo to the estimated measurement of the freeform part, because of an uncertainty in the translation distance (*left*). The uncertainty in the best estimate measurement, because of an uncertainty in the translation distance (*right*).

3.4 Uncertainty from Electronic Noise and Vibrations

The next uncertainty contributor to be assessed was electronic noise and vibrations which are likely to be present in CMMs and other measuring machines. Before noise was added to the Monte Carlo simulation, the intrinsic noise present within the Monte Carlo software was investigated. This was done by running the Monte Carlo simulation 100

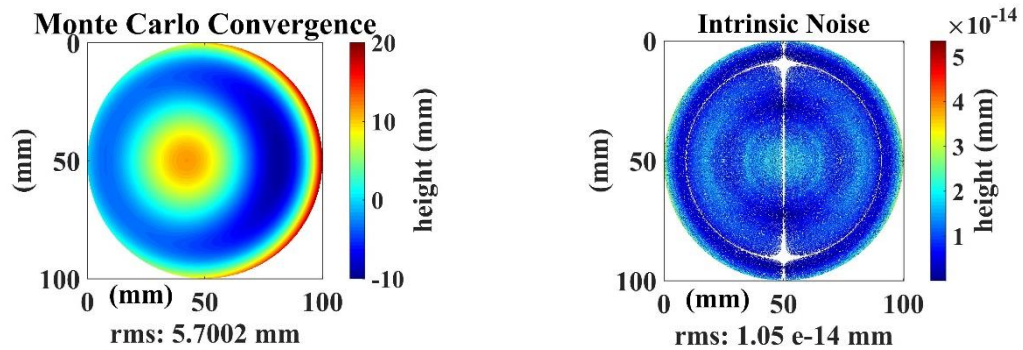


FIGURE 3.10 Monte Carlo convergence from 100 trials with nominal input parameters (*left*). Intrinsic noise present in the Monte Carlo software, obtained from the 100 trials (*right*).

times, with all input parameters fixed at nominal values (no added uncertainties). These 100 trials generated 100 possible outputs of the freeform surface (Output P_{RV} + Output P_{RI}), and the standard uncertainty of these outputs was used to quantify the intrinsic noise as shown in Figure 3.10 (*right*).

This intrinsic noise stems from the precision of the computational software and serves as an indication of the threshold, above which the forthcoming simulated electronic noise should lie. The next step involved adding noise to the Monte Carlo. To simulate electronic noise and vibrations, ± 15 nm uniformly distributed random noise was generated, and an example of this noise is shown in Figure 3.11.

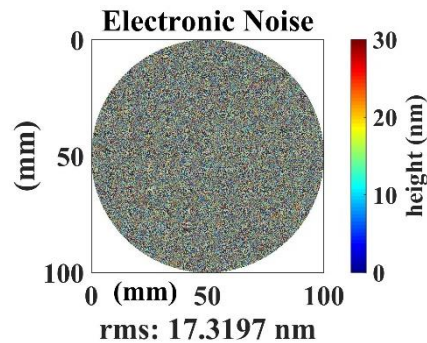


FIGURE 3.11 A simulated electronic noise to be added to the Monte Carlo simulations.

Random versions of this noise were then added to all simulated part measurements, input to the Monte Carlo. All the input parameters were at their nominal values, but every

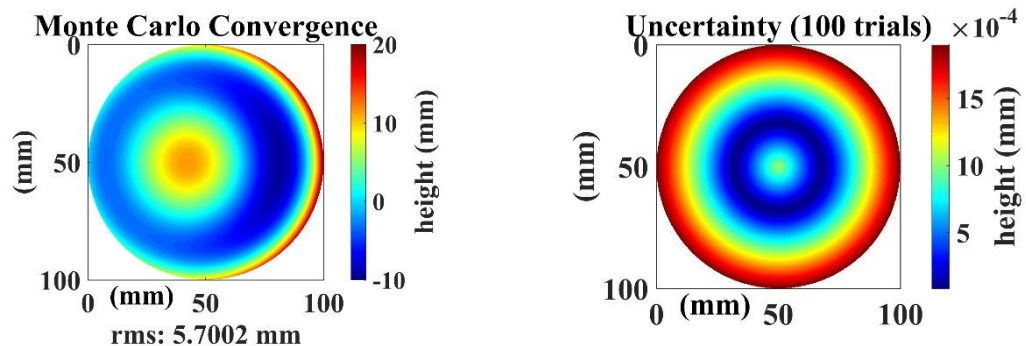


FIGURE 3.12 Monte Carlo convergence after the addition of 30 nm P-V random noise to the input parameters (*left*). The output noise because of the random 30-nm P-V input noise (*right*).

simulated part measurement had an added ± 15 nm random noise. The Monte Carlo was run 100 times and from the outputs, converged as shown in Figure 3.12 (*left*). The

uncertainty from these outputs is shown in Figure 3.12 (*right*) and depicts the noise output of the Monte Carlo software because of the ± 15 nm uniformly distributed noise.

The bulk of the output noise shown in Figure 3.12, stems from the RI portion of the Monte Carlo / Shift-Rotation algorithm. To double-check, before arriving at the noise outputs above, the noise output from the RV portion was that shown in Figure 3.13. This further confirms the noise tolerance of the N-rotation technique and shows the sensitivity of the RI-shift technique to added noise.

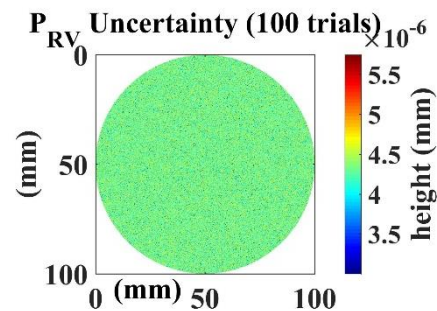


FIGURE 3.13 Output noise from the RV portion of the Monte Carlo software.

3.5 A Combined Standard Uncertainty

The standard uncertainty estimations can be summarized as shown in Figure 3.14. Figure 3.14 (*left*) shows the measurand, which is the best estimate freeform surface (Output $P_{RV} + \text{Output } P_{RI}$), while Figure 3.14 (*right*) shows the standard uncertainties obtained from the Monte Carlo simulations.

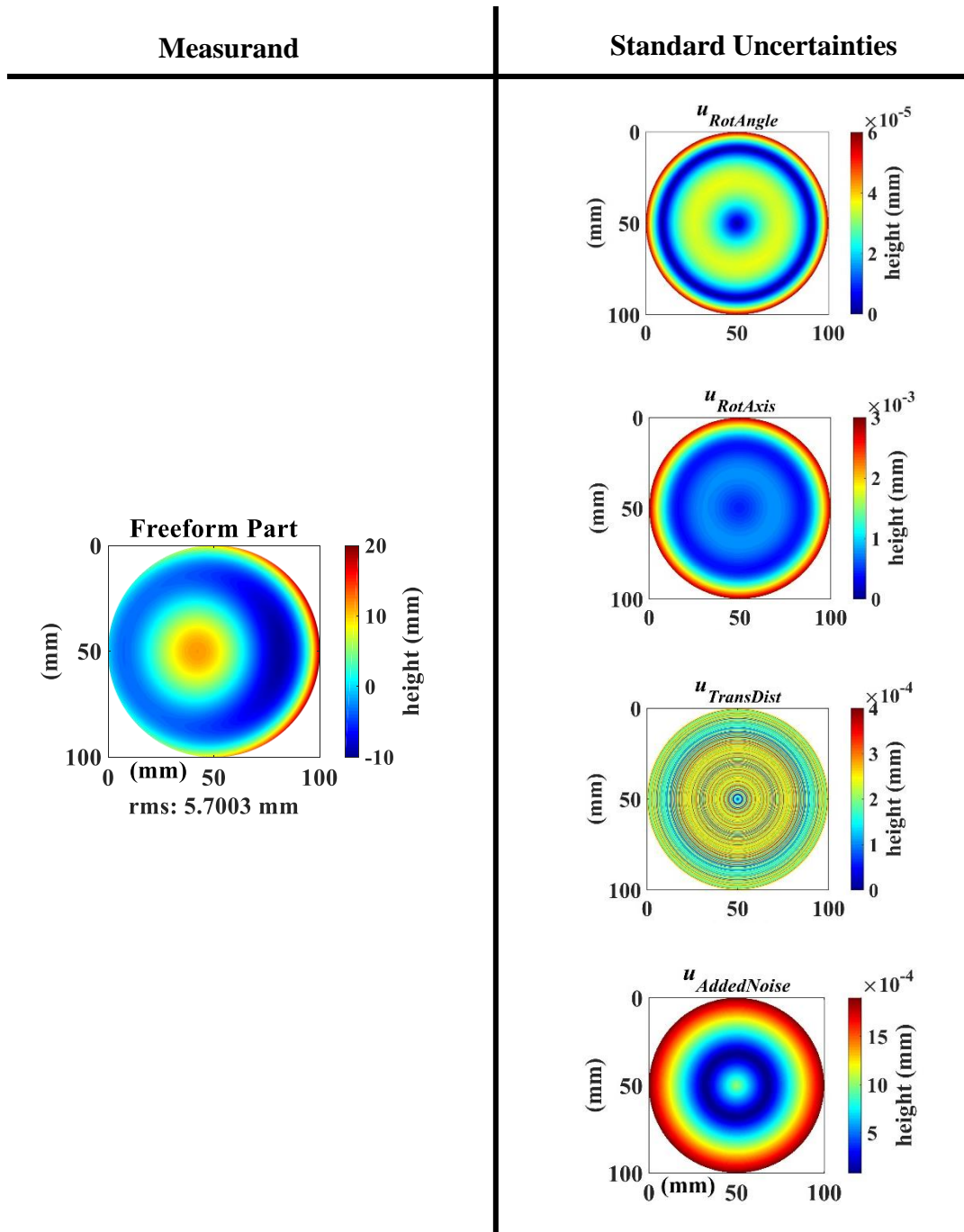


FIGURE 3.14 The best estimate of the freeform surface (*left*) and its standard uncertainties (*right*).

The standard uncertainty, $u_{RotAngle}$, represents the uncertainty after each nominal rotation angle randomly varied within upper and lower limits of $\pm 0.05^\circ$. The standard

uncertainty, $u_{RotAxis}$, represents the uncertainty after the rotation axis of every simulated part (in the N-rotation technique) fell anywhere within a 300- μm square center. The standard uncertainty, $u_{TransDist}$, represents the uncertainty after the nominal translation distance (in the RI-Shift technique) varied randomly within upper and lower limits of 200 μm . The standard uncertainty, $u_{AddedNoise}$, represents the Monte Carlo's output response to random ± 15 nm uniformly distributed noise.

With the assumption that the above standard uncertainties were uncorrelated, a combined standard uncertainty, u_C was obtained from their root sum of squares [97] as shown in Equation 3.3.

$$u_C = \sqrt{(u_{RotAngle})^2 + (u_{RotAxis})^2 + (u_{TransDist})^2 + (u_{AddedNoise})^2} \quad (3.3)$$

This combined standard uncertainty is shown alongside the measurand in Figure 3.15 reported with a 95th percentile coverage probability ($k = 2$).

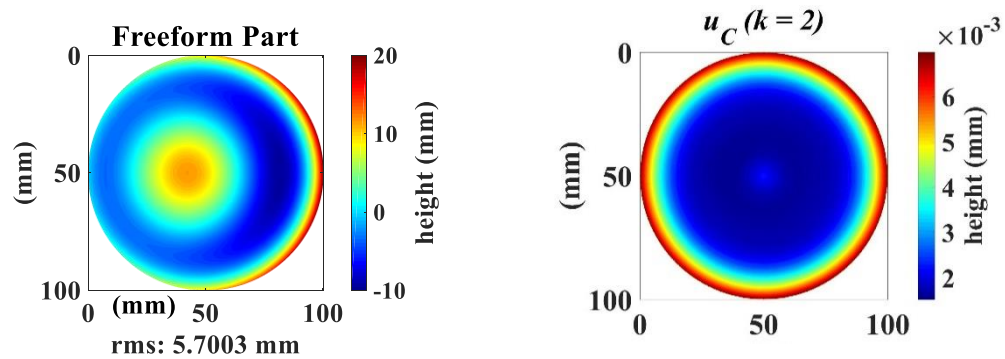


FIGURE 3.15 The best estimate of the freeform surface (*left*) and its combined standard uncertainty (*right*).

3.6 Summary

Monte Carlo simulations were used to evaluate task-specific uncertainties from sources associated with applying the Shift-Rotation technique to measurements of freeform surfaces. The best estimate of the freeform surface was used as the measurand while the inputs to the Monte Carlo were these potential sources of uncertainty: the rotation angles, a moving axis of rotation, the translation distance, and electronic noise and vibration. From the Shift-Rotation model described in Chapter 2, the Monte Carlo generated many possible outcomes which could arise from variations of the input parameters. For each input parameter, a standard uncertainty map was obtained from the many possible outcomes; these standard uncertainties were expressed as maps that showed the spatial distribution of the uncertainty within the aperture.

The standard uncertainty in the rotation angle represented the uncertainty after each nominal rotation angle randomly varied within upper and lower limits of $\pm 0.05^\circ$. The standard uncertainty in the rotation axis represented the uncertainty after the rotation axis of every simulated surface (in the N-rotation technique) translated freely within a 300- μm square center. The standard uncertainty in the translation distance represented the uncertainty after the nominal translation distance (in the RI-Shift technique) varied randomly within upper and lower limits of 200 μm . The standard uncertainty in the electronic noise represented the Monte Carlo's output response to random ± 15 nm uniformly distributed noise. With the assumption that these standard uncertainties were uncorrelated, a combined standard uncertainty was obtained from their root sum of squares and reported (with a 95th percentile coverage probability) alongside the measurand.

CHAPTER 4: ERROR SEPARATION OF MID-SPATIAL FREQUENCIES

The Shift-Rotation error separation technique is a form metrology; it is suited to separating low-spatial frequency surface components. Besides form, optical surfaces also comprise roughness and mid-spatial frequency components. This chapter investigates how the Shift-Rotation technique separates some mid-spatial frequencies that could be left behind by some sub-aperture fabrication processes.

In the frequency domain, one tool that shows the power of the spatial frequency components present on a surface, against the spectrum of spatial frequencies, is the power spectral density function (PSD) [98]. An example of a PSD graph is shown in Figure 4.1 [98]. The demarcations between these three frequency groups are user-defined spatial frequency cutoffs: a transition between form and mid-spatial frequencies, and another between mid-spatial frequencies (MSF) and roughness [99].

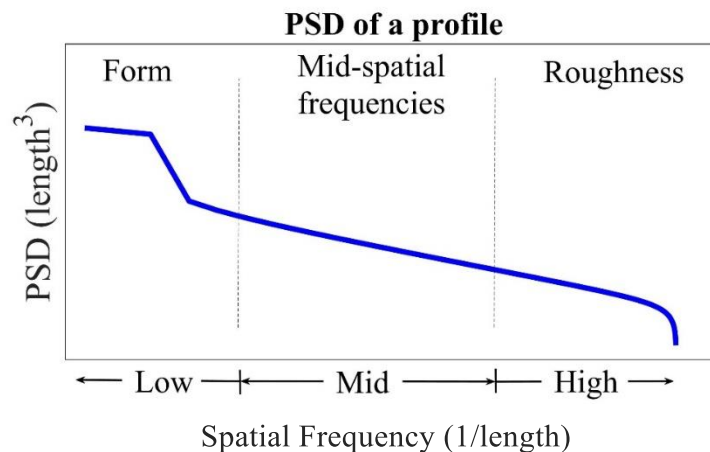


FIGURE 4.1 Separation of a profile into frequency bands.

In Chapter 2, the Shift-Rotation calibration technique was used to separate the surface components present in the simulated freeform surface shown in Figure 4.2.

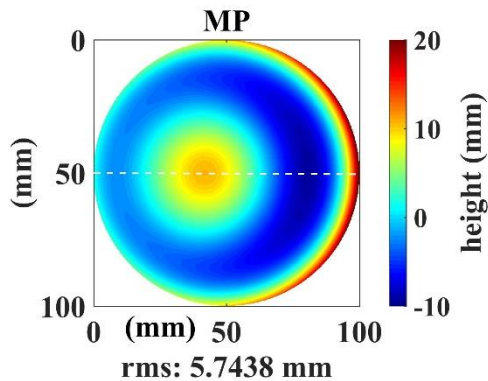


FIGURE 4.2 The freeform surface simulated with low-spatial frequency surface components.

This surface was simulated without MSF or roughness components, therefore, the Shift-Rotation separated components comprised of form, only. To show the spatial frequencies present on this surface, a horizontal profile was extracted (shown in dashed lines in Figure 4.2). This profile was transformed into the Fourier domain and its PSD was plotted in Figure 4.3.

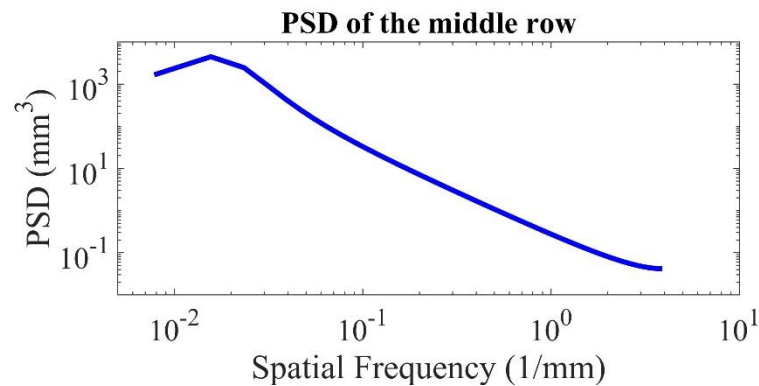


FIGURE 4.3 The PSD of a profile from the simulated freeform surface.

The graph shows no discernable mid-spatial frequencies or roughness components. To test the Shift-Rotation's error separation of mid-spatial frequency errors, the freeform surface was simulated to contain different mid-spatial frequency errors.

Since Shift-Rotation decomposes surfaces into rotationally varying (RV) and rotationally invariant (RI) components, the technique can thoroughly separate only mid-spatial frequency errors that can be classified as either purely rotationally varying or invariant. After the error separation, MSF components that are not classified as RV or RI, show up as residuals. The simulations in this chapter use very large amplitude MSF to highlight the consequences. The choice of MSF amplitudes and spatial frequencies were chosen to represent the effect, not the likely amplitude in state of the art freeforms. The simulations also use low values of N (number of rotational positions) during the error separations, meaning that there are many kN terms. The residual errors here will decrease as the number of rotational positions increase.

4.1 Error Separation of Sinusoidal Mid-Spatial Frequency Errors

Unidirectional scanning sub-aperture fabrication processes can leave behind sinusoidal or raster MSF errors [100, 101]. Shift-rotation error separations of these errors were simulated by generating the sinusoidal-distributed MSF error shown in Figure 4.4 (*left*). This contains 10 cycles across its aperture and was added to the simulated freeform surface in 4.4 (*right*).

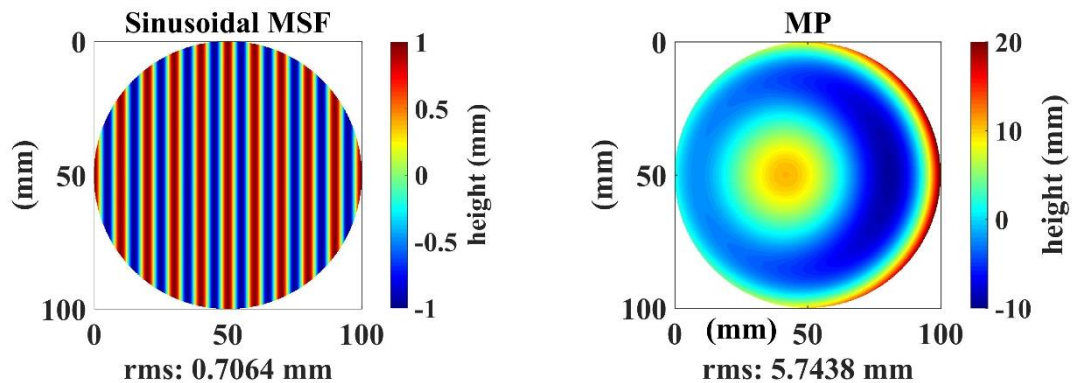


FIGURE 4.4 A simulated sinusoidal mid-spatial frequency error (*left*). The simulated freeform surface without mid-spatial frequency errors (*right*).

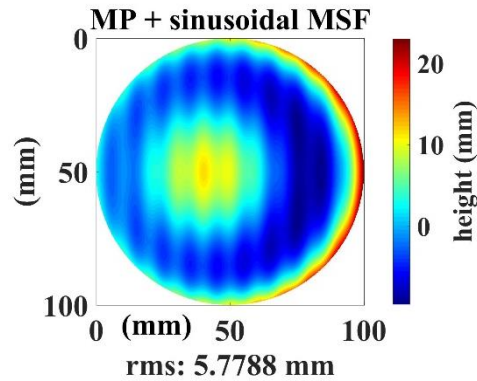


FIGURE 4.5 The freeform surface with a sinusoidal mid-spatial frequency error.

The freeform surface with the sinusoidal MSF error is shown in Figure 4.5. These mid-spatial frequency errors can be noticed in the frequency domain, after calculating the PSD of a central horizontal profile extracted from Figure 4.5. This PSD graph is shown in Figure 4.6.

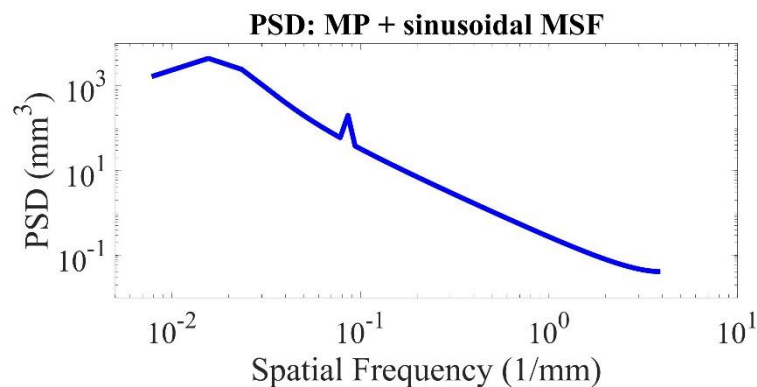


FIGURE 4.6 The power spectral density of the central horizontal profile, extracted from the simulated freeform surface with sinusoidal mid-spatial frequency errors.

The mid-spatial frequency peak observed around a spatial frequency of 0.1 cycles/mm, arises from the sinusoidal MSF error. Using the Shift-Rotation technique, the simulated freeform surface in Figure 4.5 was decomposed into four surface components: output P_{RV} , output M_{RV} , output P_{RI} , and output M_{RI} . For consistency, the error separation configuration (four part-rotations in the N-Rotation technique, and a 2-mm translation

distance in the Shift technique) applied in this chapter, was the same as that applied in the description of Shift-Rotation in Chapter 2. These separated components are shown in Figure 4.7. Output P_{RV} contains the rotationally varying components of the freeform surface, as well as the rotationally varying components of the sinusoidal MSF errors. Output M_{RV} contains the rotationally varying components of the machine error contributions. Since the sinusoidal MSF errors were added to the freeform surface, these did not show up in the Output M_{RV} map. As expected, the Output P_{RI} is a combination of

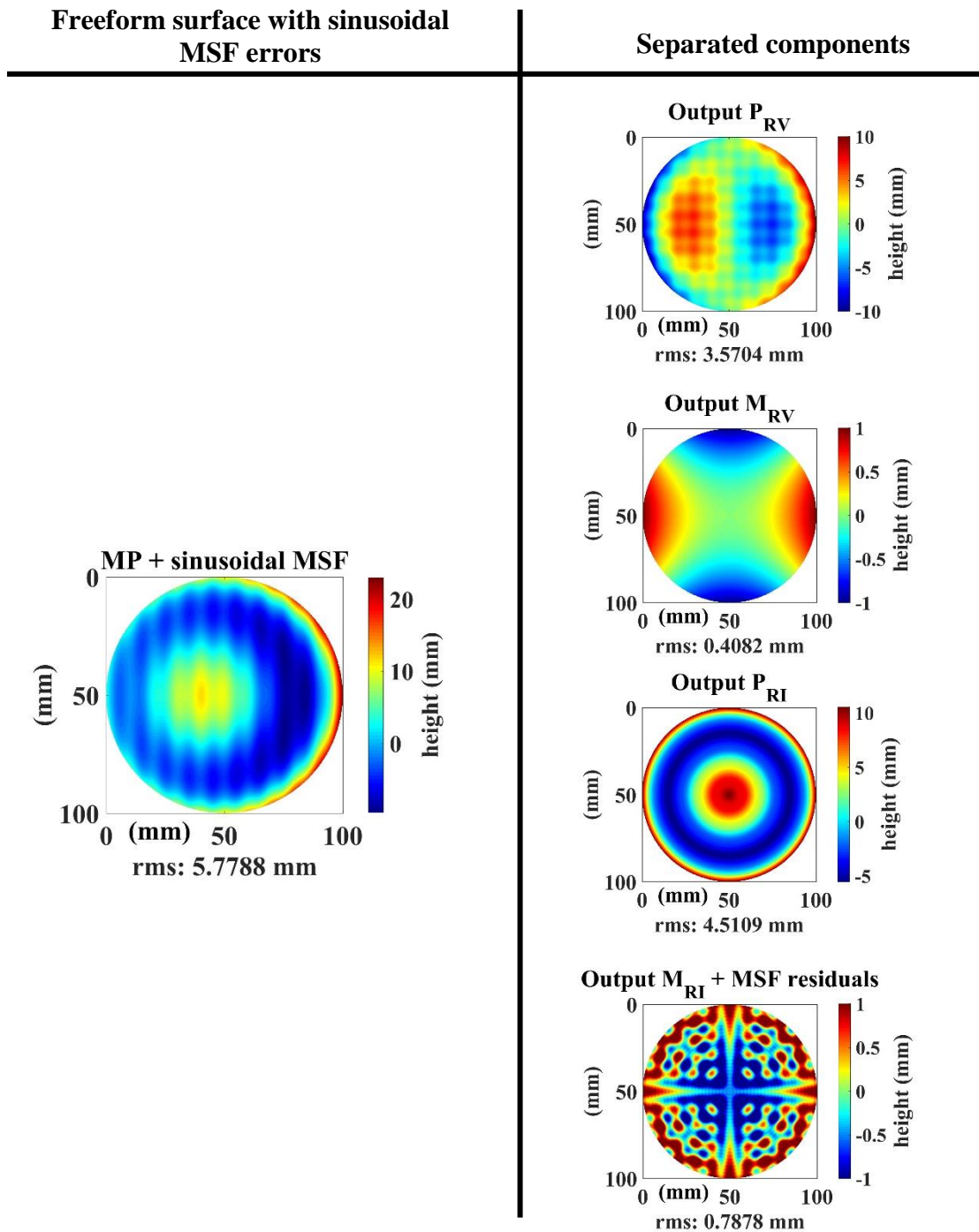


FIGURE 4.7 The simulated freeform surface with sinusoidal mid-spatial frequency errors (*left*). The Shift-Rotation separation of the freeform into four components (*right*).

the rotationally invariant components of the freeform surface, and the rotationally invariant components of the sinusoidal MSF errors. At this point in the error separation process, the sinusoidal MSF errors have been decomposed into an RV component (convolved with the

RV component of the freeform surface), and an RI component (convolved with the RI component of the freeform surface). The residual MSF components, which are neither purely RV nor RI, are convolved with the RI component of the machine errors, as shown in the fourth separated component in Figure 4.7. If sinusoidal or raster MSF errors are present on a freeform surface, Shift-rotation error separations of the measurement data would report the residual MSF errors convolved with the machine's RI errors. Additional information would be required to extract these residual MSF errors.

These residual MSF errors can be seen after the Shift-Rotation is applied to the sinusoidal MSF errors, only. Figure 4.8 shows this MSF error separation into its rotationally varying and rotationally invariant components. The MSF error components, which are not fully described as RV or RI, are shown as the residuals. The MSF error's RV component in Figure 4.8, was convolved with the RV component of the freeform surface in Figure 4.7. The MSF error's RI component in Figure 4.8, was convolved with the RI component of the freeform surface in Figure 4.7, while the MSF residuals in Figure 4.8, were convolved with the RI machine errors in Figure 4.7.

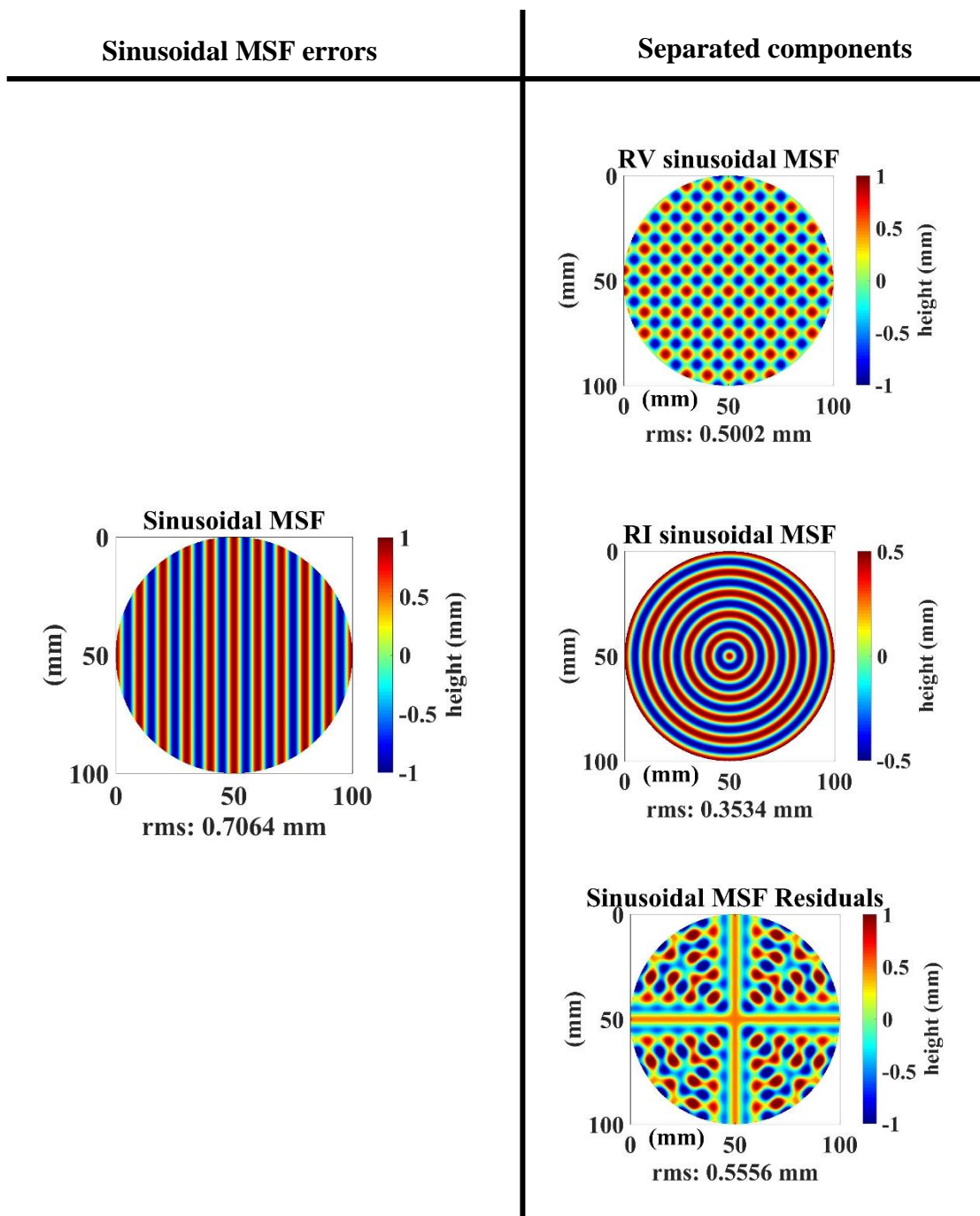


FIGURE 4.8 Sinusoidal mid-spatial frequency error (*left*). The Shift-Rotation separation of the mid-spatial frequency error, into rotationally varying, rotationally invariant, and residual components (*right*).

4.2 Error Separation of On-Axis Circular Mid-Spatial Frequency Errors

Besides raster mid-spatial frequency errors, another form of MSF error that can be added to a surface by fabrication and finishing processes, are spiral or other rotationally invariant MSF errors left behind by rotational sub-aperture tool paths [102]. These errors were simulated by generating on-axis circular MSF errors with single and multiple frequencies. Off-axis versions of these errors were also generated and error-separated.

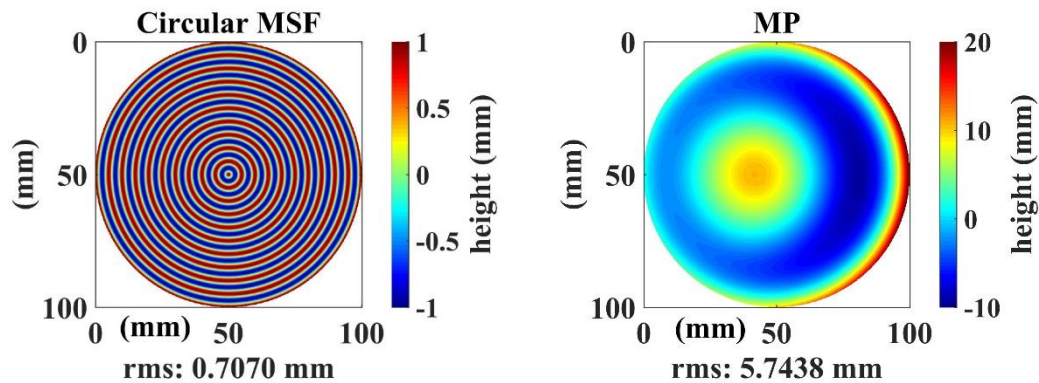


FIGURE 4.9 A simulated rotationally invariant mid-spatial frequency error (*left*). The simulated freeform surface without mid-spatial frequency errors (*right*).

Shift-rotation error separations of rotationally invariant MSF errors were simulated by generating the on-axis circular MSF error shown in Figure 4.9 (*left*). This was added to the simulated freeform surface in Figure 4.9 (*right*) and the resulting surface is shown in Figure 4.10.

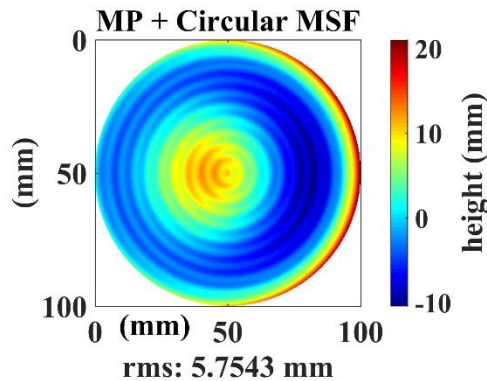


FIGURE 4.10 The simulated freeform with on-axis circular mid-spatial frequency errors.

These mid-spatial frequency errors can be noticed in the frequency domain, after calculating the PSD of a central horizontal profile extracted from the surface in Figure 4.10.

This PSD graph is shown in Figure 4.11.

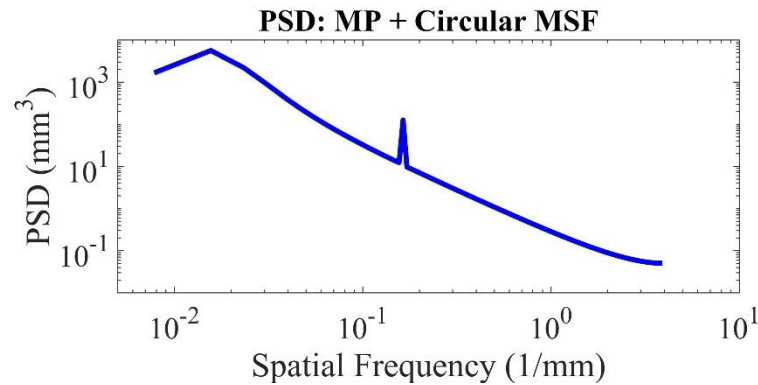


FIGURE 4.11 The power spectral density of the central horizontal profile extracted from the freeform surface with on-axis circular mid-spatial frequency errors.

The mid-spatial frequency peak observed around a spatial frequency of 0.16 cycles/mm, arises from the added MSF error. Using the Shift-Rotation technique, the freeform surface in Figure 4.10 was decomposed into four surface components: output P_{RV} , output M_{RV} , output P_{RI} , and output M_{RI} . Since the on-axis circular MSF errors consist solely of rotationally invariant terms, it is expected that these will show up convolved with the rotationally invariant components of the freeform surface. The Shift-Rotation error separations of the freeform surface with circular MSF errors are shown in Figure 4.12.

The separated RV components of the freeform surface and machine, do not reveal the presence of the circular mid-spatial frequency errors. Since the added circular mid-spatial frequency errors were on-axis and primarily comprised of RI components, the bulk of these added MSF errors are noticed in the separated RI components of the part. Some MSF residuals, however, can be noticed as convolved with the separated RI components of the machine.

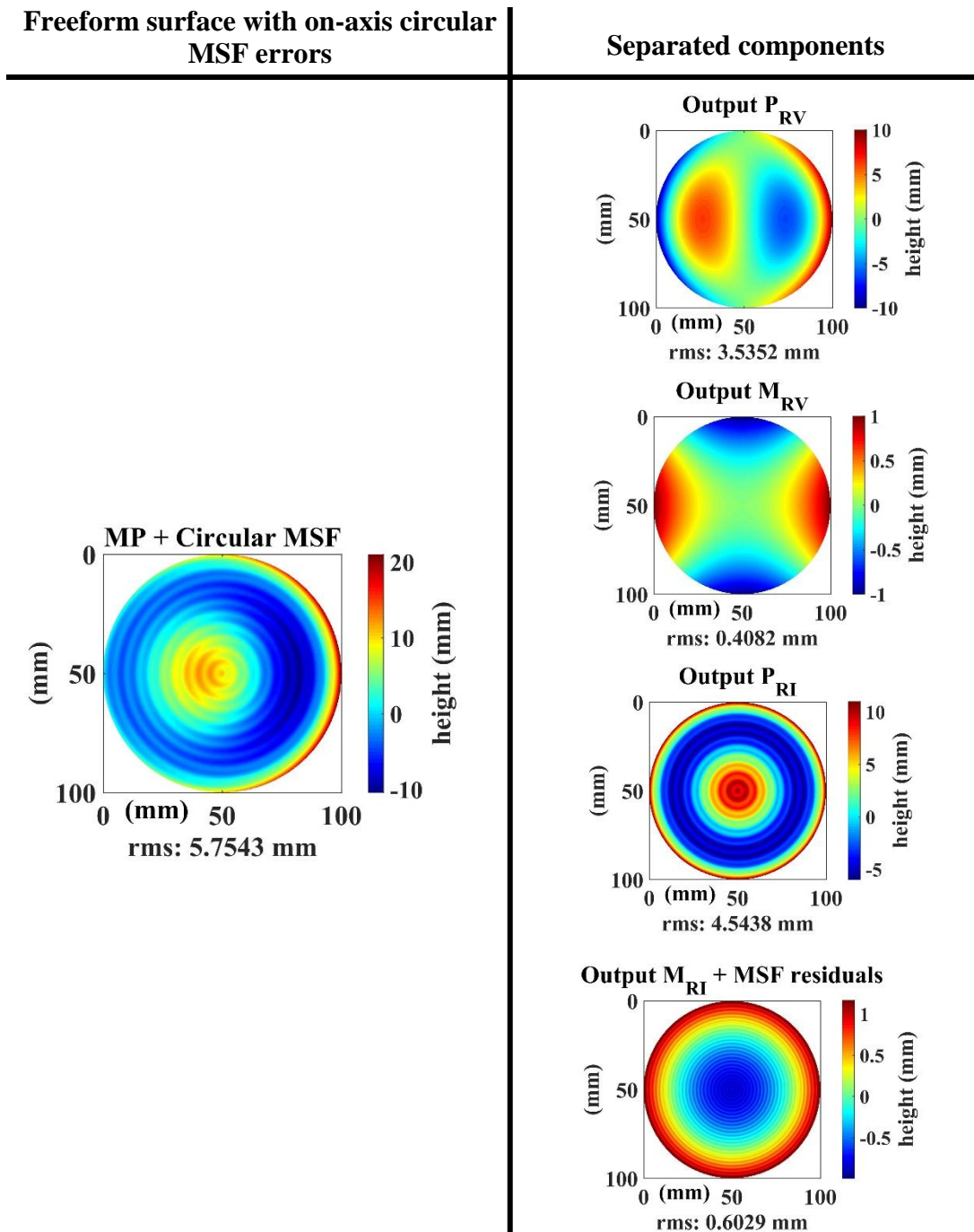


FIGURE 4.12 The simulated freeform surface with on-axis circular mid-spatial frequencies (*left*). The Shift-Rotation separation of the freeform into four components (*right*).

At this point in the error separation process, the circular MSF errors have been decomposed into an RI component (convolved with the separated RI component of the

part), and some residuals (convolved with the RI component of the machine). If these types of circular MSF errors are present on a freeform surface, after error separations of the measurement data, the bulk of the circular MSF errors would correctly be separated as convolved with the rotationally invariant components of the part. However, the residual MSF errors would be indistinguishable from the machine's RI errors. The amplitudes of these residuals can be observed after a Shift-Rotation error separation of the circular MSF errors, only.

Figure 4.13 shows the error separation of the on-axis circular MSF errors, into rotationally varying and rotationally invariant components. The MSF error components, which are not fully described as rotationally varying or invariant, are shown as the residuals. The circular MSF error contained no rotationally varying components, hence, no rotationally varying MSF error was convolved with the RV component of the part. The circular MSF error's RI component in Figure 4.13 was convolved with the RI component of the part. If the circular MSF errors were purely RI without interpolation inaccuracies, the entirety of these errors would be separated as RI components. As seen in Figure 4.13,

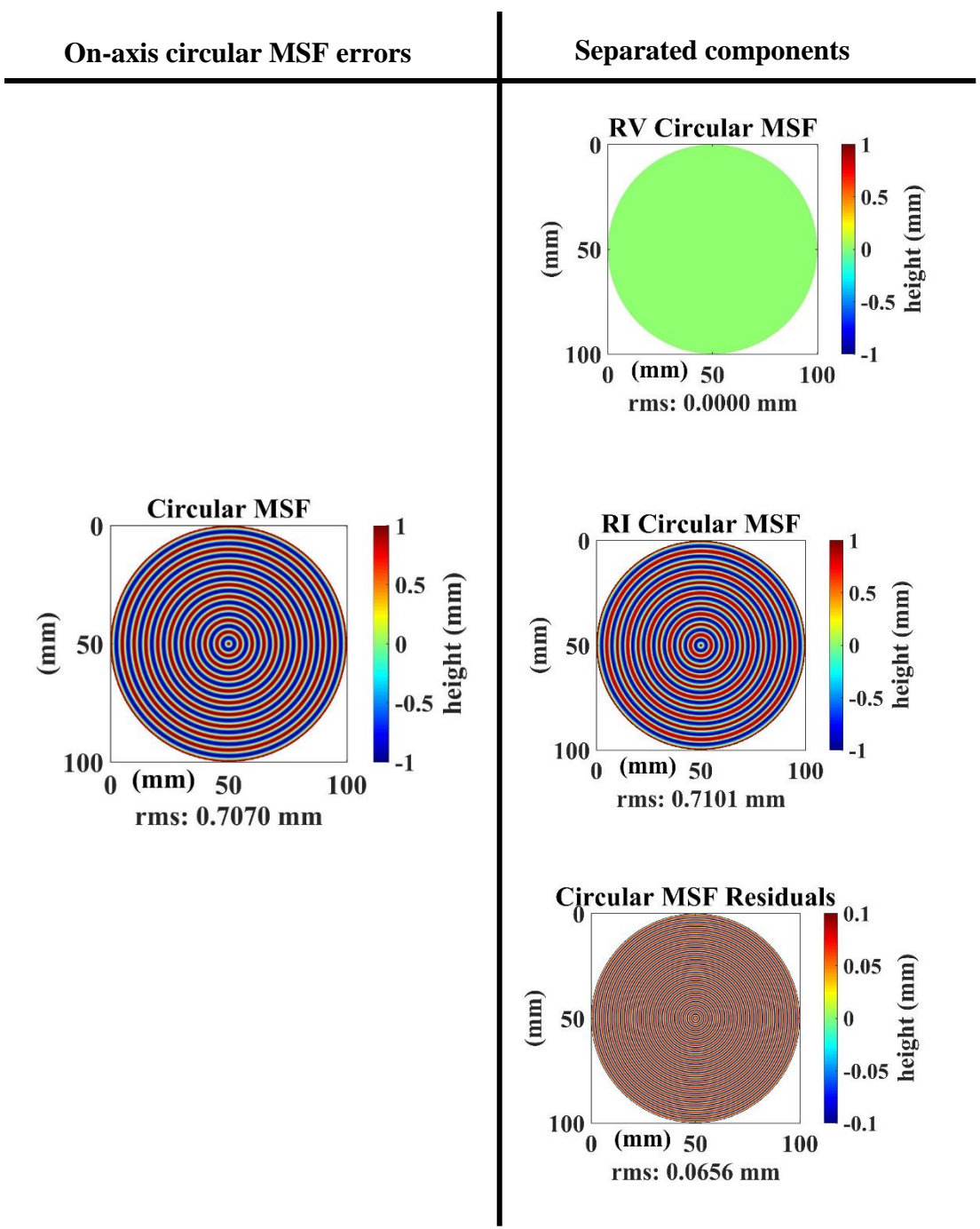


FIGURE 4.13 Simulated on-axis circular mid-spatial frequency errors (*left*). The Shift-Rotation separation of the circular mid-spatial frequency errors into rotationally varying, rotationally invariant, and residual components (*right*).

some residuals MSF errors are present. These circular MSF residuals were convolved with the RI machine errors.

On-axis circular MSF errors comprised of multiple random frequencies and amplitudes were also error separated. The results are in Appendix C. Though multiple random frequencies and amplitudes were present in the MSF errors, since these errors remained on-axis and rotationally invariant, the Shift-rotation correctly convolved them with the rotationally invariant component of the freeform surface. The next section investigates the error separation of off-axis circular MSF errors.

4.3 Error Separation of Off-Axis Circular Mid-Spatial Frequency Errors

The finishing or fabrication processes that leave spiral mid-spatial frequency errors behind, could leave off-axis errors that are not solely rotationally invariant, but contain rotationally varying terms. This section investigates the error separation of off-axis circular MSF errors using the simulated errors in Figure 4.14 (*left*). These off-axis circular MSF errors comprised multiple frequencies and amplitudes, and were added to the simulated freeform surface in Figure 4.14 (*right*).

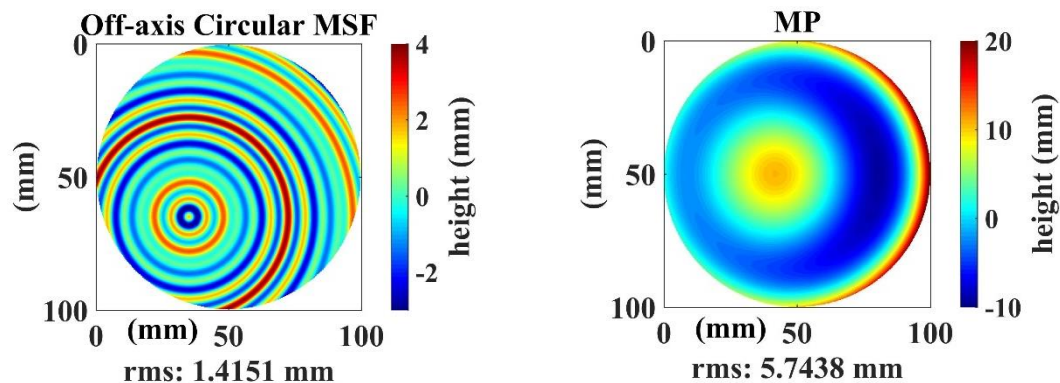


FIGURE 4.14 A simulated off-axis circular mid-spatial frequency error with multiple frequencies and amplitudes (*left*). The simulated freeform surface without mid-spatial frequency errors (*right*).

The surface that resulted from adding the off-axis MSF error to the simulated freeform surface is shown in Figure 4.15. Using the Shift-Rotation technique, this freeform surface was decomposed into four surface components: output P_{RV} , output

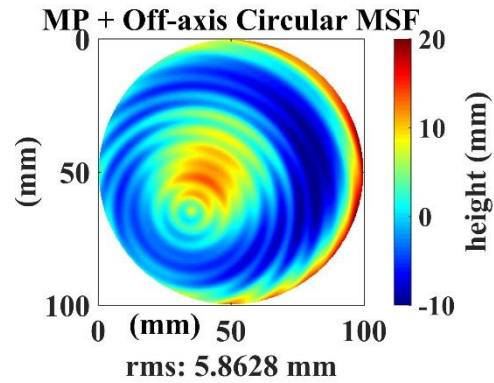
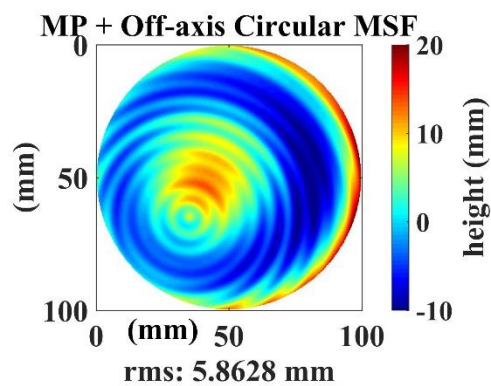


FIGURE 4.15 The simulated freeform surface with off-axis circular mid-spatial frequency errors.

M_{RV} , output P_{RI} , and output M_{RI} . Since the off-axis MSF errors contain both RV and RI terms, it is expected that these will be convolved with the RV and RI separated components of the freeform surface, respectively. The Shift-Rotation error separations of the freeform surface with off-axis MSF errors are shown in Figure 4.16.

Freeform surface with off-axis
circular MSF errors



Separated components

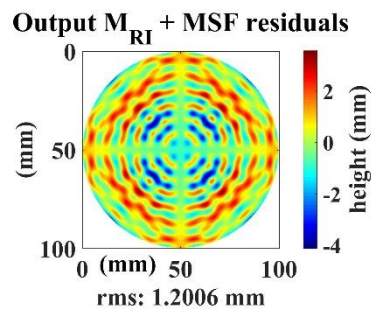
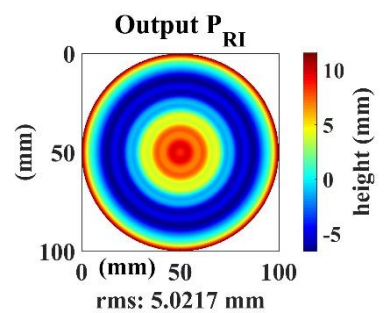
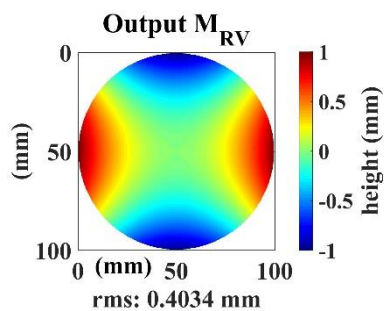
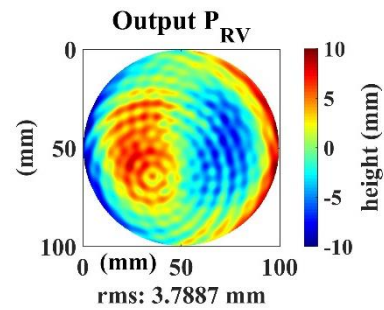


FIGURE 4.16 The freeform surface with off-axis circular mid-spatial frequencies (*left*). Shift-Rotation error separation of the freeform into four components (*right*).

Since the off-axis MSF errors contain both RV and RI components, these separated convolved with the RV and RI components of the freeform part, respectively. MSF error components that were neither RV nor RI, were residual errors and convolved with the RI machine errors. If similar off-axis circular MSF errors are present on a freeform surface, after error separations of the measurement data, these residual MSF errors would be separated as residuals indistinguishable from the machine's RI errors. The amplitudes of these residuals, as well as the RV and RI components of the off-axis MSF errors can be observed after a Shift-Rotation error separation of the MSF errors, only, as shown in Figure 4.17.

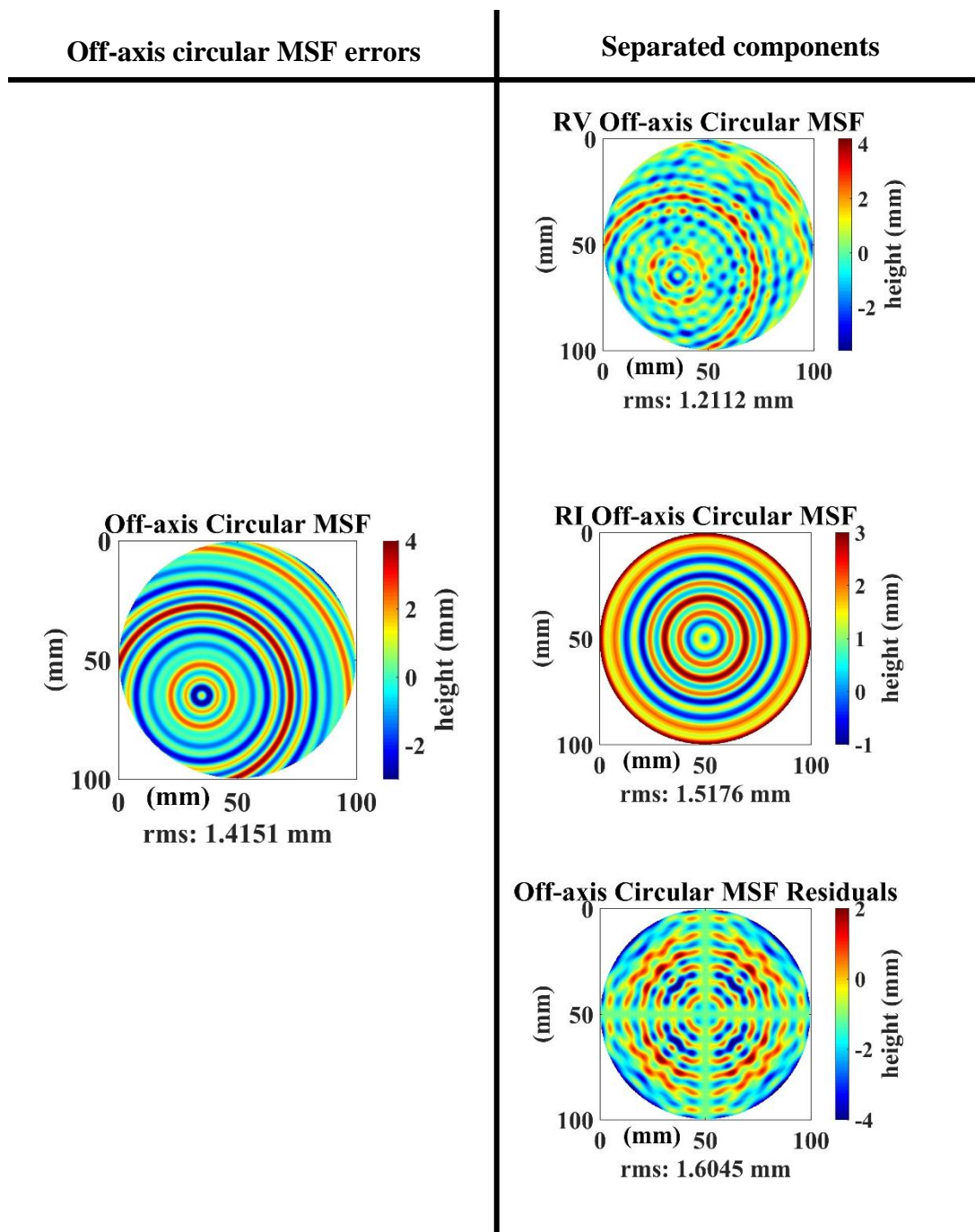


FIGURE 4.17 Off-axis circular mid-spatial frequency errors (*left*). Shift-Rotation separation of the mid-spatial frequency errors, into rotationally varying, rotationally invariant, and residual components (*right*).

4.4 Error Separation of Crosshatch Mid-Spatial Frequency Errors

Another pattern of mid-spatial frequency errors that can be left behind on a surface by some finishing processes, is a crosshatch pattern [103, 104]. Blanchard grinding is a process that could leave behind such patterns is [105], and Figure 4.18 [106] shows an example of a Blanchard ground part.



FIGURE 4.18 A Blanchard ground part showing a crosshatch pattern.

These crosshatch MSF errors comprise both RV and RI components and were Shift-rotation separated using the simulation in Figure 4.19 (*left*). These MSF errors were added to the simulated freeform surface in Figure 4.19 (*right*), and the resulting surface is shown in Figure 4.20.

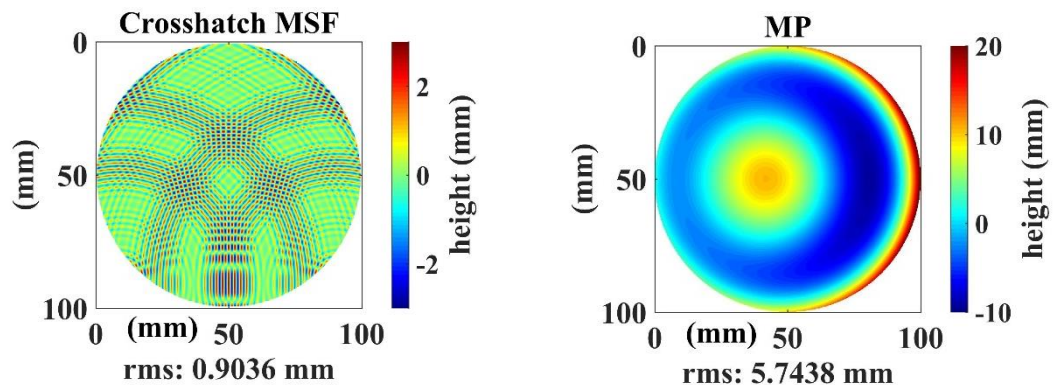


FIGURE 4.19 A simulated crosshatch mid-spatial frequency error (*left*). The simulated freeform surface without mid-spatial frequency errors (*right*).

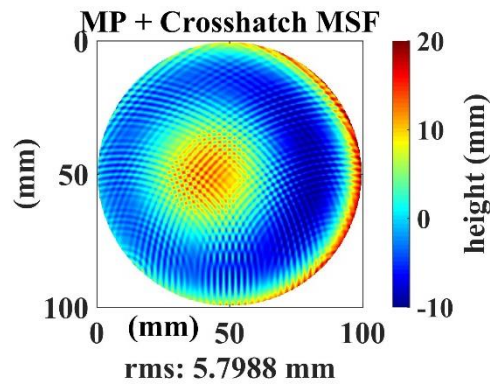


FIGURE 4.20 The simulated freeform surface with crosshatch mid-spatial frequency error.

Using the Shift-Rotation technique, this freeform surface was decomposed into four surface components: output P_{RV} , output M_{RV} , output P_{RI} , and output M_{RI} . Since the crosshatch MSF errors comprise both RV and RI terms, these are expected to be separated, convolved with the RV and RI components of the freeform part, respectively. The Shift-Rotation error separations of the freeform surface with MSF errors are shown in Figure 4.21. The error separations show that the RV components of the MSF errors were convolved with the RV components of the freeform surface, the RI components of the MSF errors were convolved with the RI components of the freeform surface, and the MSF residuals ended up convolved with the RI components of the machine errors. These components present in the crosshatch MSF errors are observed after a Shift-Rotation separation of only the crosshatch errors, and shown in Figure 4.22.

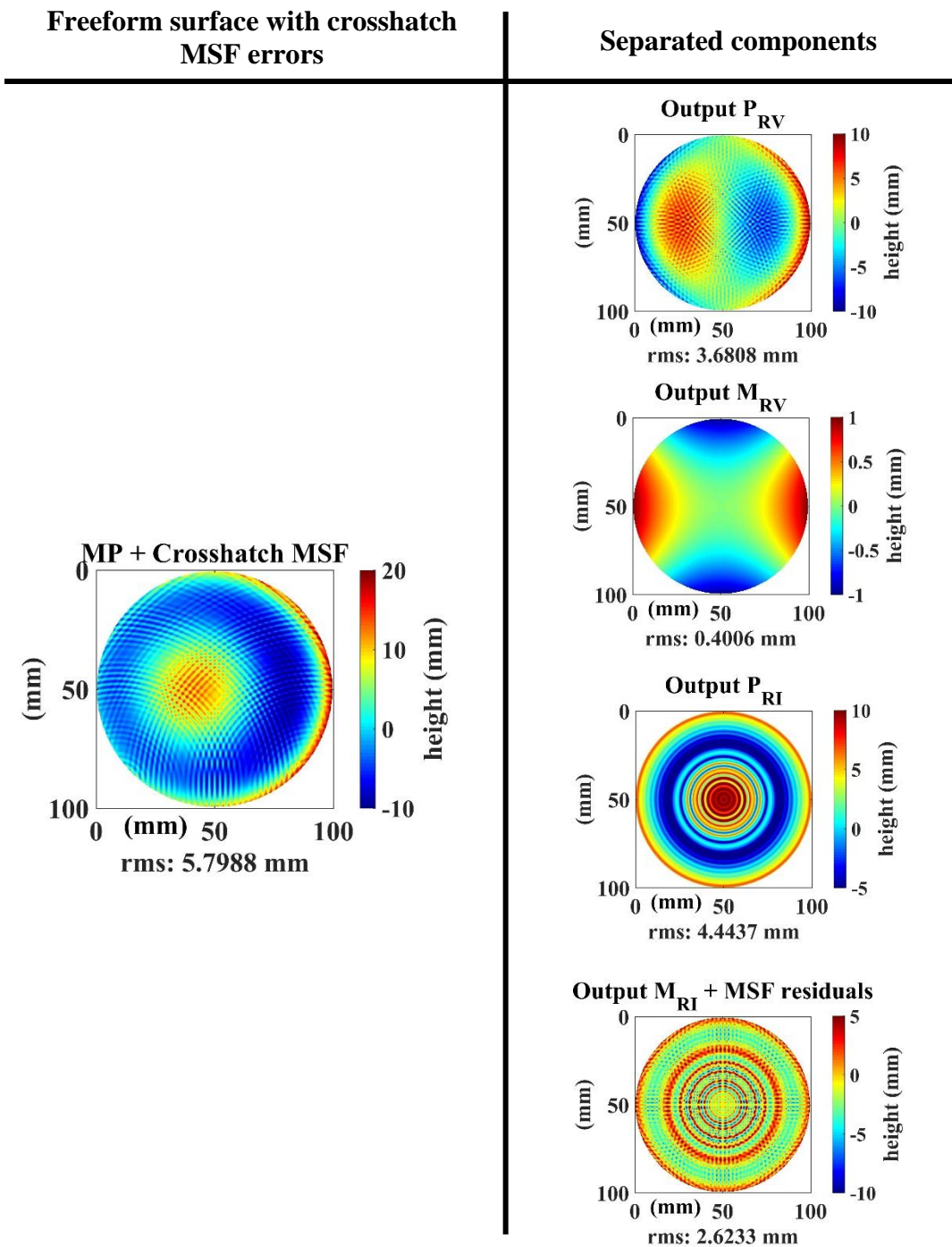


FIGURE 4.21 The simulated freeform surface with crosshatch mid-spatial frequencies (*left*). The Shift-Rotation error separation of the freeform into four components (*right*).

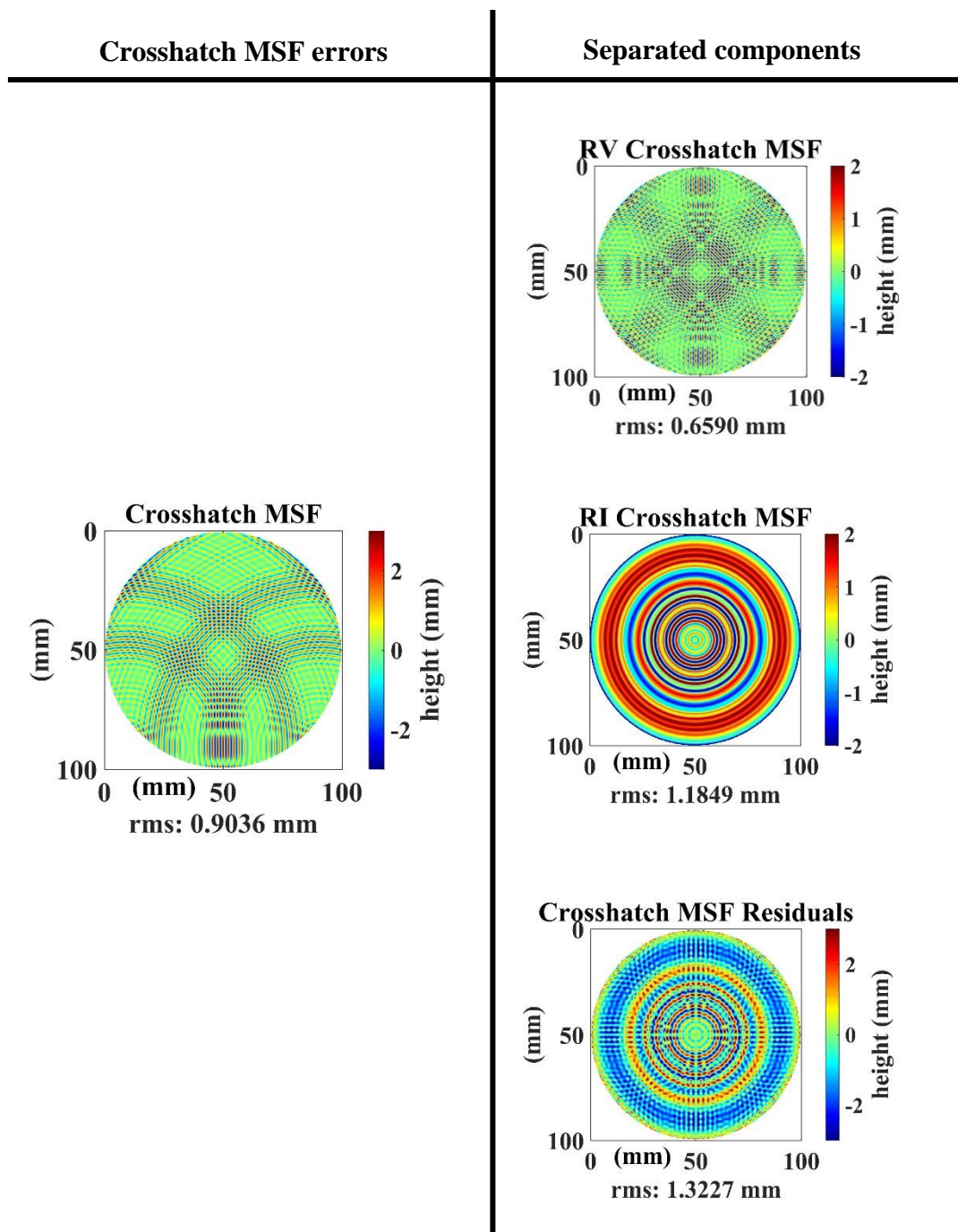


FIGURE 4.22 Crosshatch mid-spatial frequency errors (*left*). Shift-Rotation separation of the mid-spatial frequency errors, into rotationally varying, rotationally invariant, and residual components (*right*).

4.5 Summary

The Shift-Rotation technique is a form metrology suited to separating low-spatial frequency surface components, but this chapter used simulations to explore its error separation of some mid-spatial frequency (MSF) patterns that could be left behind by finishing processes. The MSF patterns in this chapter were chosen to represent the effect, not the likely amplitude in state of the art freeform surfaces.

The Shift-Rotation process separated the MSF errors into rotationally varying (RV), rotationally invariant (RI) components, and residuals. The amplitudes of these residuals can be decreased by increasing the number of rotational positions. These residuals were convolved with the RI components of the machine errors and further information would be required to deconvolve the errors.

CHAPTER 5: FREEFORM SURFACE MEASUREMENTS

So far, the demonstrations of the Shift-Rotation error separation technique have been carried with simulations. The measurement steps and procedures explained in Chapter 2, and the flowchart in Appendix A, were applied to experimental freeform surface measurements. The Shift-Rotation error separation was demonstrated by measuring a freeform surface on two touch-probe machines: a Zeiss F-25 CMM and a Mahr LD 260 surface profiler. From these measurement results, rotationally varying and invariant freeform surface components (and machine error contributions) were separated, to obtain best-estimate freeform measurements without machine error contributions. These best-estimates from the tactile machines were compared to optical measurements of the same freeform surface.

Since the error separation technique required predefined rotations and translation(s) of the test part, the measurement stage on which the part was measured had rotation and translation capabilities. In Chapter 3.2, Monte Carlo simulations were used to estimate uncertainty contributions from a moving axis of rotation. Ideally, these predefined rotations of the part should be about a fixed axis of rotation. This rotation axis should be constrained against translations in the plane perpendicular to the axis of rotation. One step towards achieving this goal involved positioning the freeform part on a linear-rotary stage, such that the optical axis of the part remained aligned to the rotation axis of the rotary stage.

Since the linear stage was to be used in the alignment process, a two-axis stage was appropriate. This x-y stage was mounted on the rotary stage (not the rotary stage on the x-y stage) because this configuration allowed for translations of the optical axis of the part, relative to that of the rotary stage. If the x-y stage was underneath the rotary stage, linear translations would move the rotation axes of the rotary stage and the part concurrently, and that would not improve the alignment of the rotary axes.

5.1 The Freeform Surface to be Measured

The freeform surface that was measured in this project was fabricated on a BK7 optical flat, on a magnetorheological finishing (MRF) machine [107]. It was housed in a polycarbonate mount with four silicon carbide balls and a reference mark that transfer coordinates from MRF to metrology. The freeform part had an outer diameter of 40-mm and a clear aperture of about 35-mm and is shown in Figure 5.1.

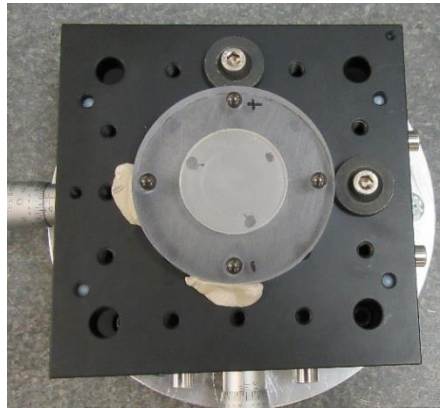


FIGURE 5.1 The freeform surface to be measured.

This freeform surface was measured on a Zeiss F-25 CMM and a Mahr LD 260 surface profiler and the task-specific measurement uncertainties were minimized by applying the Shift-Rotation error separation technique. In addition to these measurements, the freeform surface was also measured on two optical measuring machines and

comparisons were made between the measurement results. The next section introduces the measuring machines used.

5.1.1 Four Different Machines to Measure the Freeform Surface

The freeform surface shown in Figure 5.1 was measured on the following four measuring machines: a Zeiss F-25 micro-CMM, a Mahr MarSurf LD 260 surface profiler, a Zygo Verifire Fizeau interferometer, and a Zygo NexView Scanning White Light interferometer. The F-25 CMM is a touch-probe based machine (also with optical capabilities) with a 100-mm x 100 mm x 100 mm measuring volume. The touch-probe CMM has a maximum permissible error, MPE: $(0.25 + L/666) \mu\text{m}$ ($L =$ measuring length in mm) [108]. The MarSurf LD 260 surface profiler is also a touch-probe based machine; it has a measuring length up to 260 mm, a vertical resolution of 0.8 nm and form deviations of less than 100 nm [109]. The Shift-Rotation error separation was applied to the measurement results from these tactile machines, but the interferometric measurement results were not error separated. These measuring machines are shown in Figure 5.2.

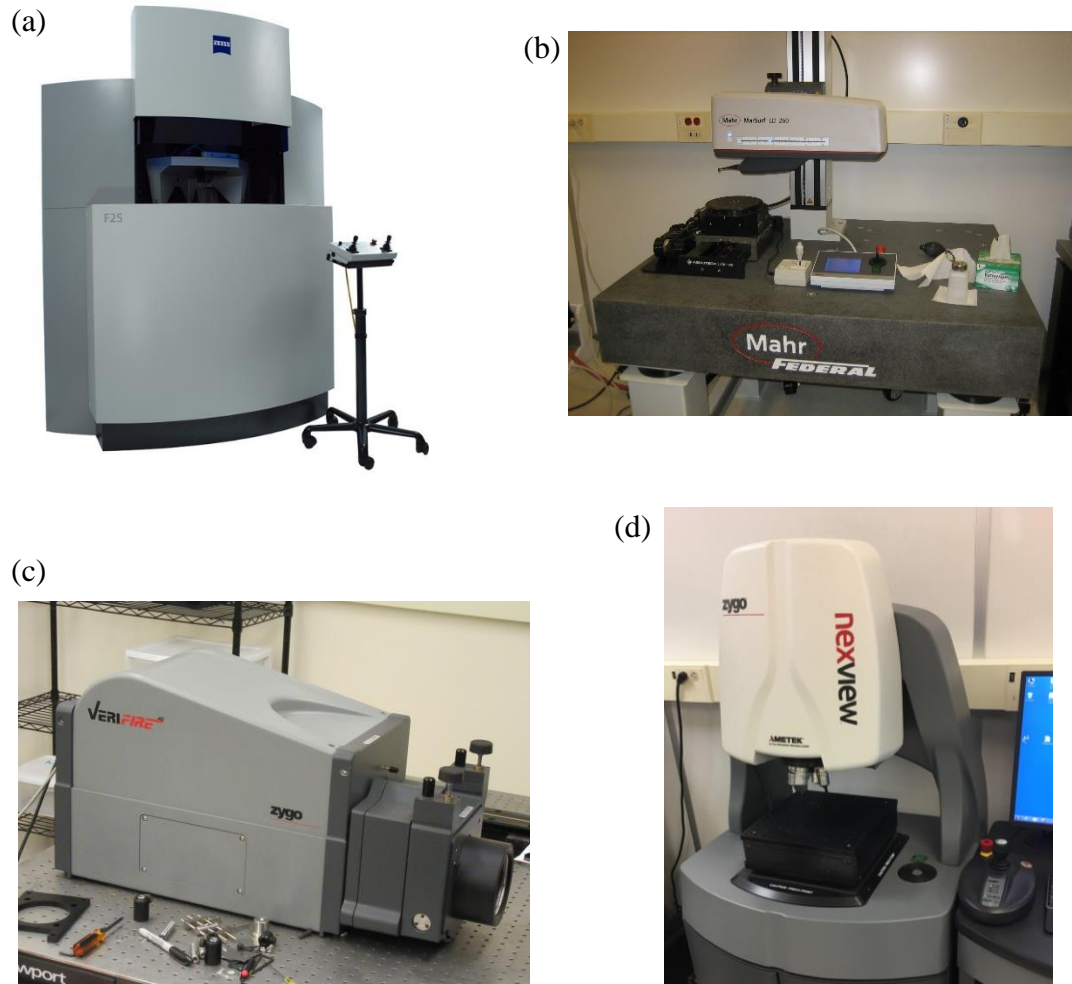


FIGURE 5.2 Four machines to measure the freeform surface. (a) Zeiss F-25 micro Coordinate Measuring Machine (b) Mahr MarSurf LD 260 surface profiler (c) Zygo VeriFire Fizeau Interferometer (d) Zygo NexView Scanning White Light Interferometer.

5.2 Measurement of the Freeform Surface on the Zygo Fizeau Interferometer

The freeform surface was fabricated with slopes slow enough to be measurable on the Fizeau interferometer using a transmission flat. The Fizeau measurement of the freeform surface was of the entire 40-mm diameter and included an annulus around the clear aperture. This measurement result was cropped down to the 35-mm clear aperture and fit to twelve Zernike terms. Figure 5.3 shows the surface generated from these twelve Zernike terms while Table 5.1 shows the Zernike coefficients.

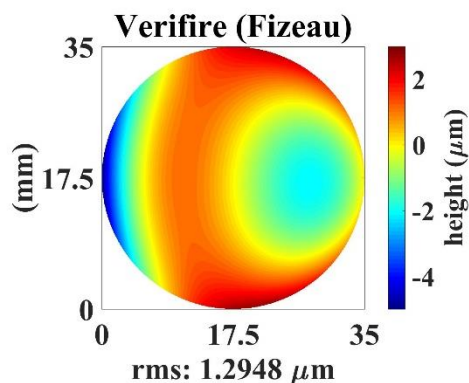


FIGURE 5.3 A Fizeau measurement of the freeform surface.

TABLE 5.1 Zernike coefficients from the Fizeau measurement of the freeform surface.

	Zernike coefficients (nm)											
	Z (2, 0)	Z (2, -2)	Z (2, 2)	Z (3, -1)	Z (3, 1)	Z (3, -3)	Z (3, 3)	Z (4, -4)	Z (4, -2)	Z (4, 0)	Z (4, 2)	Z (4, 4)
Fizeau	-22	-129	-2390	-125	-2392	109	-151	15	67	-27	-54	6

The Zeiss F-25 CMM was the next measuring machine used to measure the freeform surface. The Shift-Rotation error separation was applied to these measurement results and the next section describes the measurement strategy used, measurement results and error separations.

5.3 Measurements of the Freeform Surface on the Zeiss F-25 CMM

A Cartesian measurement model was used to measure the freeform on the Zeiss F-25 CMM. Thirty-seven parallel profiles were scanned across the freeform surface; Figure 5.4 depicts this measurement strategy. Beginning with the first vertical profile on the left-hand side, a 12.17-mm-long profile was scanned. After translating the part 1 mm to the left, a second profile, 16.97-mm-long was measured. Successive profiles were also measured with 1-mm-long separations in-between until thirty-seven profiles were

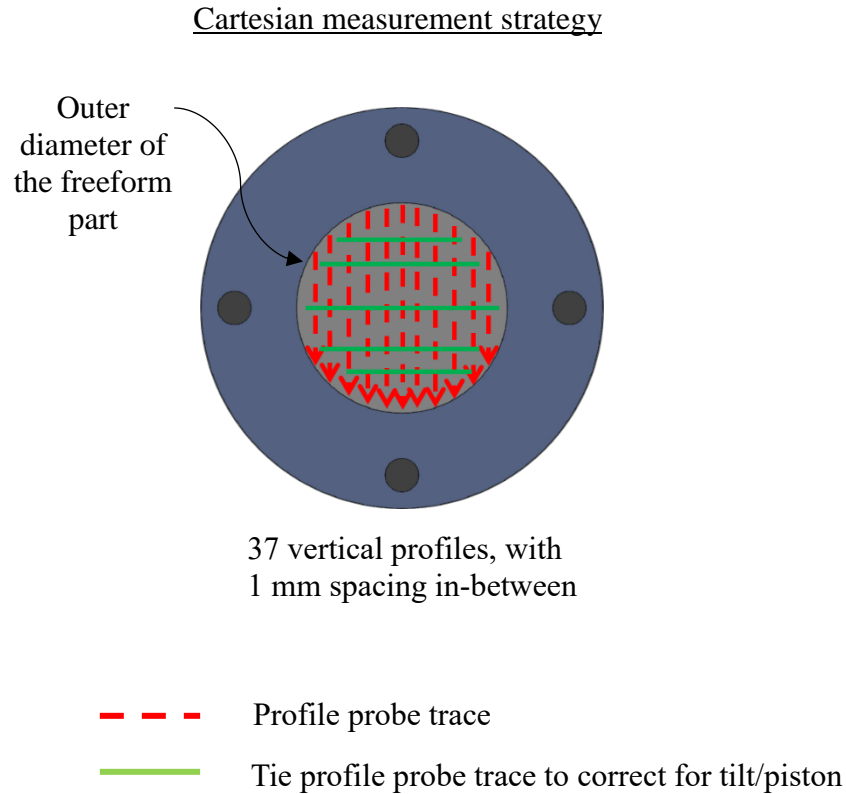


FIGURE 5.4 Cartesian measurement strategy employed on the Zeiss F-25 CMM.

measured across the surface of the 40-mm diameter part. The longest profile was the 19th profile, and was 38 mm-long while the shortest profiles were the 1st and 37th with lengths of 12.17 mm. Each of the scanned profiles had data densities with point coordinates every 1 μm .

Between the first and thirty-seventh profile measurements, stage drifts and tilt changes could occur. To correct for the possible changes in tilt and piston, additional profiles were measured. These were five parallel tie-profiles measured perpendicular to the thirty-seven profiles. The third of the five tie-profiles was 38-mm-long and ran across the middle of the part. The second and fourth tie-profiles were 36 mm-long and were measured 6 mm above and below the middle tie-profile, respectively. The first and fifth tie-profiles were 33 mm-long and were measured 9.5 mm above and below the middle tie-profile,

respectively. From the expected intersection points between the five tie-profiles and the thirty-seven profiles, the tilt and piston of each of the thirty-seven profiles were corrected.

Since the Shift-Rotation error separation technique requires multiple measurements of the freeform surface at predefined angular orientations and translations of the part, the above measurement strategy was repeated during the measurements at every orientation of the part. Figure 5.5 shows the first set of profiles scanned across the freeform surface, with the part in an initial orientation. These are pre-processed profiles and the figure includes the five tie-profiles that will be used to correct the tilts and piston of the thirty-seven profiles.

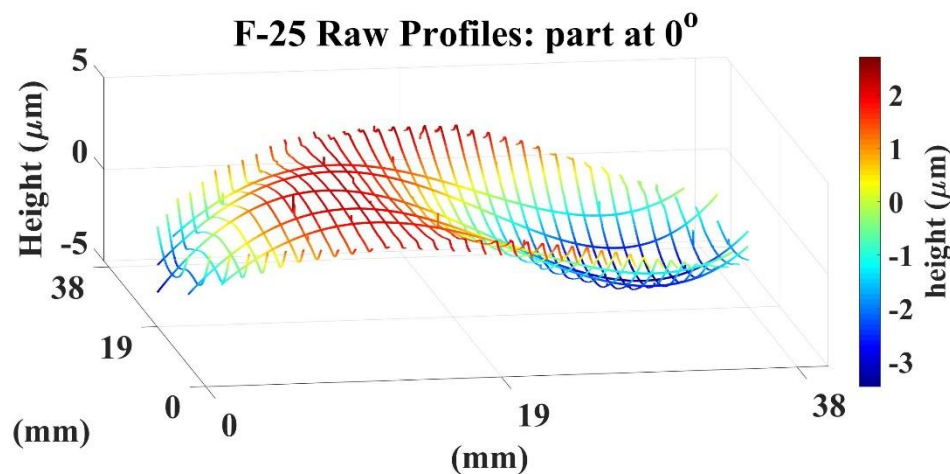


FIGURE 5.5 Profiles scanned across the freeform surface, measured on the F-25 CMM with the part in an initial position/orientation.

Since the Shift-Rotation technique is a form metrology, the roughness of the profiles was removed by applying a low-pass Gaussian filter, in the spatial domain, to all the profiles. Equation 5.1 shows the weighting function of this filter, where $\alpha = \sqrt{\ln 2/\pi} = 0.4697$, x is the position from the origin of the weighting function and a long-wavelength roughness cutoff, λ_c , of 0.8 mm was used [99].

$$S(x) = \frac{1}{\alpha\lambda_c} \exp \left[-\pi \left(\frac{x}{\alpha\lambda_c} \right)^2 \right] \quad (5.1)$$

The next data processing was a crop-down to the clear aperture. The profiles scanned on the freeform surface spanned a 38-mm diameter; these were cropped down to the 35-mm clear aperture. Next, the tilts and pistons of the thirty-seven profiles were corrected by using the x - y intersection points between the tie-profiles and the thirty-seven profiles. The tilt- and piston-corrections entailed making the thirty-seven profiles pass through the tie-profiles with minimum z -axis residuals at the x - y intersections. This was done by matching the slopes and pistons of the thirty-seven profiles, to those of the tie-profiles, at the respective intersection points. The low-pass filtered, cropped, and slope-corrected profiles from the first set of F-25 CMM measurements is shown in Figure 5.6.

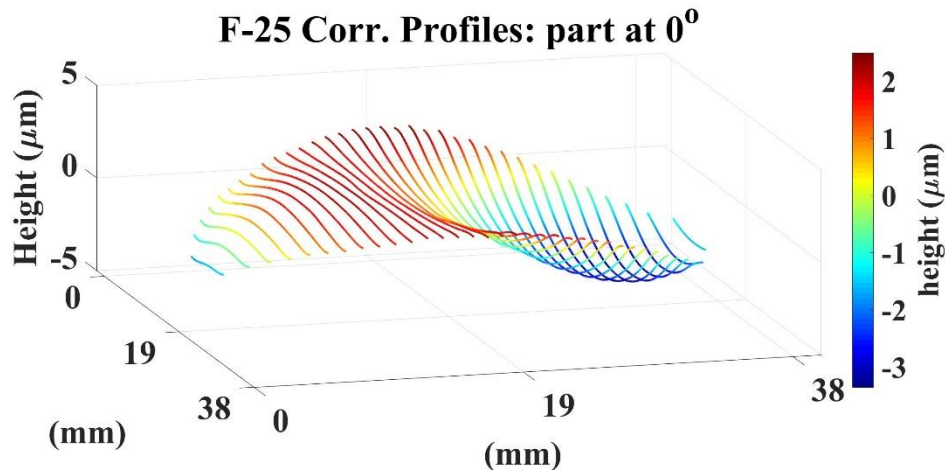


FIGURE 5.6 Low-pass filtered, cropped, and slope-corrected profiles from the first set of F-25 CMM measurements.

Next, twelve Zernike terms were fit to the surface data in Figure 5.6. The Zernike coefficients from this fit are listed in Table 5.2, while the surface generated from these coefficients is shown in Figure 5.7.

TABLE 5.5 Zernike coefficients of the Zernike fit to the corrected profiles (F-25 freeform measurement of the part in the initial position/orientation).

	Zernike coefficients (nm)											
	Z (2, 0)	Z (2, -2)	Z (2, 2)	Z (3, -1)	Z (3, 1)	Z (3, -3)	Z (3, 3)	Z (4, -4)	Z (4, -2)	Z (4, 0)	Z (4, 2)	Z (4, 4)
F-25 (part at 0°)	-45	146	-2272	23	2173	-165	-5	39	66	34	238	153

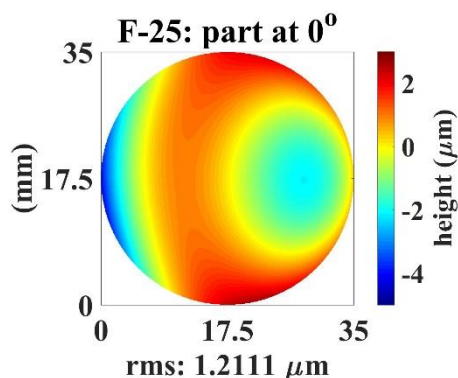


FIGURE 5.7 F-25 CMM freeform measurement of the part in the initial position.

5.3.1 Error Separations of the Rotationally Varying Components

The surface in Figure 5.7 represents the first measurement of the freeform surface on the Zeiss F-25 CMM. To solve for the rotationally varying (RV) components of the freeform, additional measurements of the part at predefined angular orientations were made. The number of angular orientations of the part was chosen to be five because there was a priori knowledge of the angular orders expected to be of significant amplitude on the freeform. Zernike terms with angular orders of 2θ were expected to dominate the freeform, hence, a minimum of three measurements of the part at equally-separated angular orientations would adequately solve for the RV components of the part.

The Cartesian measurement model described in Chapter 5.3 was used to measure the freeform surface at each angular orientation. These measured profiles were also low-pass Gaussian filtered, clear-aperture cropped, slope-corrected and fit to twelve Zernike terms. The five surfaces generated from the F-25 measurements of the freeform, at the five angular orientations of the part separated by 72° , are shown in Figure 5.8, while their corresponding Zernike coefficients are shown in Table 5.3.

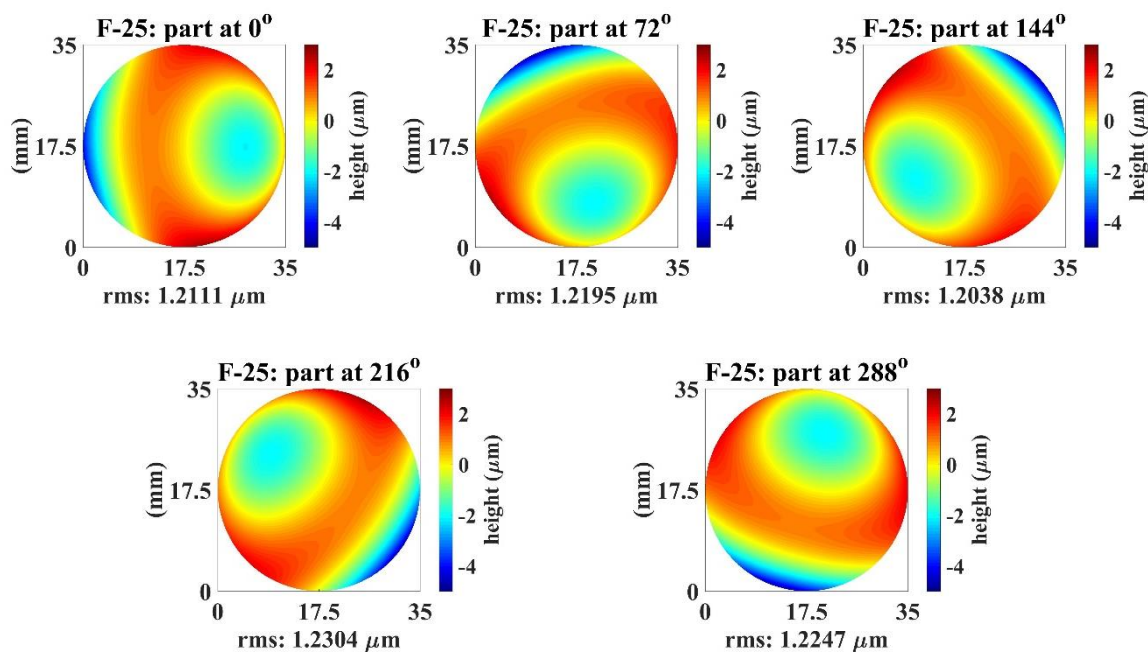


FIGURE 5.8 F-25 CMM freeform measurements of the part at five angular orientations.

TABLE 5.9 Zernike coefficients from the F-25 freeform surface measurements of the part in five angular orientations.

	Zernike coefficients (nm)											
	Z (2, 0)	Z (2, -2)	Z (2, 2)	Z (3, -1)	Z (3, 1)	Z (3, -3)	Z (3, 3)	Z (4, -4)	Z (4, -2)	Z (4, 0)	Z (4, 2)	Z (4, 4)
F-25 (part at 0°)	-45	146	-2272	23	2173	-165	-5	39	66	34	238	153
F-25 (part at 72°)	-8	-1522	1643	2166	658	71	-223	98	33	-64	-143	-43
F-25 (part at 144°)	32	2152	-522	1284	-1799	110	332	-156	-108	-21	128	35
F-25 (part at 216°)	-10	-2164	-802	-1386	-1730	-241	27	134	155	8	11	39
F-25 (part at 288°)	-53	1260	1876	-2148	709	125	-106	-81	-136	-35	-123	-99

The freeform part was measured at multiple angular orientations to enable separation of the RV component of the part by using the N-Rotation technique described in Chapter 2.1. Equations 2.1 – 2.7 expressed the error separations in Chapter 2; these equations were repeated in this Chapter to express the error separation of the F-25 measurement results. An F-25 measurement of the freeform surface was expressed as shown in Equation 5.2, where P_{RV} represents the rotationally varying component of the freeform surface, P_{RI} represents the rotationally invariant component of the freeform, M_{RV} represents the rotationally varying component of the machine error contributions, and M_{RI} represents the rotationally invariant component of the machine error contributions.

$$F25_{meas} = P_{RV} + P_{RI} + M_{RV} + M_{RI} \quad (5.2)$$

The average of the five maps in Figure 5.8 cancelled out the RV component of the part; this average was denoted by $Mean_{P(rot)}$, is expressed in Equation 5.3 and shown Figure 5.9.

$$Mean_{P(rot)} = P_{RI} + M_{RV} + M_{RI} \quad (5.3)$$

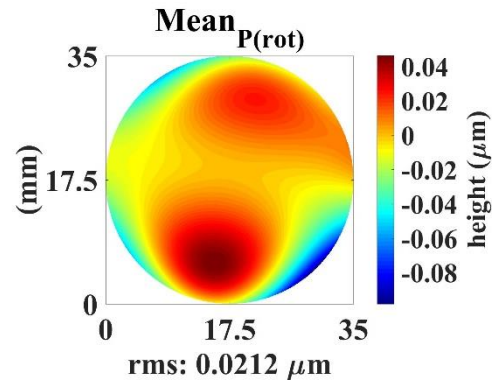


FIGURE 5.9 An average of the F-25 measurements of the freeform surface at the five angular orientations.

The RV component of the part, dropped out by the averaging process, was obtained by subtracting the map in Figure 5.9 from that in Figure 5.7; and the resulting map is shown in Figure 5.10.

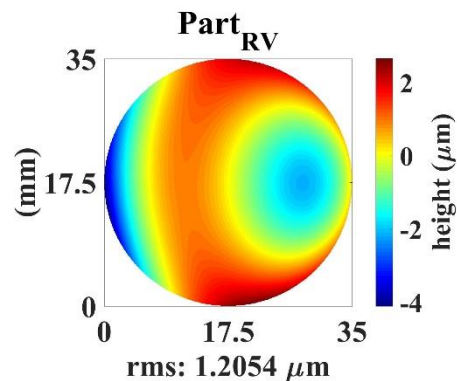


FIGURE 5.10 The separated rotationally varying component of the freeform surface.

The height map in Figure 5.10 represents the first of the four desired separated components of the F-25 freeform surface measurement. The next surface component to be extracted is the RV component of the machine's errors. Since the RV components of the test part have been extracted, any residual RV components must come from the machine error contributions. This RV machine error component was obtained by applying the N-Rotation technique to the height map in Figure 5.9 (Alternatively, the RV component of the machine can be obtained by rotating the maps in Figure 5.8 to the same orientation, and averaging). The rotations of the height map are shown in Figure 5.11.

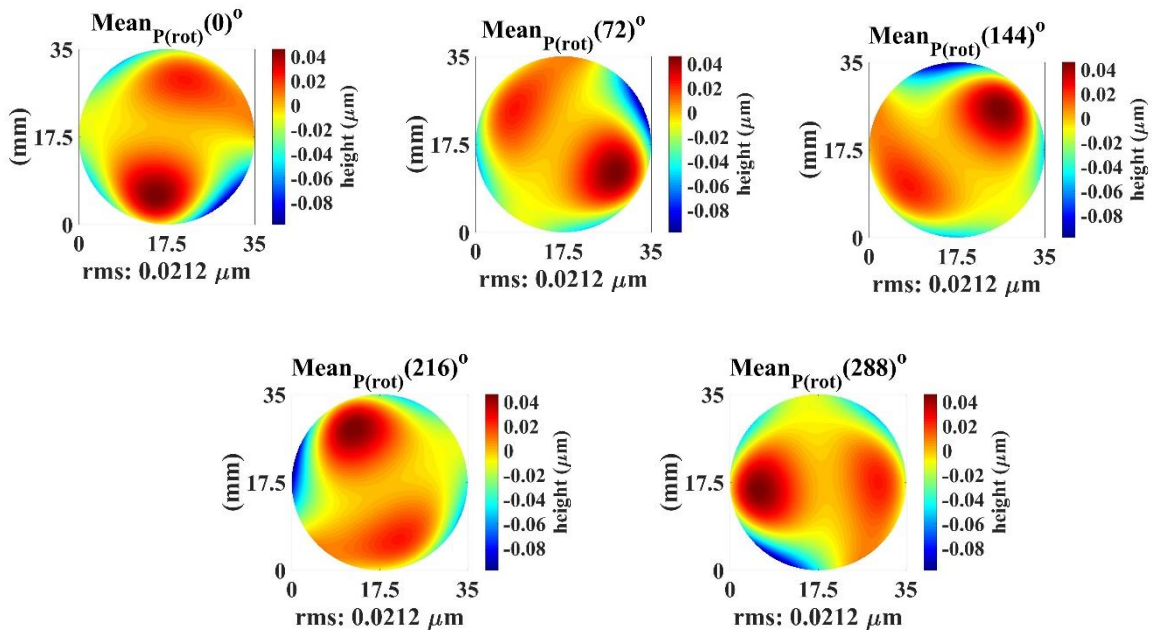


FIGURE 5.11 N-Rotations to extract the machine's rotationally varying error contributions.

The RV components of the machine errors rotate with each rotation in Figure 5.11. The average of these maps dropped out the RV machine error components and was expressed as Equation 5.4 and shown in Figure 5.12.

$$Mean_{M(rot)} = M_{RI} + P_{RI} \quad (5.4)$$

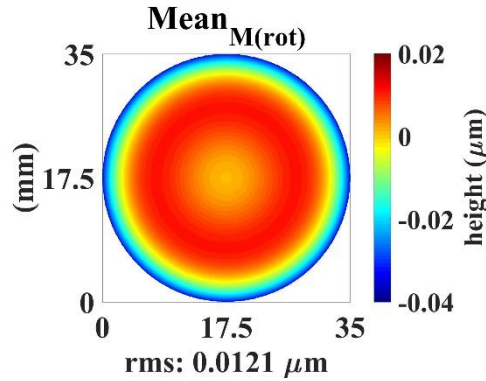


FIGURE 5.12 Average of the height maps that depict machine rotations. This average drops out the rotationally varying components of the machine errors.

The RV machine error component dropped out by the averaging process was obtained by subtracting Equation 5.4 from Equation 5.3; the resulting map is shown in Figure 5.13.

$$M_{RV} = Mean_{P(rot)} - Mean_{M(rot)} \quad (5.5)$$

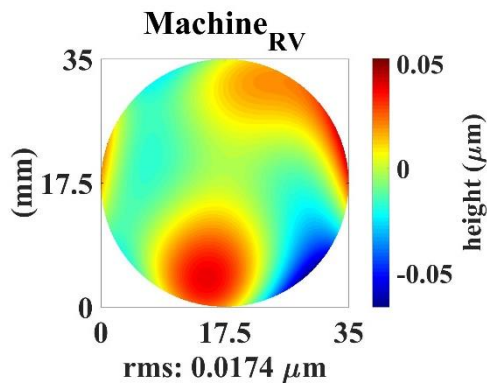


FIGURE 5.13 The separated rotationally varying component of the machine's errors.

This height map in Figure 5.13 represents the second of the four desired separated components. So far, the RV components of the part and machine error contributions have been separated, and the height map in Figure 5.12 contains only RI components of the test part and the machine's errors. These RI components were obtained from the 'Shift' portion of the Shift-Rotation technique.

5.3.2 Error Separations of the Rotationally Invariant Components

The Shift-technique described in Chapter 2.2 was used to separate the RI components present in Figure 5.12. This error separation requires an additional measurement of the freeform surface, after a lateral translation with respect to an initial position. With respect to the initial position of the part, as shown in Figure 5.7, the part was translated 1-mm and measured on the F-25 CMM. The surfaces generated from Zernike fits to the profiles from both measurements are shown in Figure 5.14.

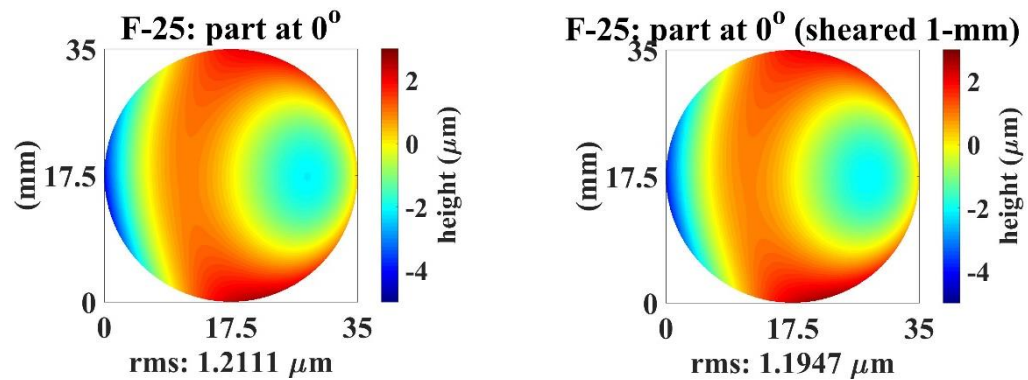


FIGURE 5.14 Measurement of the freeform surface in an initial position (*left*). Measurement after the part was shifted upwards by 1 mm (*right*).

If the measurement of the freeform in the initial position is expressed as shown in Equation 5.6, where the superscripts, ‘0’, indicate an initial position, then, the measurement after a lateral shift of the part can be expressed as shown in Equation 5.7. The superscripts, Δ , indicate the translated components.

$$F25_{meas}^0 = P^0_{RV} + P^0_{RI} + M^0_{RV} + M^0_{RI} \quad (5.6)$$

$$F25_{meas}^{\Delta} = P^{\Delta}_{RV} + P^{\Delta}_{RI} + M^0_{RV} + M^0_{RI} \quad (5.7)$$

Equations 5.6 and 5.7 assume the machine errors remained constant between the initial- and translated-part measurements. Based on this assumption, and after removing the RV components, a difference between Equations 5.6 and 5.7 gave the slope of the

freeform surface evaluated at the separation and in the translation direction, as shown in Figure 5.15.

The goal of the following steps was to obtain the RI component of the test part,

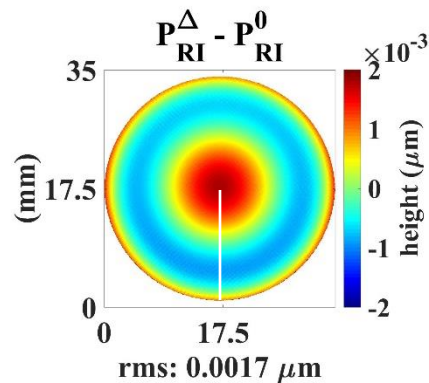


FIGURE 5.15 The slope of the freeform part evaluated after a 1-mm lateral translation.

from the slope height map in Figure 5.15. A profile, \mathbf{g} , was extracted from the part center to the edge in the $-\Delta$ direction (indicated by the white vertical line in Figure 5.15). Each point in \mathbf{g} was a height difference between two points (a distance 1-mm apart) in the desired radial profile, \mathbf{f} . The relationship between profiles \mathbf{f} and \mathbf{g} was expressed as a system of linear equations: $\mathbf{g} = \mathbf{H} * \mathbf{f}$, where \mathbf{g} was an $m \times 1$ column vector, \mathbf{f} was an $n \times 1$ column vector, and \mathbf{H} was an $m \times n$ design matrix that was built based on the size of the freeform part and the translation distance [66].

This design matrix \mathbf{H} , and an alternative way around its singularity, were described using simulations in Chapters 2.2 and 2.2.1. The simulations showed the alternative approach (noise-modification of the singular matrix) yielded the same or more accurate solutions than the pseudo-inverse approach but the above experimental validations showed otherwise. The RI solutions obtained from the noise-modification of the singular matrix did not show RI details expected to be on the test surface. Therefore, the pseudo-inverse

approach was used to decompose the RI components from the experimental results. Further research is needed to determine more robust ways of noise-modifying the singular matrix.

From the linear equation: $\mathbf{g} = \mathbf{H} * \mathbf{f}$, the desired radial profile was solved using the pseudo-inverse of \mathbf{H} and is shown in Figure 5.16.

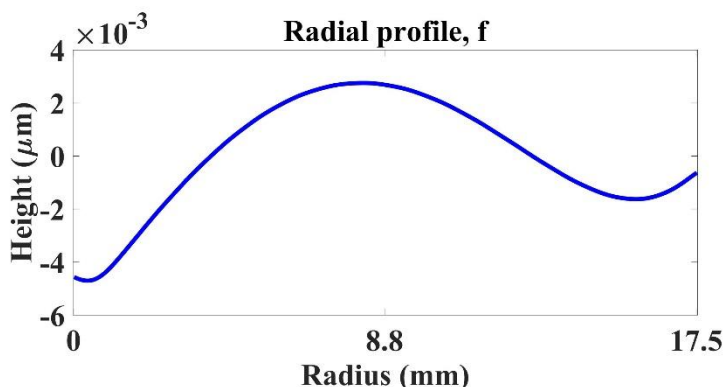


FIGURE 5.16 The solved radial profile of the rotationally invariant component of the freeform surface.

The rotationally invariant component of the freeform surface was then generated from the radial profile in Figure 5.16. The final separated component, the RI component of the machine errors, was obtained by subtracting the separated RV components of the part and machine, and the RI part-component from the measurement of the part in its initial 0° orientation. These separated RI components are shown in Figure 5.17.

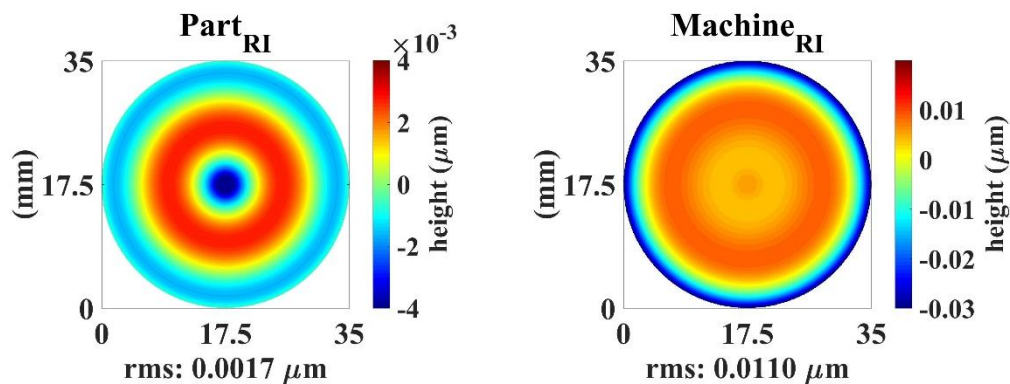


FIGURE 5.17 The solved rotationally invariant component of the freeform surface (*left*). The solved rotationally invariant component of the machine error contributions (*right*).

5.3.3 Best Estimate of the Freeform Surface from the Zeiss F-25

The error separations of the F-25 freeform measurements led to a best estimate of the freeform surface, without machine error contributions. This estimate was obtained by summing the two separated components of the freeform surface. These separated components, shown in Figure 5.10 and Figure 5.17 (*left*), were added to give the best estimate of the freeform in Figure 5.18. The Zernike coefficients from a twelve-Zernike polynomial fit to this best estimate freeform are listed in Table 5.4.

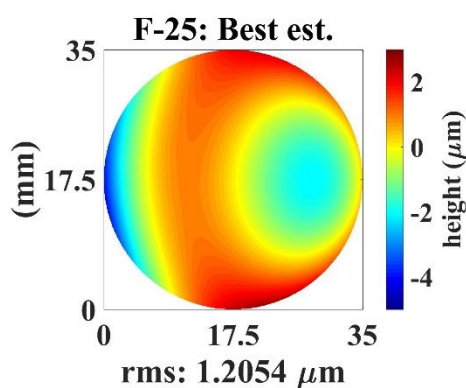


FIGURE 5.18 Best estimate of the freeform surface, separated from the Zeiss F-25 measurement results.

TABLE 5.13 Zernike coefficients from a Zernike polynomial fit to the best estimate of the freeform surface.

	Zernike coefficients (nm)											
	Z (2, 0)	Z (2, -2)	Z (2, 2)	Z (3, -1)	Z (3, 1)	Z (3, -3)	Z (3, 3)	Z (4, -4)	Z (4, -2)	Z (4, 0)	Z (4, 2)	Z (4, 4)
F-25: best est.	-30	172	-2257	36	2171	-145	-10	32	64	49	216	136

5.3.4 Uncertainty Estimations in the Best Estimate from the CMM

The Monte Carlo simulations described in Chapter 3 were used to evaluate task-specific uncertainties associated with the freeform best estimate shown in Figure 5.18. The uncertainty sources used as inputs to the Monte Carlo simulation were the rotation angles, the axis of rotation, the translation distance, and electronic noise.

The standard uncertainty, because of an uncertainty in the rotation angle, was represented as $u_{RotAngle}$. This was evaluated using a flowchart like Figure 3.2, and had five rotation-angles separated by 72° as its input. This was because five angular orientations of the part were used to solve the RV components in the F-25 measurements. In using the Monte Carlo, instead of assuming these five angles were perfect rotation angles, we presumed that each rotation angle fell anywhere within some distribution. Uniform distributions with upper and lower limits of $\pm 0.05^\circ$ were used around each nominal rotation angle. After running the Monte Carlo loop 1000 times, such that each trial had random angles from the input distributions, an array of possible outcomes of the freeform surface measurement was obtained. The standard deviation across this array led to the standard uncertainty shown in Figure 5.19 (*right*) as $u_{RotAngle}$.

The next uncertainty source input to the Monte Carlo simulation was a moving axis of rotation and its standard uncertainty was represented as $u_{RotAxis}$. In the Monte Carlo simulation, it was assumed that the freeform part translated randomly within a square region with a 100- μm length, in the plane perpendicular to the axis of rotation. After running the Monte Carlo loop 1000 times, such that each trial had random rotation axis, an array of possible outcomes of the freeform surface measurement was obtained. The

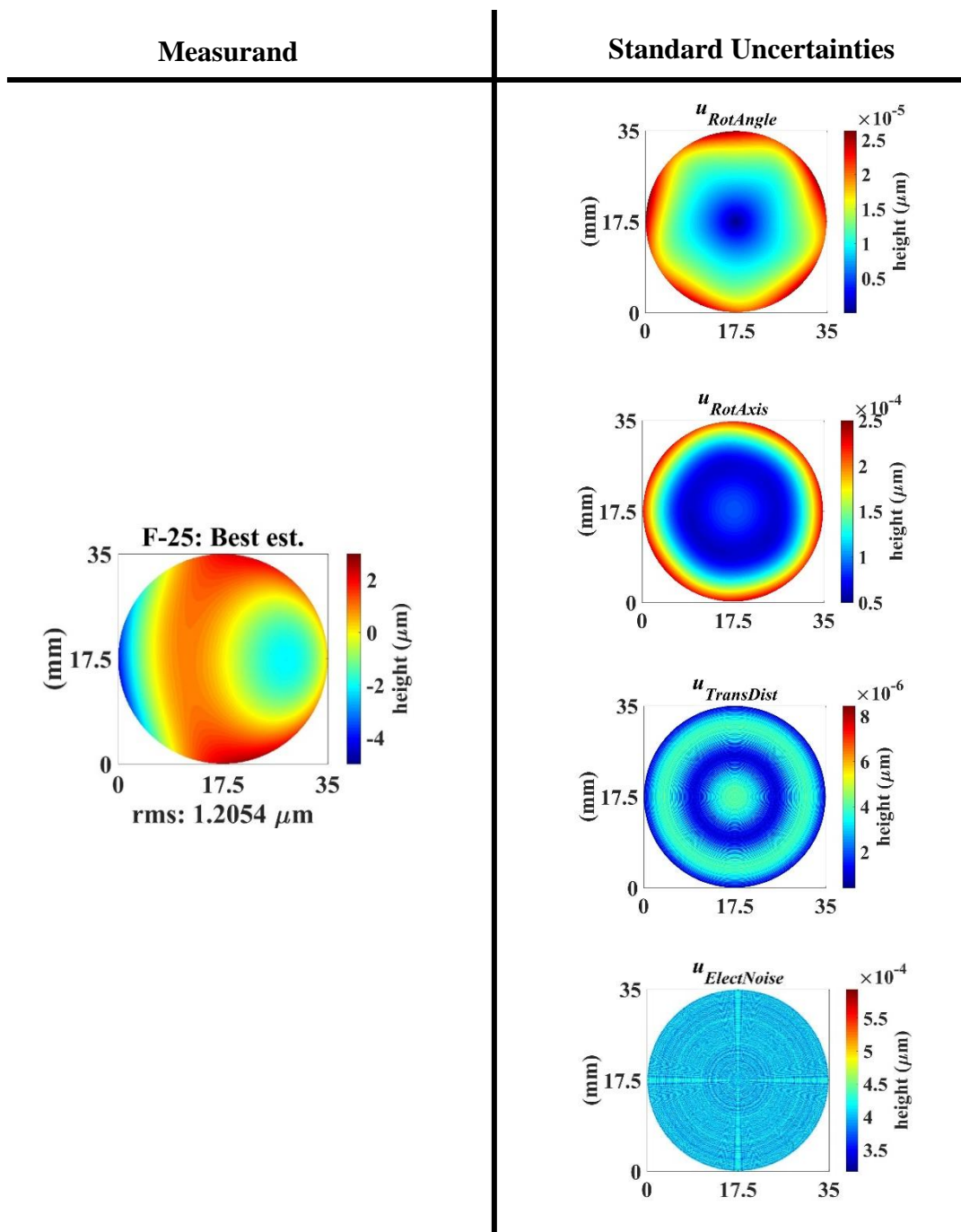


FIGURE 5.19 Best estimate of the freeform from F-25 measurements (*left*). Its standard uncertainties (*right*).

standard deviation across this array led to the standard uncertainty shown in Figure 5.19

(*right*) as $u_{RotAxis}$.

The standard uncertainty because of an uncertainty in the translation distance was represented by $u_{TransDist}$. This input to the Monte Carlo presumed the nominal translation distance of 1 mm (in the RI-Shift technique) varied randomly within upper and lower limits of $\pm 100 \mu\text{m}$. The resulting standard uncertainty after running the Monte Carlo simulation 1000 times is shown in Figure 5.19 (*right*) as $u_{TransDist}$. The fourth standard uncertainty shown in Figure 5.19 (*right*) as $u_{ElectNoise}$, represents an uncertainty because of electronic noise. It is the Monte Carlo's output response to random 10-nm P-V input noise.

The uncertainty maps in Figure 5.19 are standard uncertainties in the low-order best-estimate (the measurand) obtained from low-order Zernike-fit results. With the assumption that the above standard uncertainties were uncorrelated, a combined standard uncertainty, u_C , was obtained from their root sum of squares and reported with a 95th percentile coverage probability ($k = 2$) [97]. This combined standard uncertainty is shown alongside the best estimate of the freeform surface (separated from F-25 measurements) in Figure 5.20.

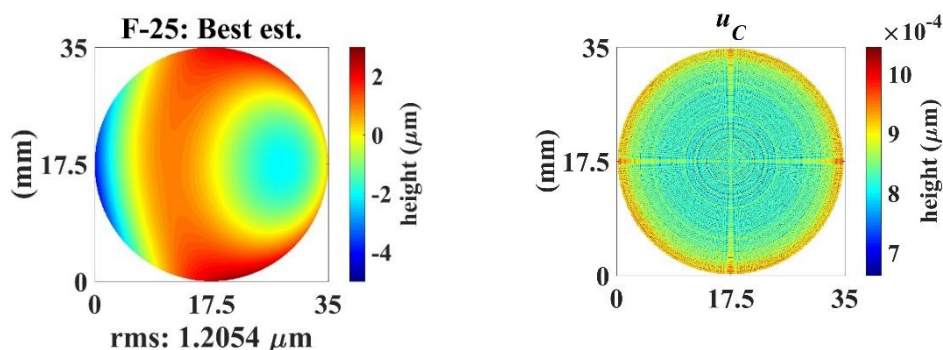


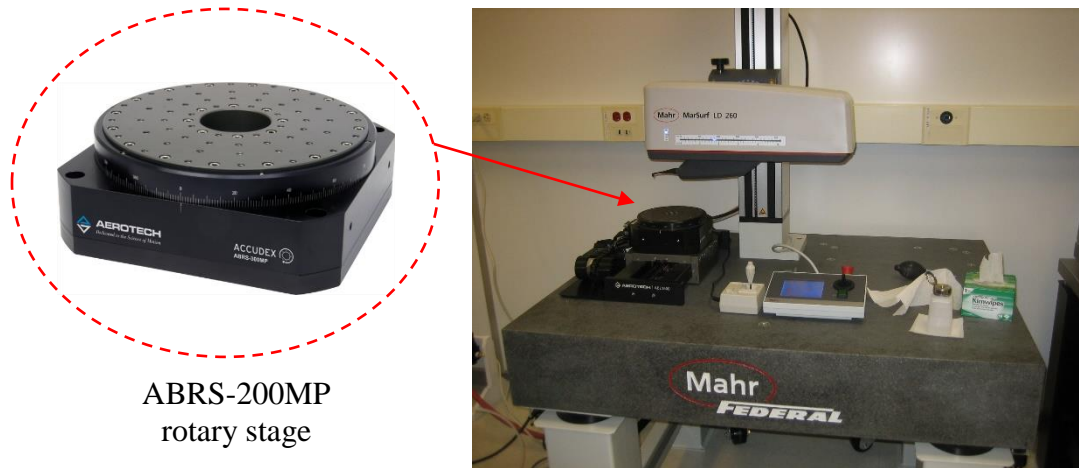
FIGURE 5.20 The best estimate of the freeform surface from F-25 measurements (*left*) and its combined standard uncertainty ($k = 2$) (*right*).

5.4 Measurements of the Freeform Surface on the Mahr Surface Profiler

Unlike the Zeiss F-25 CMM that can probe along the x -, y -, and z - axes and read the x -, y -, and z -point coordinates, the MarSurf LD 260 surface profiler [109] has a probe arm that travels only along the x -axis and reads the z -point coordinates. Since the probe arm travels along one axis, to repeat the Cartesian measurement model described in Chapter 5.3, multiple profiles were measured across the freeform surface by translating or rotating the freeform part between each profile measurement. The translation stage, rotary stage, stage mount and fixture that maneuver the part between profile measurements are mentioned in the next section.

5.4.1 Stages, Mounts and Fixtures that Maneuver the Freeform Part

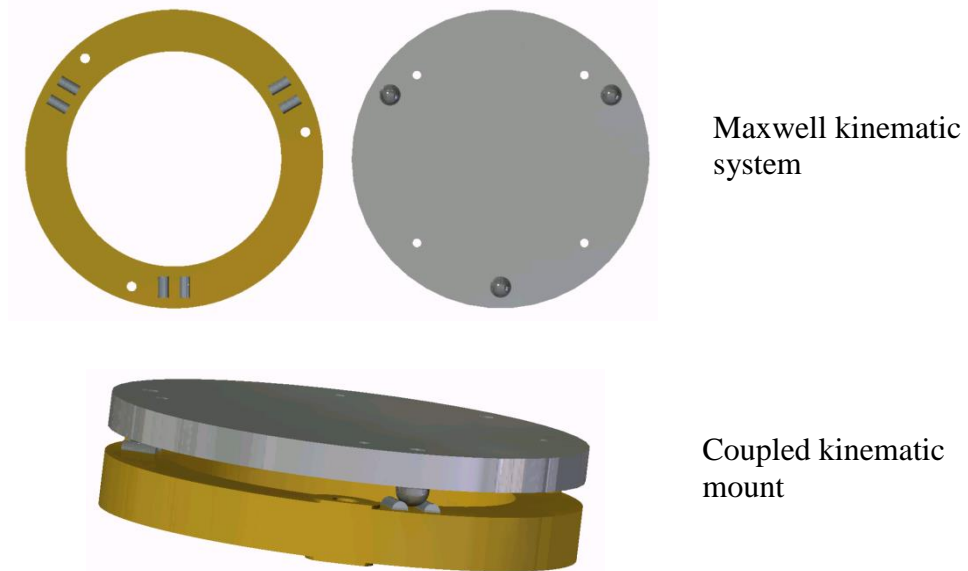
The rotary stage used to rotate the part was an Aerotech ABRS-200MP rotary stage with a 178.1-mm tabletop diameter, installed in the measuring area of the MarSurf LD 260 surface profiler and shown in Figure 5.21. To enable translations of the part, as well as to align the optical axis of the part to the rotation axis of the rotary stage, an x - y stage was mounted on the rotary stage. This x - y stage was not directly fastened to the rotary stage tabletop because the ABRS rotary stage specifications required a mounting interface which was flat to within $2\ \mu\text{m}$ [110]. A second reason for an indirect fastening was to minimize the transfer of twisting stress from the x - y stage to the rotary stage. Halsey (1913) described this stress-minimization by saying “any machine frame standing on three legs is free from twisting stress and from the resulting distortion” [111]. This was addressed by using a kinematic coupling between the two stages.



ABRS-200MP
rotary stage

FIGURE 5.21 The MarSurf LD 260 surface profiler with the affixed rotary stage.

The kinematic coupling between the x - y stage and the rotary was a Maxwell Kinematic System with three truncated spheres on one platform, and three corresponding Vees (a pair of parallel cylinders formed each vee) on the other, as shown in Figure 5.22.



Maxwell kinematic
system

Coupled kinematic
mount

FIGURE 5.22 The arrangement of the cylindrical pairs (*top left*) and spheres (*top right*) of the kinematic mount. The assembled kinematic mount (*bottom*).

The separate parts to be coupled are shown in Figure 5.22 (*top*) while the coupled system is depicted in Figure 5.22 (*bottom*).

The *x-y* stage was a Newport M-401 two-axis linear stage with a square tabletop side length of 139.7 mm and a maximum stage travel of 13 mm. This *x-y* stage, fixtured on the kinematic mount, is depicted in Figure 5.23 while the complete assembly of the *x-y* stage, kinematically coupled to the rotary stage, is shown in Figure 5.24.

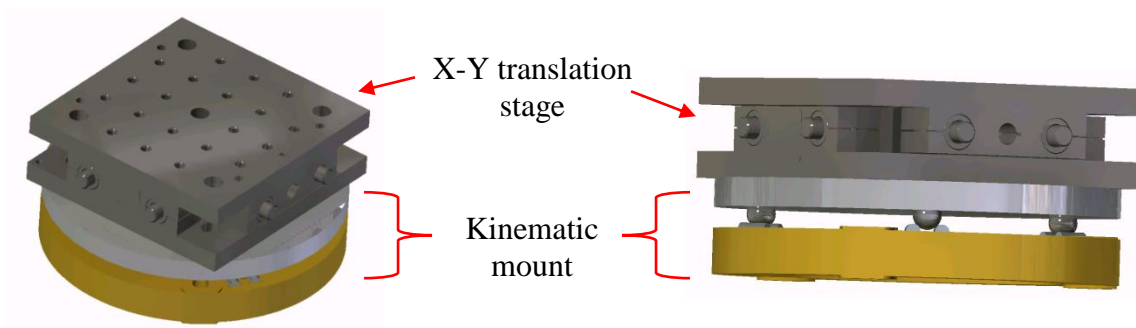


FIGURE 5.23 The *x-y* translation stage fastened to a kinematic mount.

This arrangement allows for alignment of the part's optical axis to the rotary axis of the rotary stage, as well as the required maneuverings of the part between profile measurements.

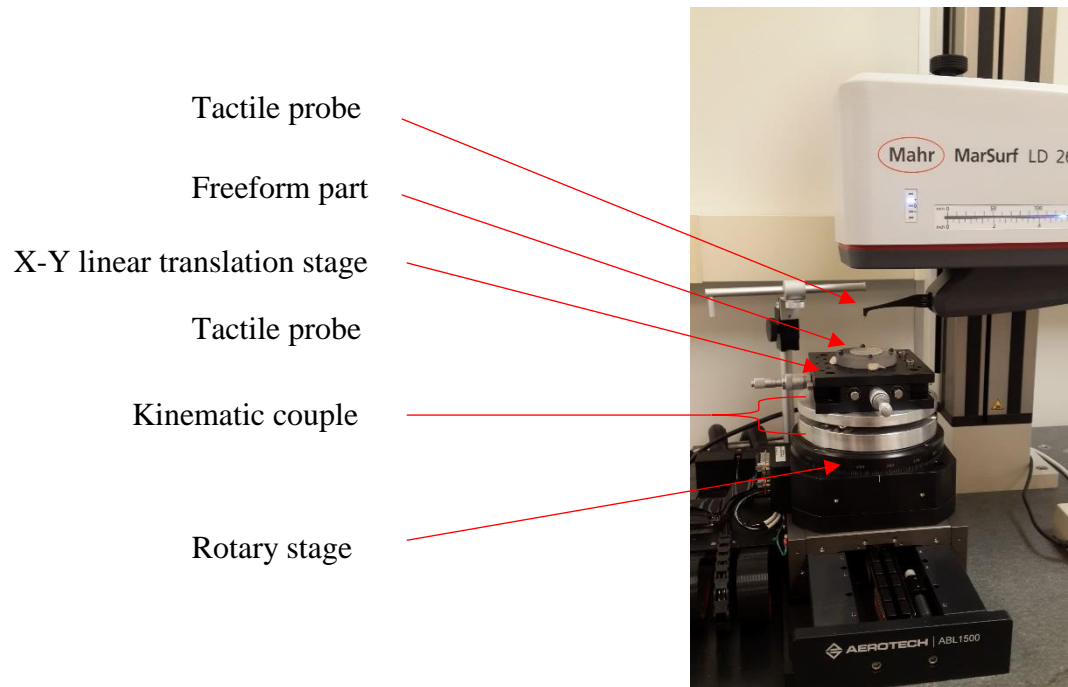


FIGURE 5.24 Assembly of the freeform part, translation stage, and rotary stage on the Mahr surface profiler.

5.4.2 Error Separations of the Rotationally Varying Components

The Cartesian measurement model (described in Chapter 5.3) used to measure the freeform surface on the Zeiss F-25 CMM, was used to measure the freeform surface on the Mahr Surface Profiler. The same Gaussian filter, clear-aperture crop, and tilt- and piston-corrections (applied to the Zeiss CMM measurement results) were applied to the measurement results from the Mahr surface profiler.

To solve for the rotationally varying (RV) components of the freeform surface, the surface was measured with the part positioned at five predefined angular orientations. The surfaces generated from the Mahr measurements of the freeform, at the five angular

orientations of the part separated by 72° , are shown in Figure 5.25, while their corresponding Zernike coefficients are shown in Table 5.5.

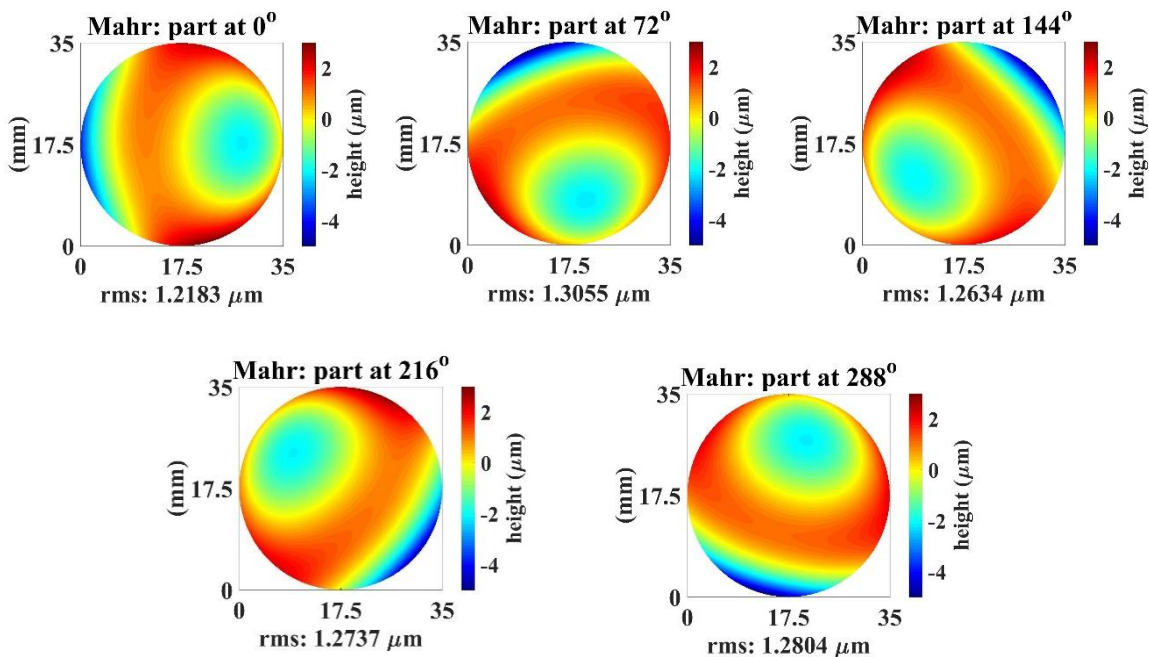


FIGURE 5.25 Mahr LD 260 freeform measurements of the part at five angular orientations.

TABLE 5.17 Zernike coefficients from the Mahr LD 260 freeform surface measurements of the part in five angular orientations.

	Zernike coefficients (nm)											
	Z (2, 0)	Z (2, -2)	Z (2, 2)	Z (3, -1)	Z (3, 1)	Z (3, -3)	Z (3, 3)	Z (4, -4)	Z (4, -2)	Z (4, 0)	Z (4, 2)	Z (4, 4)
Mahr (part at 0°)	47	299	-2262	116	2199	-38	-127	-7	45	62	173	203
Mahr (part at 72°)	-59	-1563	1761	2380	665	33	-257	148	0	-98	-136	-124
Mahr (part at 144°)	-13	2250	-524	1431	-1835	115	412	-205	-56	9	131	71
Mahr (part at 216°)	8	-2197	-855	-1521	-1778	-208	119	179	84	19	20	84
Mahr (part at 288°)	-51	1269	1881	-2366	732	208	-152	-98	-100	-90	-47	-144

The RV component of the freeform surface was deduced from the measurement results in Figure 5.25 by using the N-Rotation technique described in Chapter 2.1. The average of the five maps dropped out the RV component of the part; this average was denoted by $\text{Mean}_{P(\text{rot})}$ and shown Figure 5.26.

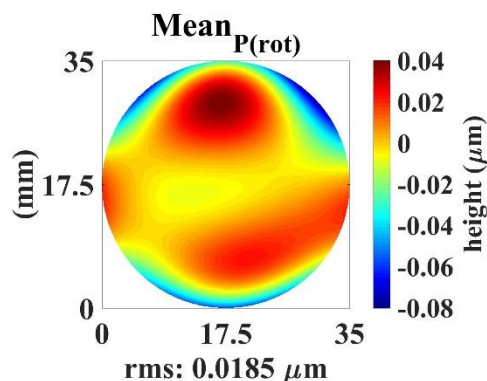


FIGURE 5.26 An average of the Mahr LD 260 freeform surface measurements at the five angular orientations.

The RV component of the part, dropped out by the averaging process, was obtained by subtracting the map in Figure 5.26 from that in Figure 5.25 (*top left*); and the resulting map is shown in Figure 5.27.

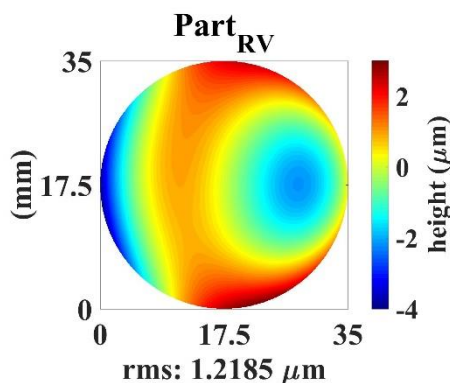


FIGURE 5.27 The separated rotationally varying component of the freeform surface.

This represents the first of the four desired separated components of the Mahr LD 260 freeform surface measurement. The next surface component to be extracted is the RV component of the machine's errors. Since the RV components of the freeform have been

extracted, any residual RV components must come from the machine error contributions. This RV machine error component was obtained by applying the N-Rotation technique to the height map in Figure 5.26; these rotations are shown in Figure 5.28.

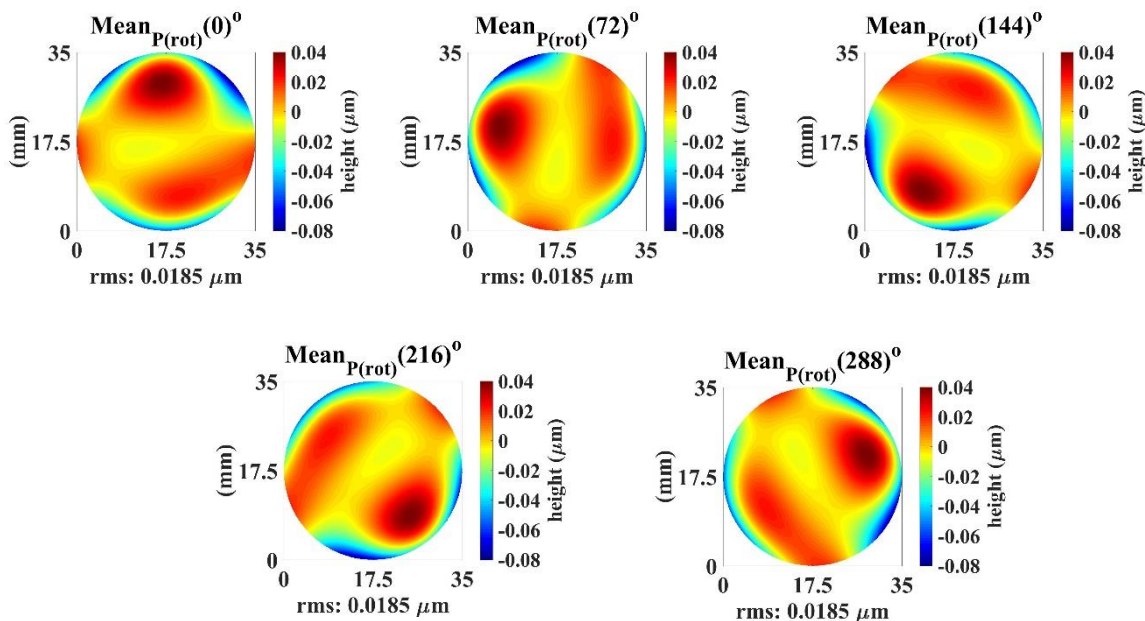


FIGURE 5.28 N-Rotations to extract the machine's rotationally varying error contributions.

The RV components of the machine errors rotate with each of the rotations in Figure 5.28. The average of these height maps drops out the RV machine error components; this average is shown in Figure 5.29.

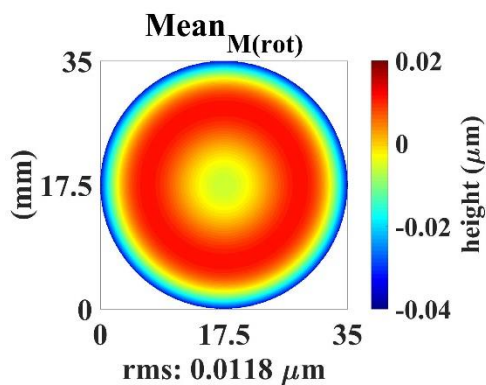


FIGURE 5.29 Average of the height maps that depict machine rotations. This average drops out the rotationally varying components of the machine errors.

The RV machine error component dropped out by the averaging process is shown in Figure 5.30 and represents the second of the four desired separated components.

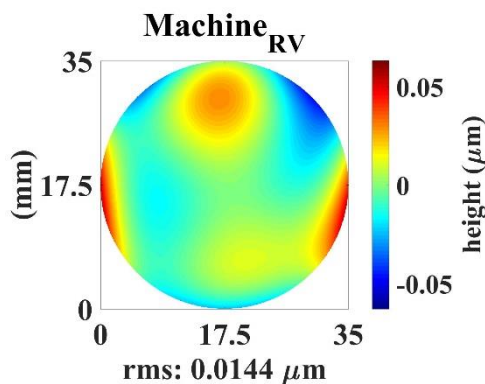


FIGURE 5.30 The separated rotationally varying component of the machine's errors.

So far, the RV components of the test part and machine error contributions have been separated, and the surface in Figure 5.29 contains only convolved RI components of the freeform surface and the machine's errors. These RI components were extracted using the 'Shift' portion of the Shift-Rotation technique.

5.4.3 Error Separations of the Rotationally Invariant Components

The Shift-technique described in Chapter 2.2, and applied to the Zeiss F-25 measurement results, was used to separate the RI components present in Figure 5.29. This error separation required an additional measurement of the freeform surface, after a lateral translation with respect to an initial position. From the difference between the initial and translated measurements, minus RV components, the slope of the part was obtained. A profile from the part center to the edge (in the direction opposite the translation) was extracted from this slope to solve for the radial profile of the freeform surface.

Since the Shift-technique utilizes a difference between profiles from the initial and translated surface measurements, the RI components can be solved from diametrical profiles (instead of areal measurements) measured at the initial and translated positions of

the part. Considering this, a diametrical profile was extracted from the surface in Figure 5.25 (top left), and after translating the freeform part 1-mm along the direction of the diametrical profile, the same profile on the surface was remeasured. These initial and shifted profiles are shown in Figure 5.31. These profiles have been processed; they were cropped to the clear aperture and low-pass filtered with the same Gaussian filter applied to the previous freeform measurements from the Zeiss F-25 CMM and Mahr surface profiler.

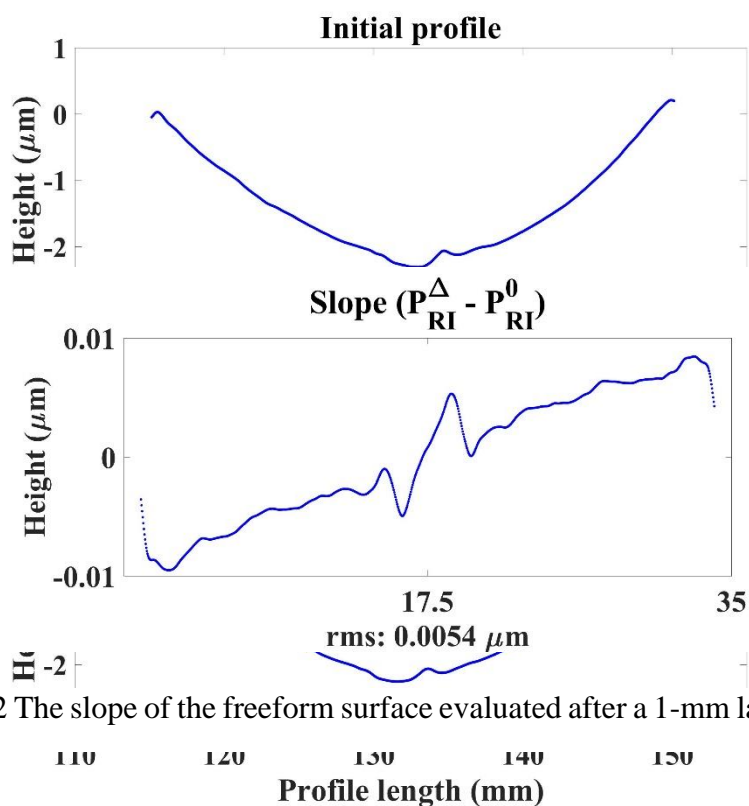


FIGURE 5.32 The slope of the freeform surface evaluated after a 1-mm lateral translation.

FIGURE 5.31 Measurement of a profile on the freeform surface in an initial position (top). Measurement after the freeform part was shifted 1-mm to the left (right).

After removing the RV components present in the profiles above, and assuming the machine errors remained constant between the initial- and translated-profile measurements, a difference between the profiles gave the slope of the part evaluated at the separation and in the translation direction, as shown in Figure 5.32.

The goal of the next step was to deduce the RI component of the freeform surface from the slope profile in Figure 5.32. This was obtained by extracting a portion, \mathbf{g} , of the slope profile and solving the system of linear equations: $\mathbf{g} = \mathbf{H}*\mathbf{f}$ via the pseudo-inverse approach as described in Chapter 2.2 and Chapter 5.3.2. The rotationally invariant component of the freeform surface generated from the solved radial profile, \mathbf{f} , is shown in Figure 5.33 (*left*). This represents the third of the four separated components from the Mahr-freeform surface measurements. The final separated component (the RI component of the machine errors) was obtained by subtracting the separated RV components of the part and machine, and the RI part-component from the measurement of the part in its initial 0° orientation; this result is shown in Figure 5.33 (*right*).

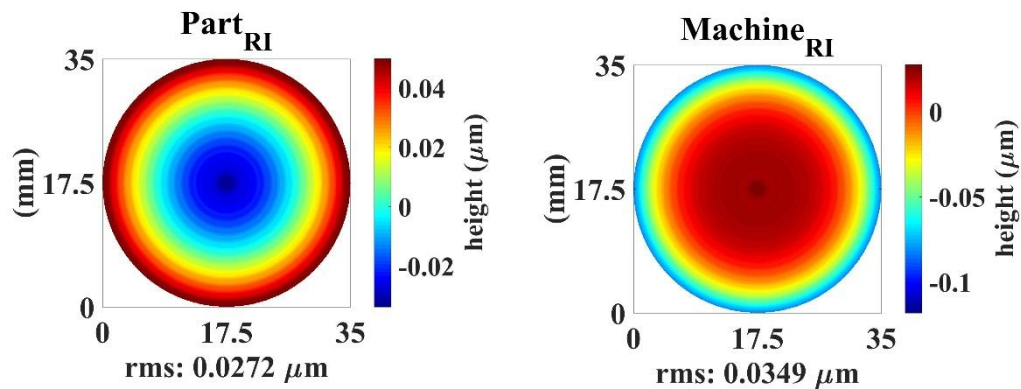


FIGURE 5.33 The solved rotationally invariant component of the freeform surface (*left*). The solved rotationally invariant component of the machine error contributions (*right*).

5.4.4 Best Estimate of the Freeform Surface from the Mahr LD 260

The error separations of the Mahr freeform measurements led to a best estimate of the freeform surface, without machine error contributions. This estimate was obtained by adding the two separated components of the freeform surface. These separated components, shown in Figure 5.27 and Figure 5.33 (*left*), were added to give the best estimate of the freeform in Figure 5.34. The Zernike coefficients from a twelve-Zernike polynomial fit to this best estimate freeform are listed in Table 5.6.

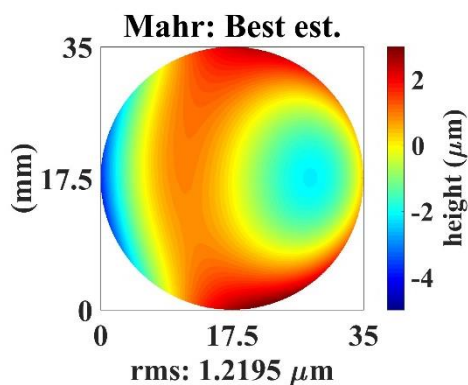


FIGURE 5.34 Best estimate of the freeform surface separated from the Mahr LD 260 measurement results.

TABLE 5.21 Zernike coefficients from a Zernike polynomial fit to the best estimate of the freeform surface.

	Zernike coefficients (nm)											
	Z (2, 0)	Z (2, -2)	Z (2, 2)	Z (3, -1)	Z (3, 1)	Z (3, -3)	Z (3, 3)	Z (4, -4)	Z (4, -2)	Z (4, 0)	Z (4, 2)	Z (4, 4)
Mahr: best est.	101	288	-2262	108	2203	-60	-126	-10	51	79	145	185

5.4.5 Uncertainty Estimations in the Best Estimate from the Mahr profiler

The Monte Carlo simulations in Chapter 5.3.4 were also used to evaluate task-specific uncertainties associated with obtaining the freeform best estimate shown in Figure 5.34. The uncertainty sources used as inputs were the rotation angles, the axis of rotation, the translation distance, and electronic noise. Their standard uncertainties were represented by $u_{RotAngle}$, $u_{RotAxis}$, $u_{TransDist}$, and $u_{ElectNoise}$ respectively, and shown alongside the measurand in Figure 5.35. The best estimate of the freeform surface separated from the Mahr LD 260 measurement results is shown in Figure 5.35 (*left*) while its standard uncertainties are shown in Figure 5.35 (*right*).

The standard uncertainty, $u_{RotAngle}$, represents the uncertainty after each nominal 72° rotation angle varied randomly within upper and lower limits of $\pm 0.05^\circ$. The standard uncertainty, $u_{RotAxis}$, represents the uncertainty after the rotation axis of the freeform part translated randomly within a square region with a $100\text{-}\mu\text{m}$ length, in the plane perpendicular to the axis of rotation. The standard uncertainty, $u_{TransDist}$, represents the uncertainty after the nominal 1-mm translation distance (in the RI-Shift technique) varied randomly within upper and lower limits of $\pm 100\ \mu\text{m}$. The standard uncertainty, $u_{ElectNoise}$, represents an uncertainty because of electronic noise; it is the Monte Carlo's output response to $\pm 5\ \text{nm}$ uniformly distributed input noise.

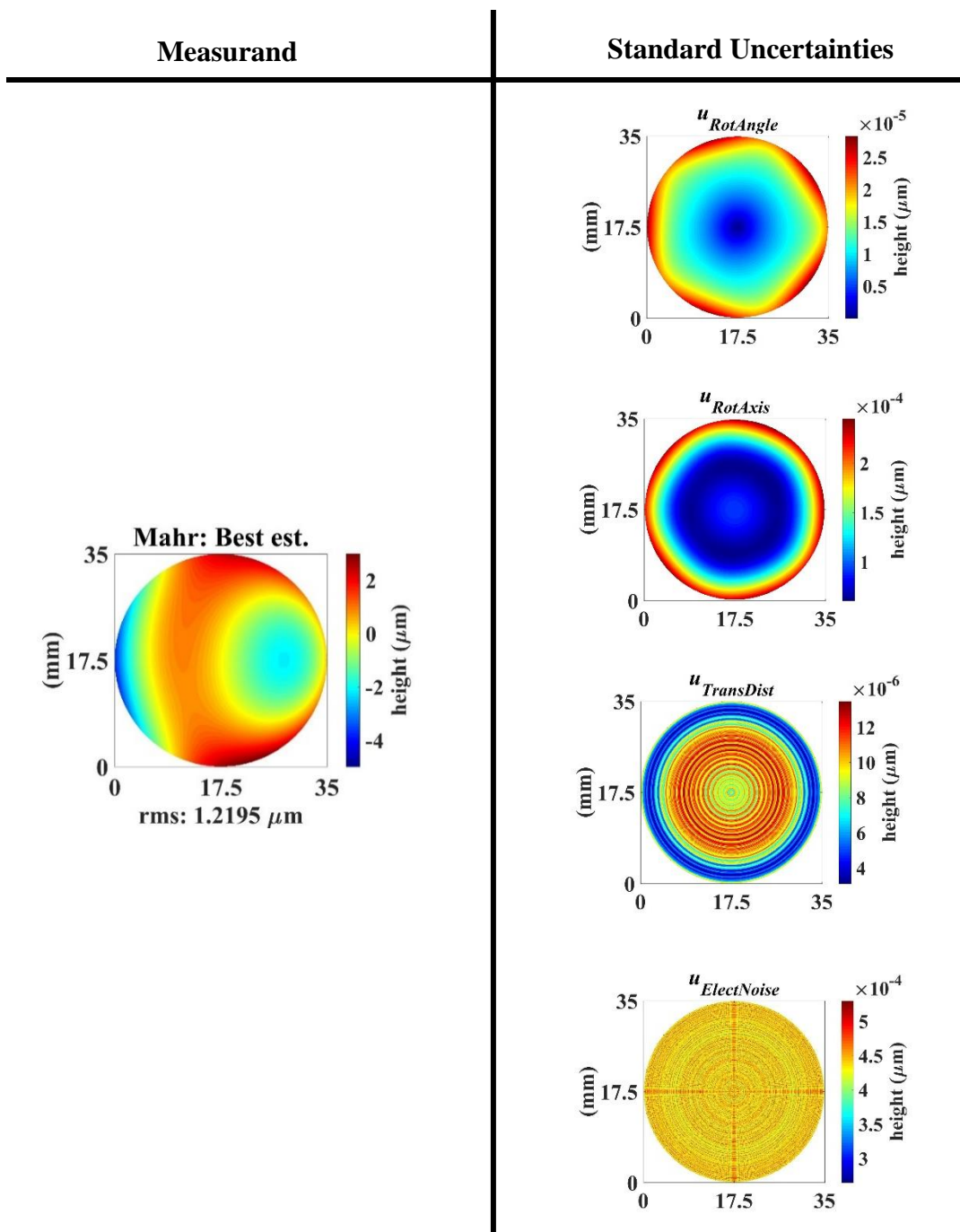


FIGURE 5.35 Best estimate of the freeform from the Mahr LD 260 measurements (*left*). Its standard uncertainties (*right*).

The uncertainty maps in Figure 5.35 are standard uncertainties in the low-order best-estimate (the measurand) obtained from low-order Zernike-fit results. With the assumption that the above standard uncertainties were uncorrelated, a combined standard uncertainty, u_C , was obtained from their root sum of squares and reported with a 95th percentile coverage probability ($k = 2$) [97]. This combined standard uncertainty is shown alongside the best estimate of the freeform surface (separated from Mahr LD 260 measurements) in Figure 5.36.

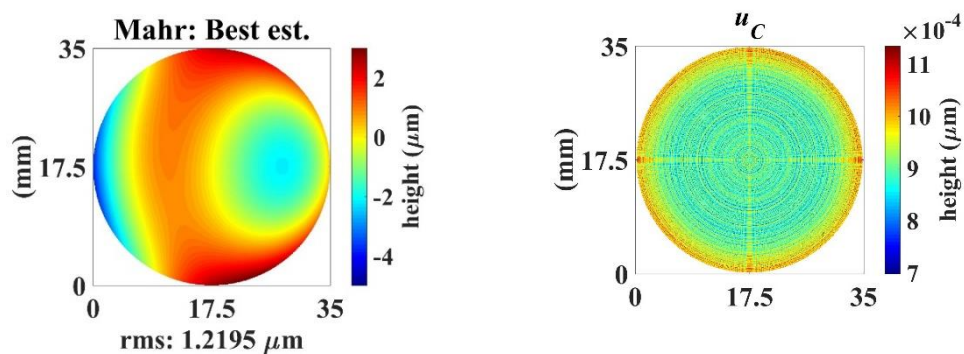


FIGURE 5.36 The best estimate of the freeform surface from Mahr LD 260 measurements (*left*) and its combined standard uncertainty ($k = 2$) (*right*).

5.5 Measurement of the Freeform Surface on the Zygo NexView Interferometer

The freeform surface was measured on the fourth instrument, a Zygo NexView Scanning White Light interferometer. A 2.75X microscope objective was used to measure 75 sites on the freeform surface. These sites were stitched together using an x - y blend stitching algorithm with a 20% overlap region between individual sites. This measurement result was cropped down to the 35-mm clear aperture and fit to twelve Zernike terms. Figure 5.37 shows the surface generated from these twelve Zernike terms while its Zernike coefficients are listed in Table 5.7. The next section compares this NexView freeform measurement result to the Verifire (Fizeau) measurement result and the best estimates from the Zeiss CMM and the Mahr surface profiler.

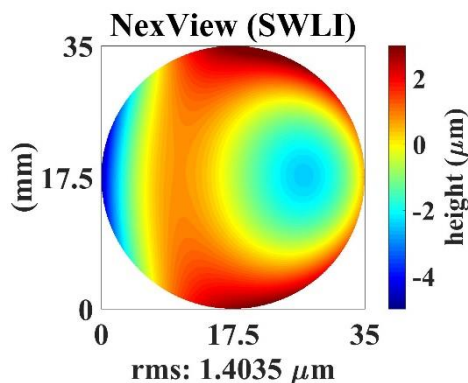


FIGURE 5.37 A NexView measurement of the freeform surface.

TABLE 5.25 Zernike coefficients of the NexView freeform measurement.

	Zernike coefficients (nm)											
	Z (2, 0)	Z (2, -2)	Z (2, 2)	Z (3, -1)	Z (3, 1)	Z (3, -3)	Z (3, 3)	Z (4, -4)	Z (4, -2)	Z (4, 0)	Z (4, 2)	Z (4, 4)
NexView	486	-118	-2569	-58	2503	141	139	-12	-79	-21	-25	9

5.6 Comparisons between Freeform Measurements made on the Four Machines

The Shift-Rotation error separation was applied to the freeform measurements made on the Zeiss F-25 CMM, as well as the Cartesian-model freeform measurements made on the Mahr surface profiler. From these error separations, best estimates of the freeform surface (without machine error contributions) were obtained. This section compares these best estimate results to the freeform measurement results from the optical instruments. Figure 5.38 shows these freeform surface comparisons while Table 5.8 lists their respective Zernike coefficients.

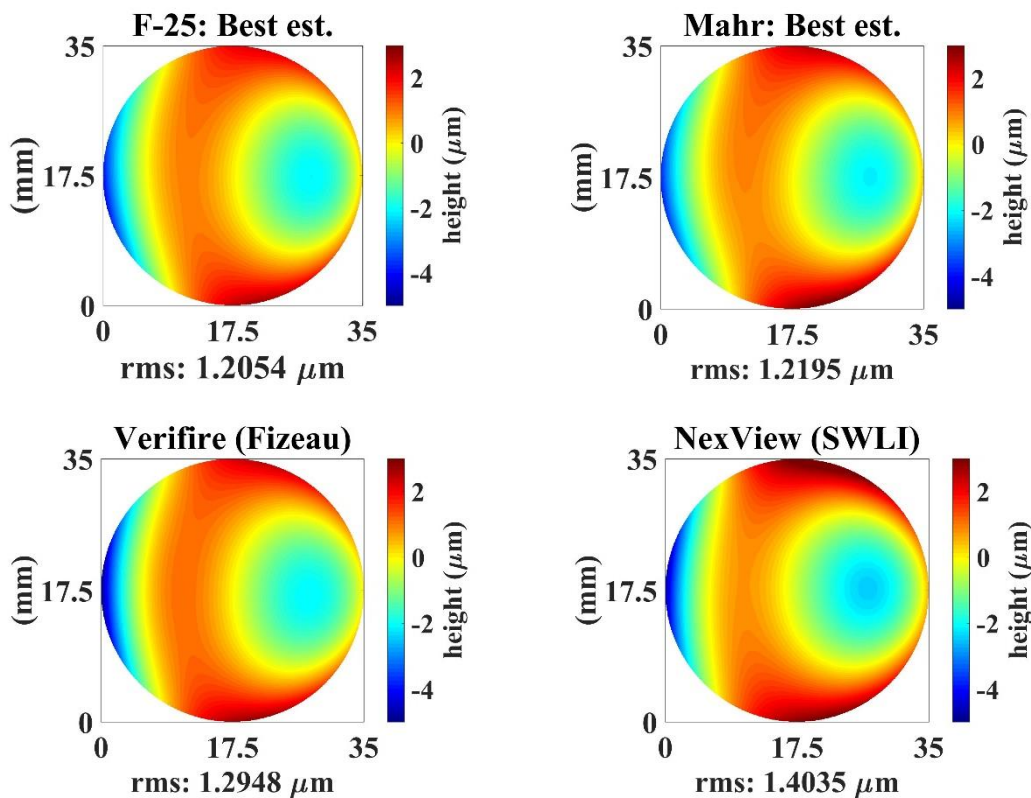


FIGURE 5.38 Freeform surface measurements from four measuring instruments.

TABLE 5.28 Zernike coefficients of the freeform measurement results from the four instruments.

	Zernike coefficients (nm)											
	Z (2, 0)	Z (2, -2)	Z (2, 2)	Z (3, -1)	Z (3, 1)	Z (3, -3)	Z (3, 3)	Z (4, -4)	Z (4, -2)	Z (4, 0)	Z (4, 2)	Z (4, 4)
F-25: best est.	-30	172	-2257	36	2171	-145	-10	32	64	49	216	136
Mahr: best est.	101	288	-2262	108	2203	-60	-126	-10	51	79	145	185
Verifire (Fizeau)	-22	-129	-2390	-125	-2392	109	-151	15	67	-27	-54	6
NexView (SWLI)	486	-118	-2569	-58	2503	141	139	-12	-79	-21	-25	9

For consistency, the surfaces generated from Zernike coefficients from the four measuring instruments had the same grid size with an aperture diameter of 1001 pixels. The maps in Figure 5.38 (as well as all previous maps) have the same aperture diameter of 1001 pixels. The comparison in Table 5.8 was further expressed as the amplitudes (root-sum-square of the sine and cosine Zernike terms, where applicable) of the Zernike coefficients. These amplitudes are reported in Table 5.9.

TABLE 5.27 Amplitude Zernike coefficients of the freeform surfaces from the four instruments.

	Amplitudes of the Zernike coefficients (nm)						
	defocus	astig.	coma	trefoil	spherical	sec. astig	tetrafoil
F-25: best est.	30	2264	2171	145	49	225	140
Mahr: best est.	101	2280	2206	140	79	154	185
Verifire (Fizeau)	22	2393	2395	186	27	86	16
NexView (SWLI)	486	2572	2504	198	21	83	15

The table shows the dominant terms present on the freeform surface are astigmatism and coma. A comparison between these terms shows the best estimates from the Zeiss CMM and the Mahr profiler agree to within 35 nm. On the other hand, the

amplitudes of the astigmatism and coma terms from the optical measurements were higher than those from the tactile instruments.

5.7 Summary

This chapter demonstrated that the Shift-Rotation technique can be applied to coordinate measuring machine (CMM) and profilometer measurement results. A freeform surface was measured on a Zeiss F-25 CMM and a Mahr LD 260 surface profiler. On both machines, the surface was measured at predetermined angular rotations and translations of the surface. These measurement results were decomposed with the Shift-Rotation into rotationally varying and invariant freeform surface components (and machine error contributions), to obtain best-estimate freeform measurements without machine error contributions.

Task-specific uncertainties associated with these freeform best estimates, from the CMM and profilometer, were evaluated using Monte Carlo simulations. The uncertainty sources used as inputs to the Monte Carlo simulation were the rotation angles, the axis of rotation, the translation distance, and electronic noise.

The dominant terms present on the freeform surface were astigmatism and coma. A comparison between the Zernike-coefficient amplitudes of these terms showed the best estimates from the Zeiss CMM and the Mahr profiler agreed to within 35 nm. These comparisons, and the error separation of the freeform measurement results, demonstrate that the Shift-Rotation calibration technique can be applied to CMM and profilometer measurements to minimize task-specific uncertainty by separating machine error contributions.

CHAPTER 6: CONCLUSIONS AND FUTURE WORK

6.1 Conclusions

In this research, task-specific measurement uncertainty was minimized by applying an in-situ self-calibration technique, known as Shift-Rotation, to freeform surface measurements. Shift-Rotation is an absolute testing procedure developed in interferometric optical surface metrology to separate measurement results into system errors and test piece errors [20, 21, 53-64]. This calibration method requires surface measurements after rotations and translations of the test part and relies on the decomposition of surface departures into rotationally varying (RV) and rotationally invariant (RI) components.

Simulations were used to demonstrate the Shift-Rotation technique. The technique minimizes task-specific uncertainty by separating machine errors from test part measurements. These machine errors contain geometric and computational errors [48] and a number of methods are available for evaluating the errors [48-51]. With the Shift-Rotation technique, it is unnecessary to measure these machine errors which include the parametric errors (21 D. o. F for a 3-axis machine), since the separated RV and RI components of the machine errors can be added to give a representation of the task-specific machine error contributions. These machine error contributions can be separated out, on a task-specific basis, anywhere in the machine's measurement volume. Also, since this calibration method requires stability only over the measurement cycle time, effects of machine drifts are reduced to the timescale of the measurement rather than the interval between machine calibrations.

Simulations were also used to estimate uncertainties associated with applying the Shift-Rotation technique to measurements of freeform surfaces. These were Monte Carlo simulations that evaluated standard uncertainty contributions from potential sources inherent in the shift- and rotation-measurement process. These uncertainty sources were the rotation angles, the axis of rotation, the translation distance, and electronic noise. The standard uncertainty in the rotation angle was obtained after each nominal rotation angle varied randomly within upper and lower limits of $\pm 0.05^\circ$. The standard uncertainty in the axis of rotation was obtained after the rotation axis of every simulated part (in the N-rotation technique) fell anywhere within a 300- μm square center. The standard uncertainty in the translation distance was obtained after the nominal translation distance (in the RI-Shift technique) varied randomly within upper and lower limits of 200 μm . The standard uncertainty in the electronic noise was the Monte Carlo's output response after adding ± 5 nm uniformly distributed electronic noise to every simulated surface. With the assumption that these standard uncertainties were uncorrelated, a combined standard uncertainty was obtained from their root sum of squares and reported alongside the best estimate of the measurand.

The Shift-Rotation technique is a form metrology but its error separations of some mid-spatial frequency (MSF) patterns were simulated. These MSF errors could be left behind by some sub-aperture fabrication and finishing processes, and examples of the simulated MSF patterns include sinusoidal MSF errors, on- and off-axis spiral MSF errors, and crosshatch MSF errors. The simulations demonstrated that the Shift-Rotation process separates the MSF errors into RV and RI components but if the MSF errors are not described as purely RV or RI, the error separations would result in residual MSF

components. These residuals would be reported convolved with the RI components of the machine errors and further information would be required to deconvolve the errors.

The next step involved experimental validation of the Shift-Rotation error separation technique. The error separation was demonstrated by measuring a freeform surface on a Coordinate Measuring Machine (CMM) and a tactile profilometer. This freeform surface was fabricated on a BK7 optical flat, on a magnetorheological finishing (MRF) machine. It was housed in a polycarbonate mount with four silicon carbide balls and a reference mark that transferred coordinates from MRF to metrology, it had an outer diameter of 40-mm and a clear aperture of about 35-mm.

This freeform surface was measured on two touch-probe machines: a Zeiss F-25 micro-CMM and a Mahr MarSurf LD 260 surface profiler, according to the Shift-Rotation measurement procedures explained in Chapter 2. From these measurement results, rotationally varying and invariant freeform surface components (and machine error contributions) were separated, to obtain best-estimate freeform measurements without machine error contributions. These best-estimates from the tactile machines were compared to optical measurements of the same freeform surface. The optical measurements were from a Zygo Verifire Fizeau interferometer and a Zygo NexView Scanning White Light interferometer. A comparison of the dominant terms on the freeform surface showed the best estimates from the Zeiss CMM and the Mahr profiler agree to within 35 nm. The research demonstrated that the Shift-Rotation calibration technique can be applied to CMM and profilometer measurements to minimize task-specific uncertainty by separating machine error contributions.

6.2 Future Work

6.2.1 A More Robust Noise-Modification of a Singular Matrix

The technique used to separate the rotationally invariant components involved calculating the inverse of a singular matrix. Besides a pseudo-inverse, an alternative approach was investigated. This alternative approach did not seek a pseudo-inverse solution, but focused on converting the singular matrix into a non-singular (invertible) matrix. This was achieved by adding negligible non-symmetric noise to the singular matrix to perturb the linear dependencies between its rows and columns, in such a way that the singular matrix became a well-behaved non-singular matrix.

Simulations showed this approach yielded the same or more accurate solutions than the pseudo-inverse approach but the experimental validations showed otherwise. In this research, the negligible noise was added to the diagonal of the singular matrix to offset the symmetry of its design. The noise was added to the diagonal because the singular matrix was designed to have two non-zero elements in each row, and these included diagonal elements. Further work is required to determine optimum and robust ways of adding noise to singular matrices to make them invertible.

6.2.2 Filtering Effect of Probe-Ball Radius

A tactile CMM and a tactile profilometer were used to scan profiles across a freeform surface but the filtering effects of their probe ball radii on the profile measurement results were not investigated. Since comparisons were made between touch-probe measurements from different machines, research into the possible probe-induced dilation and erosion filtering effects could improve the comparisons.

REFERENCES

- [1] X. Jiang, P. Scott, and D. Whitehouse, "Freeform surface characterisation-a fresh strategy," *CIRP Annals-Manufacturing Technology*, vol. 56, pp. 553-556, 2007.
- [2] E. Savio, L. De Chiffre, and R. Schmitt, "Metrology of freeform shaped parts," *CIRP Annals - Manufacturing Technology*, vol. 56, pp. 810-835, // 2007.
- [3] F. Z. Fang, X. D. Zhang, A. Weckenmann, G. X. Zhang, and C. Evans, "Manufacturing and measurement of freeform optics," *CIRP Annals - Manufacturing Technology*, vol. 62, pp. 823-846, // 2013.
- [4] K. Garrard, T. Bruegge, J. Hoffman, T. Dow, and A. Sohn, "Design tools for freeform optics," in *Optics & Photonics 2005*, 2005, pp. 58740A-58740A-11.
- [5] S. Wills, "Freeform Optics: Notes from the Revolution," *Optics and Photonics News*, vol. 28, pp. 34-41, 2017.
- [6] W. T. Plummer, "Free-form optical components in some early commercial products," in *Proc. SPIE*, 2005, pp. 67-73.
- [7] I. Kitajima, "Improvement in lenses," *British patent*, vol. 250, pp. 1669-1671, 1926.
- [8] B. H. James, "Lens of variable focal power having surfaces of involute form," ed: Google Patents, 1949.
- [9] L. W. Alvarez, "Two-element variable-power spherical lens," ed: Google Patents, 1967.
- [10] J. G. Baker, "Variable power, analytic function, optical component in the form of a pair of laterally adjustable plates having shaped surfaces, and optical systems including such components," ed: Google Patents, 1971.
- [11] S. S. Rege, T. S. Tkaczyk, and M. R. Descour, "Application of the Alvarez-Humphrey concept to the design of a miniaturized scanning microscope," *Optics express*, vol. 12, pp. 2574-2588, 2004.
- [12] A. Simonov, M. Rombach, G. Vdovin, and M. Loktev, "Varifocal optics for a novel accommodative intraocular lens," in *MOEMS-MEMS 2006 Micro and Nanofabrication*, 2006, pp. 61130B-61130B-7.
- [13] P. J. Smilie, B. S. Dutterer, J. L. Lineberger, M. A. Davies, and T. J. Suleski, "Design and characterization of an infrared Alvarez lens," *Optical Engineering*, vol. 51, pp. 013006-1-013006-8, 2012.
- [14] S. F. Busch, J. C. Balzer, G. Bastian, G. E. Town, and M. Koch, "Extending the Alvarez-Lens Concept to Arbitrary Optical Devices: Tunable Gratings, Lenses, and Spiral Phase Plates," *IEEE Transactions on Terahertz Science and Technology*, vol. 7, pp. 320-325, 2017.
- [15] W. Ip and M. Loftus, "Adaptive and compensation methods in free-form surface assessment," *Proceedings of the Institution of Mechanical Engineers, Part B: Journal of Engineering Manufacture*, vol. 210, pp. 135-145, 1996.
- [16] D. Ma, Z. Feng, and R. Liang, "Tailoring freeform illumination optics in a double-pole coordinate system," *Applied Optics*, vol. 54, pp. 2395-2399, 2015/03/20 2015.
- [17] J. M. Rodgers and K. P. Thompson, "Benefits of freeform mirror surfaces in optical design," in *Proceedings of the American Society of Precision Engineering 2004 Winter Topical Meeting on Freeform Optics*, 2004, pp. 73-78.
- [18] D. Malacara, *Optical shop testing* vol. 59: John Wiley & Sons, 2007.

- [19] D. Malacara and A. Cornejo, "Testing of aspherical surfaces with Newton fringes," *Applied optics*, vol. 9, pp. 837-839, 1970.
- [20] B. Dörband and G. Seitz, "Interferometric testing of optical surfaces at its current limit," *Optik-International Journal for Light and Electron Optics*, vol. 112, pp. 392-398, 2001.
- [21] H. Ichikawa and T. Yamamoto, "Apparatus and method for wavefront absolute calibration and method of synthesizing wavefronts," U.S. Patent No. 5,982,490, 1999.
- [22] B. Doerband, "High precision testing of optical components," in *International Optical Design Conference*, 1998, pp. 484-489.
- [23] J. Burge, D. Anderson, D. Ketelsen, and S. West, "Null test optics for the MMT and Magellan 6.5-m f/1.25 primary mirrors," in *Proc. SPIE*, 1994, pp. 658-669.
- [24] J. E. Greivenkamp, "Testing aspheric surfaces," *Optics and Photonics News*, vol. 1, pp. 25-27, 1990.
- [25] J. H. Burge, "Applications of computer-generated holograms for interferometric measurement of large aspheric optics," in *Proc. SPIE*, 1995, pp. 258-269.
- [26] S. Arnold, "interferometric null testing of aspheres," *SPIE Newsroom SPIE Newsroom*, 2002.
- [27] P. Murphy, J. Fleig, G. Forbes, D. Miladinovic, G. DeVries, and S. O'Donohue, "Subaperture stitching interferometry for testing mild aspheres," in *Proc. SPIE*, 2006, p. 62930J.
- [28] J. Fleig, P. Dumas, P. E. Murphy, and G. W. Forbes, "An automated subaperture stitching interferometer workstation for spherical and aspherical surfaces," in *Proc. of SPIE Vol*, 2003, p. 297.
- [29] X. Wang, L. Wang, L. Yin, B. Zhang, D. Fan, and X. Zhang, "Measurement of large aspheric surfaces by annular subaperture stitching interferometry," *Chinese Optics Letters*, vol. 5, pp. 645-647, 2007.
- [30] M. Tricard, A. Kulawiec, M. Bauer, G. DeVries, J. Fleig, G. Forbes, *et al.*, "Subaperture stitching interferometry of high-departure aspheres by incorporating a variable optical null," *Cirp Annals-Manufacturing Technology*, vol. 59, pp. 547-550, 2010.
- [31] J. Wyant, "Testing aspherics using two-wavelength holography," *Applied Optics*, vol. 10, pp. 2113-2118, 1971.
- [32] K. Creath, Y.-Y. Cheng, and J. C. Wyant, "Contouring aspheric surfaces using two-wavelength phase-shifting interferometry," *Journal of Modern Optics*, vol. 32, pp. 1455-1464, 1985.
- [33] A. Beutler, "Comparison of 2D and 3D measurements of aspheres with a tactile and optical sensor on one measuring instrument," in *Optical Fabrication and Testing*, 2014, p. OTu4A. 1.
- [34] D. S. Anderson and J. H. Burge, "Swing-arm profilometry of aspherics," in *Proc. SPIE*, 1995, pp. 269-279.
- [35] R. Henselmans, L. Cacace, G. Kramer, P. Rosielle, and M. Steinbuch, "The NANOMEFOS non-contact measurement machine for freeform optics," *Precision Engineering*, vol. 35, pp. 607-624, 2011.
- [36] T. Kart, G. Kosoglu, H. Yuksel, and M. N. Inci, "3D optical profilometry using a fiber optic Lloyd's mirror," in *Proc. of SPIE Vol*, 2014, pp. 920409-1.

- [37] A. Beutler, "3D profilometry on aspheric and freeform lenses," in *Proc. of SPIE Vol.*, 2011, pp. 80821J-1.
- [38] J. F. Ellison and S. VanKerkhove, "Characterization of symmetric aberrations in aspheric surfaces using noncontact profilometry," in *Proceedings of SPIE*, 2003, pp. 347-354.
- [39] R. Palum, "Aspheric surface figure measurement using mechanical profilometry," in *30th Annual Technical Symposium*, 1987, pp. 79-87.
- [40] L. D. Lund, "Direct Contact Profilometry Of Large Aspherics," in *1986 Technical Symposium Southeast*, 1986, pp. 75-79.
- [41] J. L. Pearson, G. W. Roberts, P. Rees, and S. J. Thompson, "Use of a NOM profilometer to measure large aspheric surfaces," *Proc. SPIE 9628, Optical Systems Design 2015: Optical Fabrication, Testing, and Metrology V*, vol. 9628, 2015.
- [42] Y. Li and P. Gu, "Free-form surface inspection techniques state of the art review," *Computer-Aided Design*, vol. 36, pp. 1395-1417, 2004/11/01/ 2004.
- [43] G. Sironi, O. Citterio, G. Pareschi, B. Negri, A. Ritucci, R. Subranni, *et al.*, "MPR: innovative 3D free-form optics profilometer," in *Proceedings of SPIE, the International Society for Optical Engineering*, 2011.
- [44] J. A. Gómez-Pedrero, D. Rodríguez-Ibañez, J. Alonso, and J. A. Quirgoa, "Design and development of a profilometer for the fast and accurate characterization of optical surfaces," in *Proc. SPIE*, 2015, p. 96281I.
- [45] J. M. Sprauel, J. M. Linares, J. Bachmann, and P. Bourdet, "Uncertainties in CMM Measurements, Control of ISO Specifications," *CIRP Annals - Manufacturing Technology*, vol. 52, pp. 423-426, 2003/01/01/ 2003.
- [46] D. Flack, "Measurement good practice Guide No. 42: CMM verification," *National Physical Laboratory*, 2001.
- [47] H. Kunzmann and F. Wäldele, "Performance of CMMs," *CIRP Annals - Manufacturing Technology*, vol. 37, pp. 633-640, 1988/01/01/ 1988.
- [48] D. Flack, "Co-ordinate measuring machine task-specific measurement uncertainties," vol. Measurement Good Practice Guide No. 130. National Physical Laboratory., 2013.
- [49] E. Trapet and F. Wäldele, "A reference object based method to determine the parametric error components of coordinate measuring machines and machine tools," *Measurement*, vol. 9, pp. 17-22, 1991.
- [50] C. Lim and M. Burdekin, "Rapid volumetric calibration of coordinate measuring machines using a hole bar artefact," *Proceedings of the Institution of Mechanical Engineers, Part B: Journal of Engineering Manufacture*, vol. 216, pp. 1083-1093, 2002.
- [51] R. J. Hocken and P. H. Pereira, *Coordinate measuring machines and systems*: CRC Press, 2016.
- [52] S. Sartori and G. Zhang, "Geometric error measurement and compensation of machines," *CIRP Annals-Manufacturing Technology*, vol. 44, pp. 599-609, 1995.
- [53] C. J. Evans, R. J. Hocken, and W. T. Estler, "Self-calibration: reversal, redundancy, error separation, and 'absolute testing'," *CIRP Annals-Manufacturing Technology*, vol. 45, pp. 617-634, 1996.

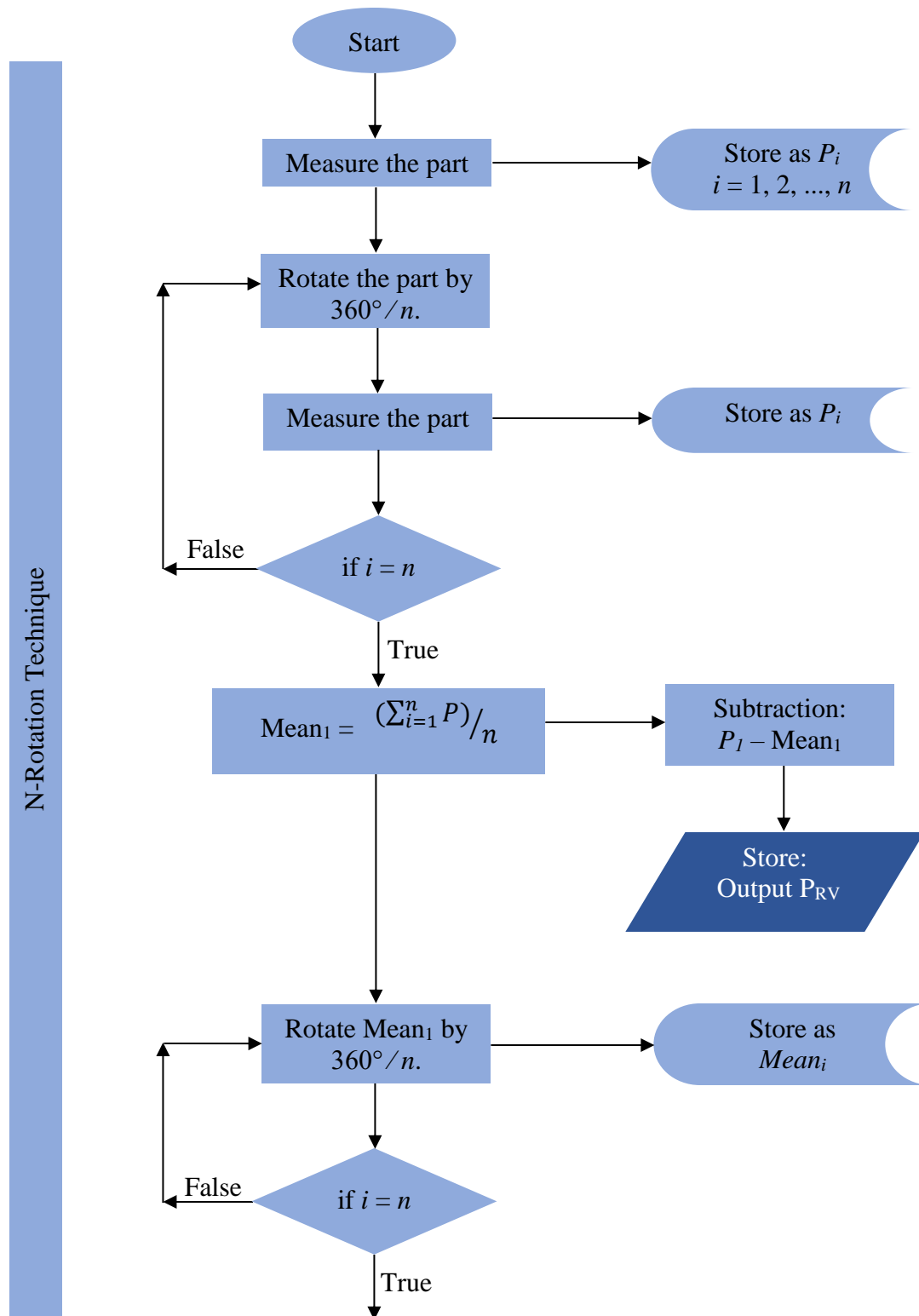
- [54] W. Song, S. Li, X. Hou, F. Wu, W. Zhao, and Y. Wan, "Absolute calibration for Fizeau interferometer with the global optimized shift-rotation method," *Optics and Lasers in Engineering*, vol. 54, pp. 49-54, 2014.
- [55] W. Song, X. Hou, F. Wu, and Y. Wan, "Absolute interferometric shift-rotation method with pixel-level spatial frequency resolution," *Optics and Lasers in Engineering*, vol. 54, pp. 68-72, 2014.
- [56] B. Dörband, H. Müller, and G. Seitz, "High Precision Interferometric Measurements of Lens Elements," in *Fringe*, 1997, pp. 15-17.
- [57] W. Song, F. Wu, X. Hou, G. Wu, B. Liu, and Y. Wan, "Absolute calibration of a spherical reference surface for a Fizeau interferometer with the shift-rotation method of iterative algorithm," *Optical Engineering*, vol. 52, pp. 033601-033601, 2013.
- [58] K. Otaki, T. Yamamoto, Y. Fukuda, K. Ota, I. Nishiyama, and S. Okazaki, "Accuracy evaluation of the point diffraction interferometer for extreme ultraviolet lithography aspheric mirror," *Journal of Vacuum Science & Technology B: Microelectronics and Nanometer Structures Processing, Measurement, and Phenomena*, vol. 20, pp. 295-300, 2002.
- [59] I. Fujimoto, T. Takatsuji, K. Nishimura, and M. Y. Kim, "Autonomous calibration method of the reference flat surface of an interferometer without using a standard flat surface," *Applied optics*, vol. 51, pp. 4754-4767, 2012.
- [60] D. Su, E. Miao, Y. Sui, and H. Yang, "Absolute surface figure testing by shift-rotation method using Zernike polynomials," *Optics letters*, vol. 37, pp. 3198-3200, 2012.
- [61] W. Song, F. Wu, X. Hou, W. Zhao, and Y. Wan, "Absolute measurement of flats with the method of shift-rotation," *Optical Review*, vol. 20, pp. 374-377, September 01 2013.
- [62] Z. Yang, Z. Gao, D. Zhu, and Q. Yuan, "Absolute ultra-precision measurement of high-numerical-aperture spherical surface by high-order shift-rotation method using Zernike polynomials," *Optics Communications*, vol. 355, pp. 191-199, 2015/11/15/ 2015.
- [63] H. Ma, L. Zhang, Y. Yang, Q. Yuan, Z. Shi, and H. Ren, "The transmitted wavefront of spherical lens measured by rotation-shift method," *IJLEO Optik - International Journal for Light and Electron Optics*, vol. 127, pp. 7908-7912, 2016.
- [64] B. Dörband, *Handbook of Optical Systems, Metrology of Optical Components and Systems* vol. 5: John Wiley & Sons, 2012.
- [65] C. J. Evans and R. N. Kestner, "Test optics error removal," *Applied Optics*, vol. 35, pp. 1015-1021, 1996.
- [66] W. P. Kuhn, "Precision surface measurement," U.S. Patent No. 7,158,914, 2007.
- [67] J. A. Soons and U. Griesmann, "Absolute interferometric tests of spherical surfaces based on rotational and translational shears," in *SPIE Optical Engineering+ Applications*, 2012, pp. 84930G-84930G-12.
- [68] C. J. Evans and W. P. Kuhn, "Method and apparatus for tilt corrected lateral shear in a lateral shear plus rotational shear absolute flat test," U.S. Patent No. 7,446,883, 2008.
- [69] R. K. Tyson, "Conversion of Zernike aberration coefficients to Seidel and higher-order power-series aberration coefficients," *Optics letters*, vol. 7, pp. 262-4, 1982.

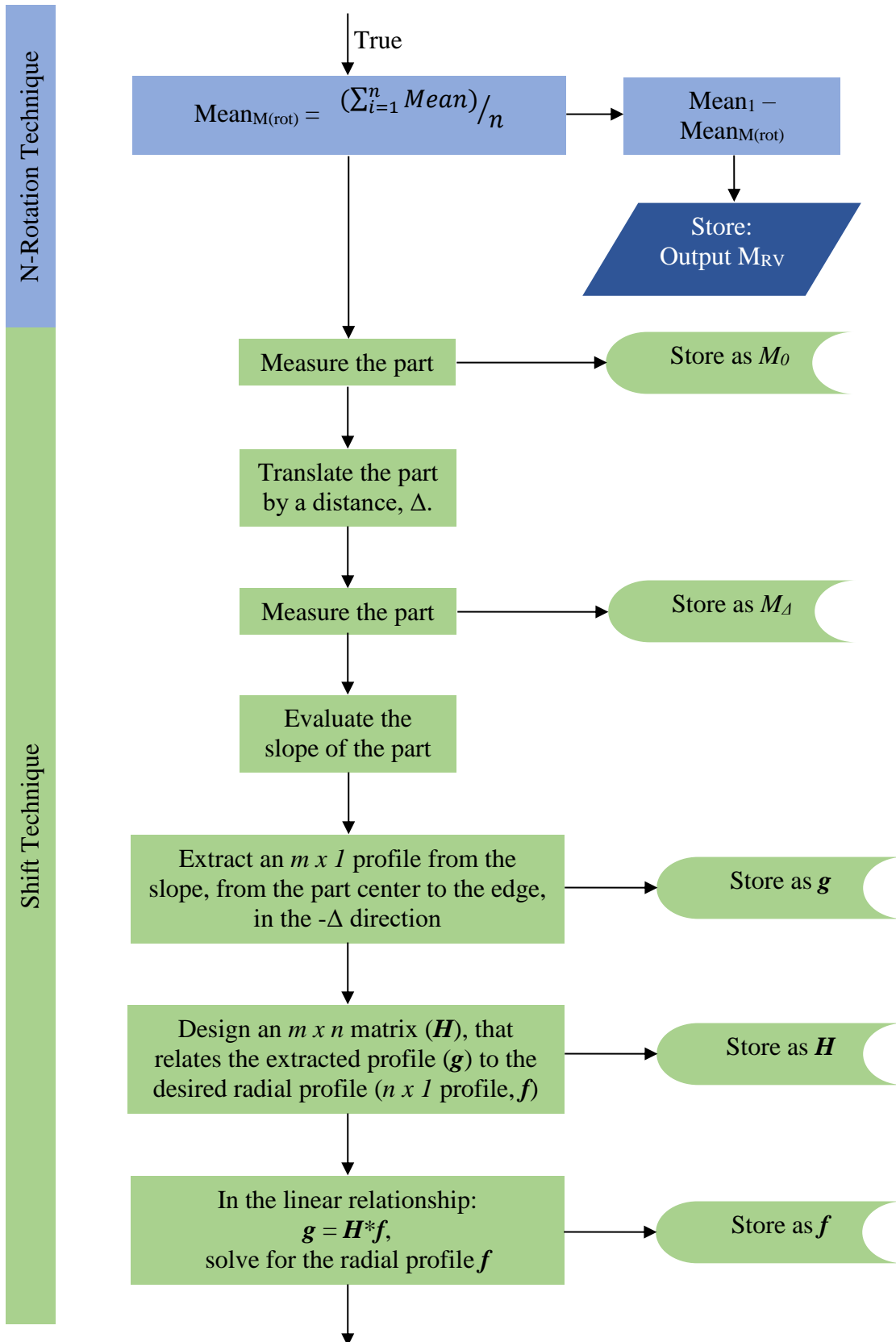
- [70] R. J. Noll, "Zernike polynomials and atmospheric turbulence," *JOsA*, vol. 66, pp. 207-211, 1976.
- [71] J. C. Wyant and K. Creath, "Basic wavefront aberration theory for optical metrology," *Applied optics and optical engineering*, vol. 11, pp. 28-39, 1992.
- [72] V. Lakshminarayanan and A. Fleck, "Zernike polynomials: a guide," *Journal of Modern Optics*, vol. 58, pp. 545-561, 2011.
- [73] M. J. Healy, *Matrices for statistics*: Oxford University Press, 2000.
- [74] M. Fiedler, *Special matrices and their applications in numerical mathematics*: Courier Corporation, 2008.
- [75] J. R. Schott, *Matrix analysis for statistics*: John Wiley & Sons, 2016.
- [76] C. G. Cullen, *Matrices and linear transformations*: Courier Corporation, 2012.
- [77] S. Barnett, "Matrices. Methods and applications," *Oxford Applied Mathematics and Computing Science Series, Oxford: Clarendon Press*, 1990, vol. 1, 1990.
- [78] J. M. Ortega, *Matrix theory: A second course*: Springer Science & Business Media, 2013.
- [79] M. A. Rakha, "On the Moore–Penrose generalized inverse matrix," *Applied Mathematics and Computation*, vol. 158, pp. 185-200, 2004.
- [80] R. Penrose, "A generalized inverse for matrices," in *Mathematical proceedings of the Cambridge philosophical society*, 1955, pp. 406-413.
- [81] J. R. Magnus and H. Neudecker, "Matrix differential calculus with applications in statistics and econometrics," 1995.
- [82] R. A. Horn and C. R. Johnson, *Matrix analysis*: Cambridge university press, 2012.
- [83] P. G. Ciarlet, B. Miara, and J.-M. Thomas, *Introduction to numerical linear algebra and optimisation*: Cambridge University Press, 1989.
- [84] G. H. Golub and C. F. Van Loan, *Matrix computations* vol. 3: JHU Press, 2012.
- [85] R. Wilhelm, R. Hocken, and H. Schwenke, "Task specific uncertainty in coordinate measurement," *CIRP Annals-Manufacturing Technology*, vol. 50, pp. 553-563, 2001.
- [86] E. Trapet, "The virtual CMM concept, advanced mathematical tools in metrology II," *World Scientific*, vol. 40, pp. 238-247, 1995.
- [87] H. Kunzmann, E. Trapet, and F. Waldele, "Concept for the traceability of measurements with coordinate measuring machines," in *Proc. of the 7th Int. Precision Engineering Seminar, Kobe, Japan, Springer Verlag*, 1993, pp. 40-52.
- [88] M. Trenk, M. Franke, and H. Schwenke, "The 'Virtual CMM'a software tool for uncertainty evaluation—practical application in an accredited calibration lab," *Proc. of ASPE: Uncertainty Analysis in Measurement and Design*, 2004.
- [89] H. Haitjema, B. Van Dorp, M. Morel, and P. H. Schellekens, "Uncertainty estimation by the concept of virtual instruments," in *Proc. SPIE*, 2001, p. 147.
- [90] S. D. Phillips, B. R. Borchardt, D. S. Sawyer, W. T. Estler, D. E. Ward, K. Eberhardt, *et al.*, "The calculation of CMM measurement uncertainty via the method of simulation by constraints," in *American Society for Precision Engineering*, 1997.
- [91] A. Balsamo, M. Di Ciommo, R. Mugno, B. Rebaglia, E. Ricci, and R. Grella, "Evaluation of CMM uncertainty through Monte Carlo simulations," *CIRP Annals-Manufacturing Technology*, vol. 48, pp. 425-428, 1999.

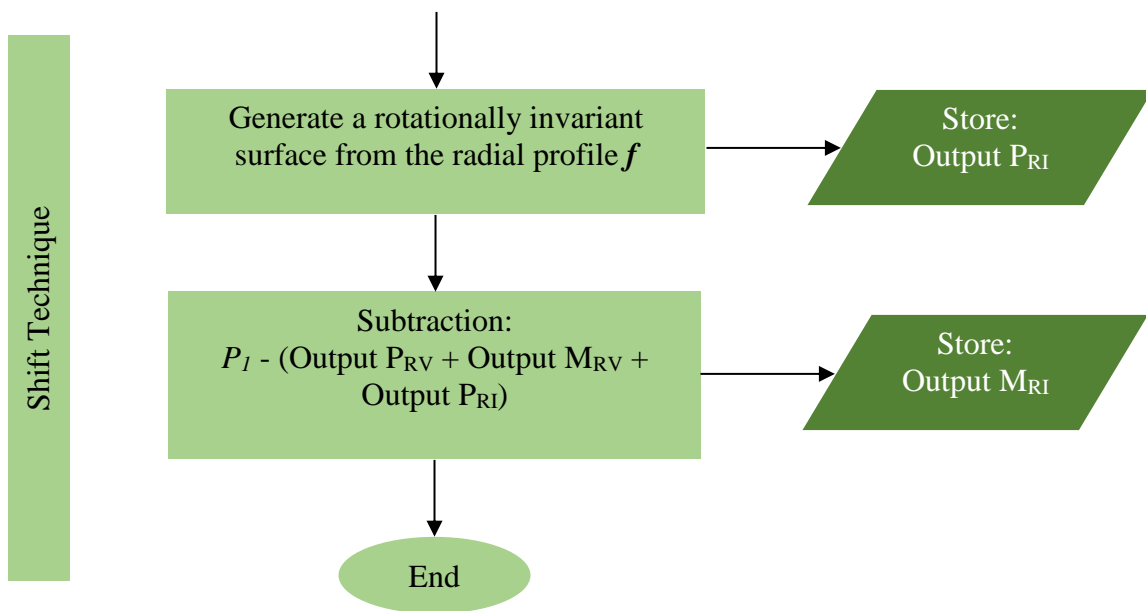
- [92] H. Schwenke, B. Siebert, F. Wäldele, and H. Kunzmann, "Assessment of uncertainties in dimensional metrology by Monte Carlo simulation: proposal of a modular and visual software," *CIRP Annals-Manufacturing Technology*, vol. 49, pp. 395-398, 2000.
- [93] B. IUPAP, "Evaluation of Measurement Data—Supplement 2 to the ‘Guide to the Expression of Uncertainty in Measurement’—Extension to any number of output quantities," 2011.
- [94] C. J. Evans, "P_{Vr}—a robust amplitude parameter for optical surface specification," *Optical Engineering*, vol. 48, pp. 043605-043605-8, 2009.
- [95] N. A. J. Hastings, "Statistical distributions; a handbook for students and practitioners," 1974.
- [96] C. F. Dietrich, *Uncertainty, calibration and probability: the statistics of scientific and industrial measurement*: CRC Press, 1991.
- [97] S. Bell, "Measurement Good Practice Guide No. 11 (Issue 2)," *A Beginner's Guide to Uncertainty of Measurement*. National Physical Laboratory Teddington, Middlesex, United Kingdom, 2001.
- [98] A. Duparre, J. Ferre-Borrull, S. Gliech, G. Notni, J. Steinert, and J. M. Bennett, "Surface characterization techniques for determining the root-mean-square roughness and power spectral densities of optical components," *Applied optics*, vol. 41, pp. 154-171, 2002.
- [99] B. Muralikrishnan and J. Raja, *Computational surface and roundness metrology*: Springer Science & Business Media, 2008.
- [100] J. Hou, D. Liao, and H. Wang, "Development of multi-pitch tool path in computer-controlled optical surfacing processes," *Journal of the European Optical Society-Rapid Publications*, vol. 13, p. 22, 2017.
- [101] Y. Dai, F. Shi, X. Peng, and S. Li, "Restraint of mid-spatial frequency error in magneto-rheological finishing (MRF) process by maximum entropy method," *Science in China Series E: Technological Sciences*, vol. 52, pp. 3092-3097, 2009.
- [102] G. Yu, H. Li, and D. Walker, "Removal of mid spatial-frequency features in mirror segments," *Journal of the European Optical Society-Rapid publications*, vol. 6, 2011.
- [103] P. De Groot, "Handbook of Optical Metrology: Principles and Applications," *Interference Microscopy for Surface Structure Analysis*, "Second Edition," CRC Press, Boca Raton, vol. 31, pp. 791-828, 2015.
- [104] J. A. Menapace, P. J. Davis, W. A. Steele, L. L. Wong, T. I. Suratwala, and P. E. Miller, "MRF applications: measurement of process-dependent subsurface damage in optical materials using the MRF wedge technique," Lawrence Livermore National Laboratory (LLNL), Livermore, CA2005.
- [105] T. P. Metals. (2017, 02/03/2017). *Blanchard grinding*. Available: <http://tciprecision.com/contract-machining/grinding/blanchard-grinding/>
- [106] I. Precision Grinding. (2013, 02/03/2017). *Large plate Blanchard ground*. Available: <https://www.flickr.com/photos/pgiphotos/9493625011/>
- [107] "Work done by UNCC students: H. Shahinian & T. Noste," 2016.
- [108] C. Zeiss. (2007). *F25 Measuring Nanometers*. Available: http://moncktons.com/docs/zeiss_f25.pdf

- [109] Mahr. *MarSurf LD 130 / LD 260*. Available: <https://www.mahr.com/en/Services/Production-metrology/Products/MarSurf---PC-Based-Roughness-Measuring-Units/MarSurf-LD-130---LD-260/>
- [110] I. Aerotech, "ABRS Series Stage User's Manual," ed, 2011.
- [111] F. A. Halsey, *Handbook for Machine Designers and Draftsmen*: McGraw-Hill book Company, Incorporated, 1913.

APPENDIX A: FLOWCHART OF THE SHIFT-ROTATION TECHNIQUE







APPENDIX B: INFLUENCE OF RANDOM MACHINE Z-AXIS ERRORS

APPENDIX B.1 Influence of 1% Random Machine Z-axis Errors

The added random machine errors were reduced from a maximum of 10% to 1% the nominal systematic machine errors. Figure B.1 (*left*) shows a simulated systematic machine error, without random errors in the z-axis, while Figure B.1 (*right*) shows the

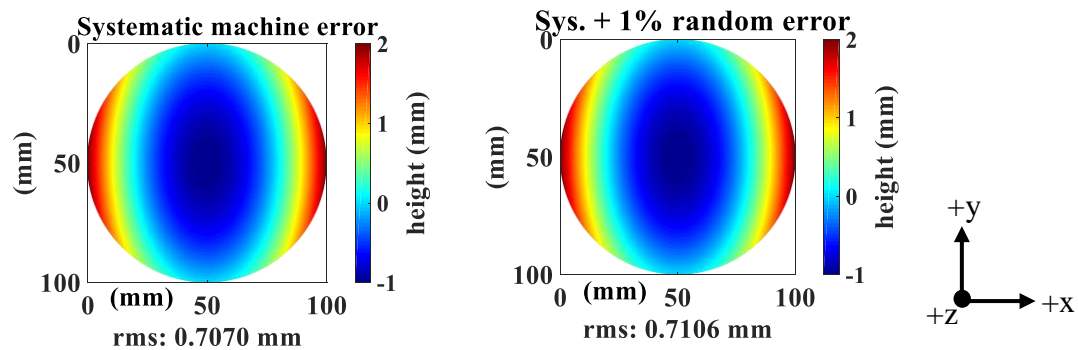


FIGURE B.1 Simulated systematic machine errors (*left*). The machine's systematic errors with a random component in the z-direction. The random errors have a maximum amplitude of 1% the nominal systematic error. (*right*).

resulting machine error after the addition of a random machine z-axis error with a maximum amplitude of 1% deviation from the nominal.

To evaluate the effects of the added random errors on the error separation process, the Shift-Rotation error separations were carried out on a simulated part with the systematic and random errors shown in Figure B.1 (*right*). After Shift-Rotation error separations (4 rotations in the N-Rotation technique, and a 200 μm part translation in the Shift-technique) of the part that included the random machine errors, the separated output components were compared to the input components, as shown in Figure B.2. A comparison between the output and input rotationally varying components, shows that even with the added 1% random machine errors, the N-Rotation technique correctly separated the RV components

of the part and machine. The rms of the Output P_{RV} height map equals that of the Input P_{RV} , while the rms of the Output M_{RV} height map differed from the Input M_{RV} by 0.5%.

On the other hand, more significant changes were observed between the output and input RI components. After the addition of 1% random machine errors, the Shift technique imperfectly solved for the RI components. There was a 1% rms deviation between the Output and Input P_{RI} height maps, and a 30% rms deviation between the Output and Input M_{RI} height maps. The rms of this part estimate differed from its corresponding input by 0.5%.

The difference height maps which result from the addition of 1% random machine z-axis errors are shown in Figure B.3. Comparing the rms values of the RV differences, to those of the RI differences, shows that the addition of the 1% random machine z-axis errors, had negligible effect on the separation of the RV components but had a more significant effect on the separation of the RI components. The RI rms deviations were 2 orders of magnitude, larger than the RV rms deviations.

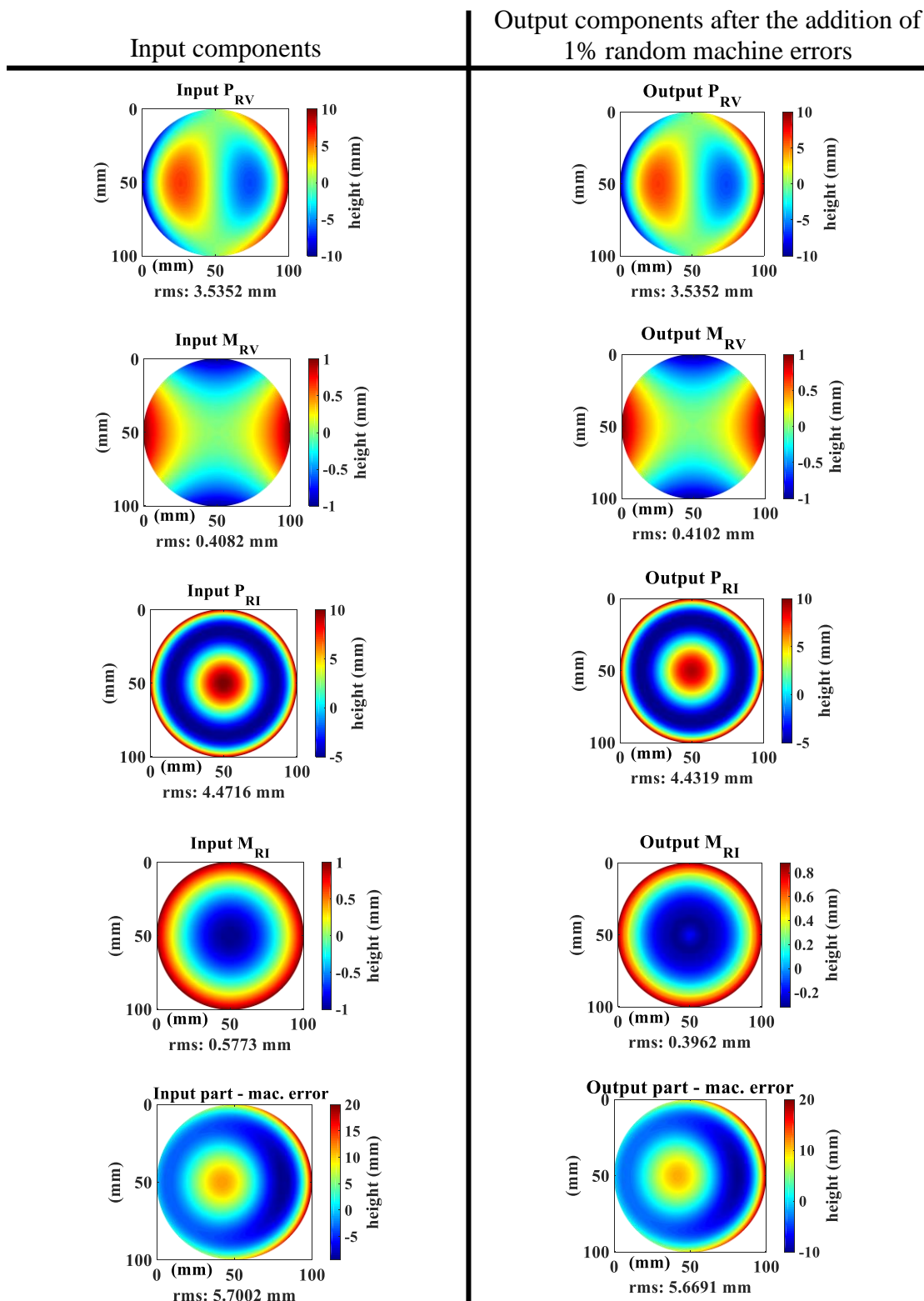
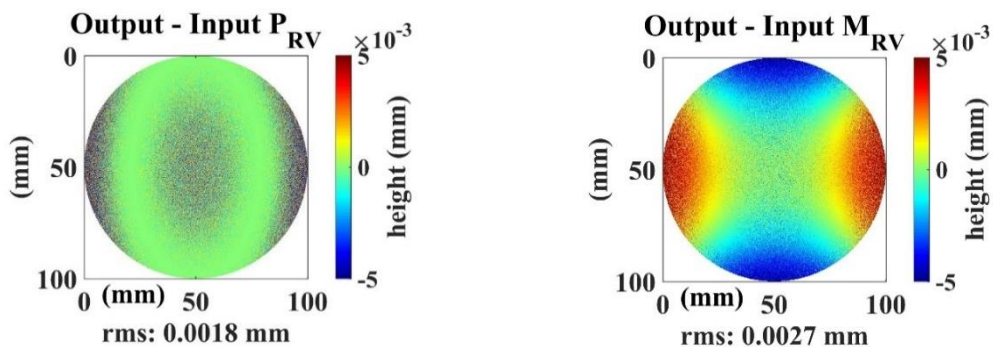


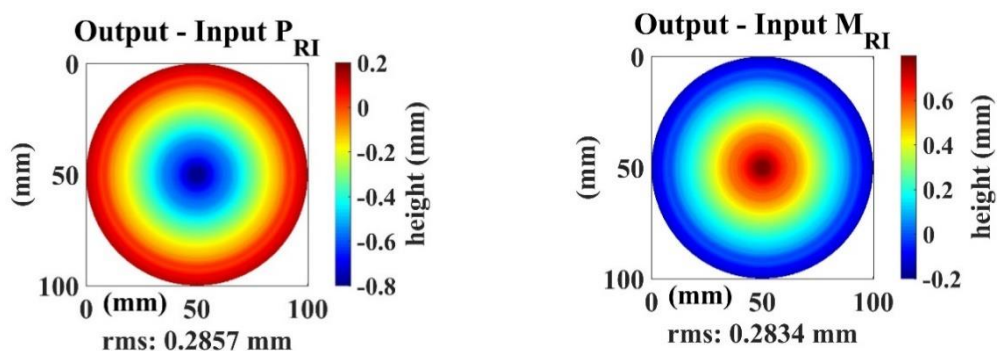
FIGURE B.2 Input components to the Shift-Rotation technique (*left*). Output components obtained after the addition of random z-axis machine errors with maximum amplitudes of 1% deviation from the nominal (*right*).

Differences between output and input surface components, after the addition of 1% random machine z-axis errors

Differences between rotationally varying components



Differences between rotationally invariant components



Difference between output and input best estimates of the part

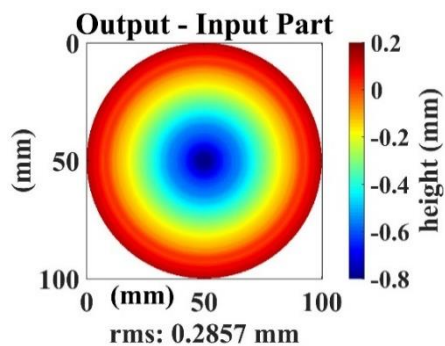


FIGURE B.3 Differences between output and input surface components, after the addition of 1% random machine z-axis errors.

APPENDIX B.2 Influence of 0.1% Random Machine Z-axis Errors

The added random machine errors were further reduced from a maximum of 1% to 0.1% the nominal systematic machine errors. Figure B.4 (*left*) shows a simulated systematic machine error, without random errors in the z-axis, while Figure B.4 (*right*) shows a resulting machine error after the addition of a random machine z-axis error, with

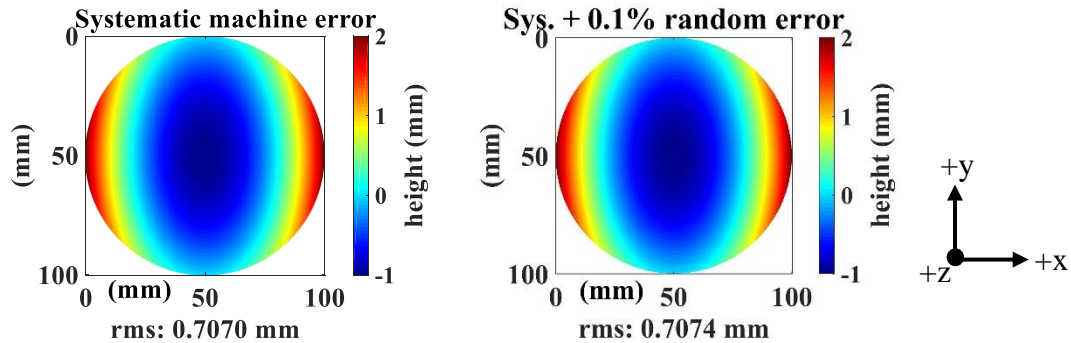


FIGURE B.4 Simulated systematic machine errors (*left*). The machine's systematic errors with a random component in the z-direction. The random errors have a maximum amplitude of 0.1% the nominal systematic error (*right*).

a maximum amplitude of 0.1% deviation from the nominal. These added errors were on a pixel-by-pixel basis and an effect of the added random error can be noticed by the change in the rms of the height maps.

Similar to the previous section, in order to evaluate the effects of the added random errors on the error separation process, the Shift-Rotation error separations were carried out on a simulated part with the systematic and random errors shown in Figure B.4 (*right*). After Shift-Rotation error separations of the part that included the random machine errors, the separated output components were compared to the input components and shown in Figure B.5. Similar to the previous simulations (where 10% and 1% random errors were added), Figure B.5 shows that the N-Rotation technique correctly separated the RV components. The rms of the Output P_{RV} height map equals that of the Input P_{RV} , while the

rms of the Output M_{RV} height map differed from the Input M_{RV} by 0.05%. Figure B.5 also shows an improvement in the Shift-technique's separation of the RI components; the random errors reduced from 1% to 0.1%. The rms of the Output P_{RI} height map differed from that of the corresponding input by 0.03%, while the rms of the Output M_{RI} height map differed from its input by 2%.

The difference height maps which resulted from the addition of 0.1% random machine z-axis errors are shown in Figure B.6. Comparing the rms values of the RV differences, to those of the RI differences, shows that the addition of the 0.1% random machine z-axis errors had little effect on the separation of the RV components but had a more significant effect on the separation of the RI components. The RI rms deviations were about 1 or 2 orders of magnitude larger than the RV rms deviations.

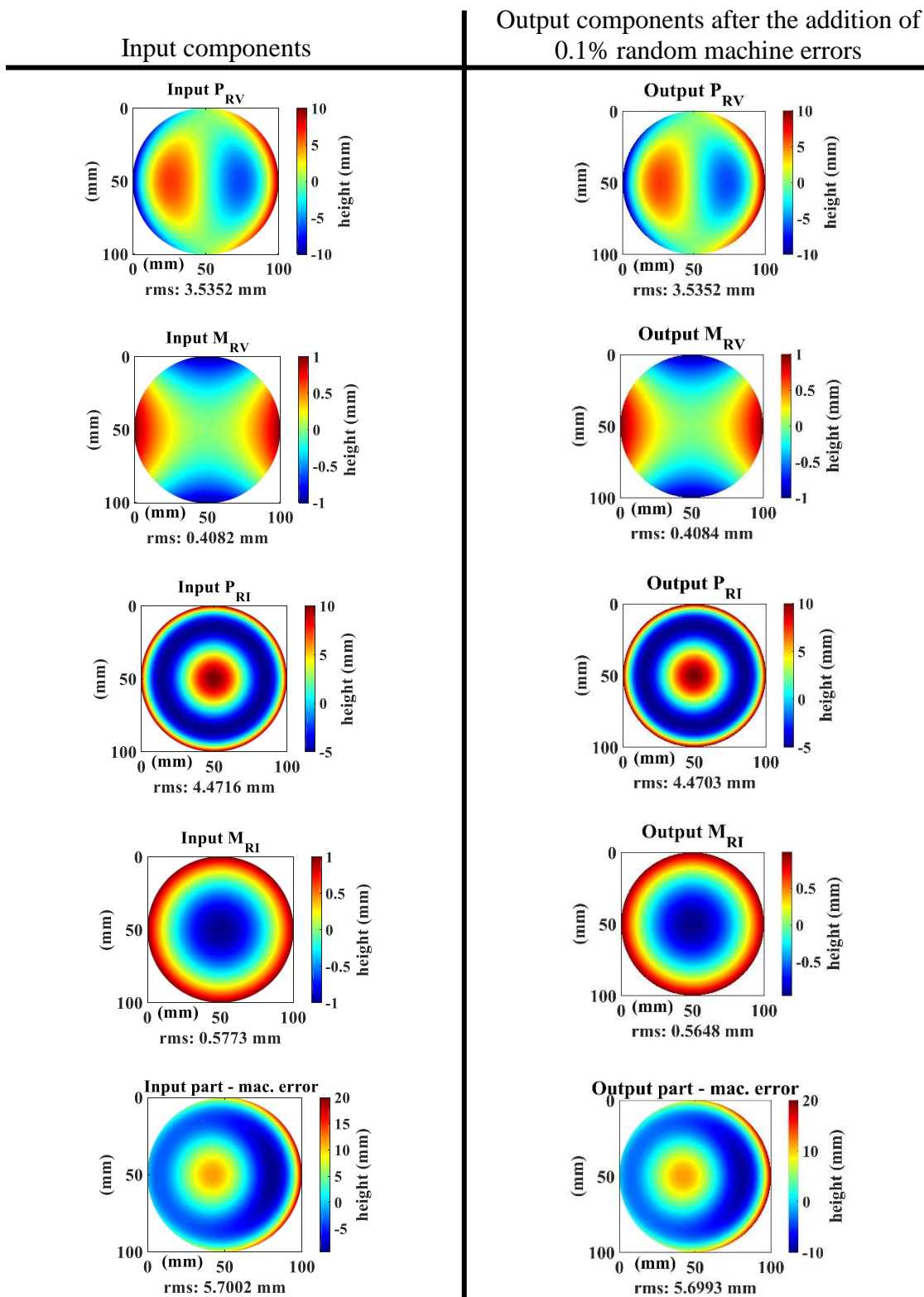
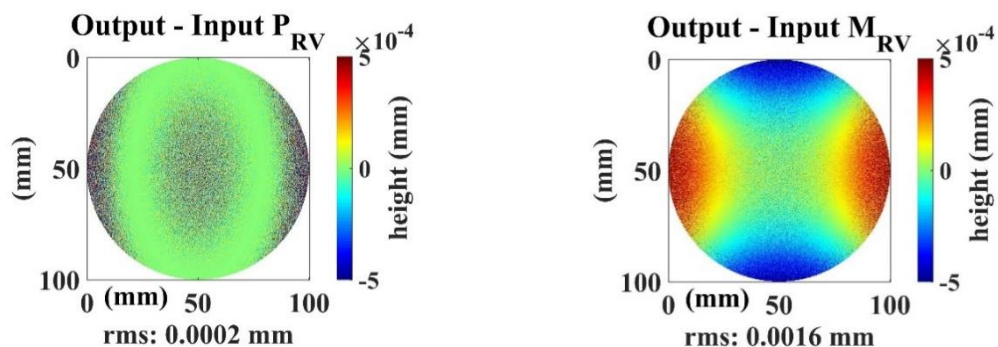


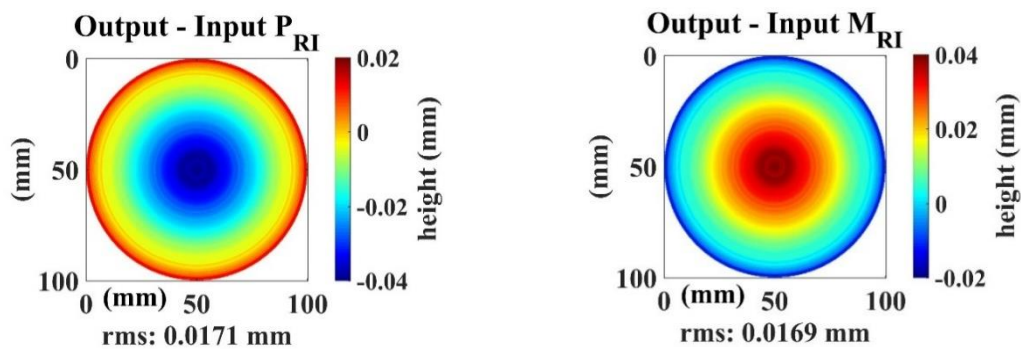
FIGURE B.5 Input components to the Shift-Rotation technique (*left*). Output components obtained after the addition of random z-axis machine errors with maximum amplitudes of 0.1% deviation from the nominal (*right*). (*right*).

Differences between output and input surface components after the addition of 0.1% random machine z-axis errors

Differences between rotationally varying components



Differences between rotationally invariant components



Difference between output and input best estimates of the part

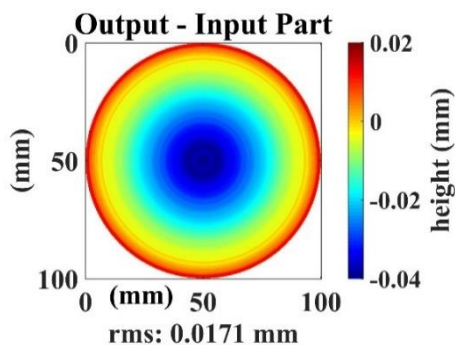


FIGURE B.6 Differences between output and input surface components after the addition of 0.1% random machine z-axis errors.

APPENDIX B.3 Influence of 0.01% Random Machine Z-axis Errors

The fourth set of added random machine z-axis errors had maximum amplitudes of 0.01% the nominal systematic machine errors. Figure B.7 (*left*) shows a simulated systematic machine error without random errors in the z-axis, while Figure B.7 (*right*) shows the resulting machine error after the addition of a random machine z-axis error with a maximum amplitude of 0.01% deviation from the nominal. These added errors were on a pixel-by-pixel basis and Figure B.7 shows they did not have a significant impact on the rms of the machine error.

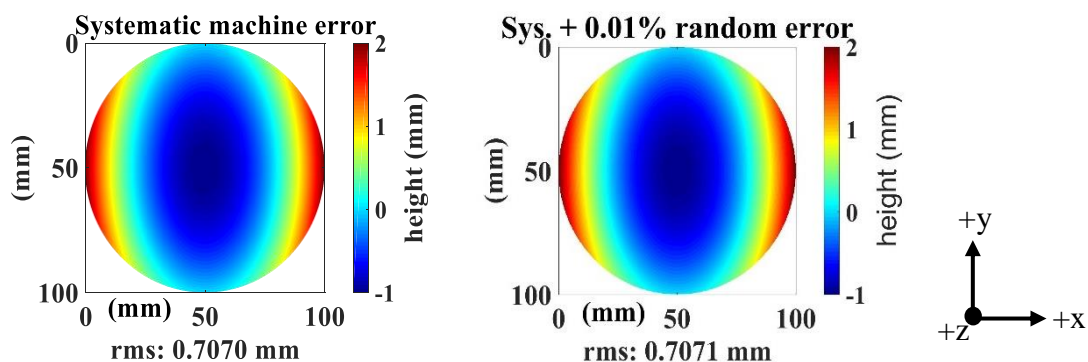


FIGURE B.7 Simulated systematic machine errors (*left*). The machine's systematic errors with a random component in the z-direction. The random errors have a maximum amplitude of 0.01% the nominal systematic error (*right*).

Similar to the previous chapter, to evaluate the effects of the added random errors on the error separation process, the Shift-Rotation error separations were carried out on a simulated part which included the systematic and random errors shown in Figure B.7 (*right*). After Shift-Rotation error separations of the part that included the random machine errors, the separated output components were compared to the input components and shown in Figure B.8.

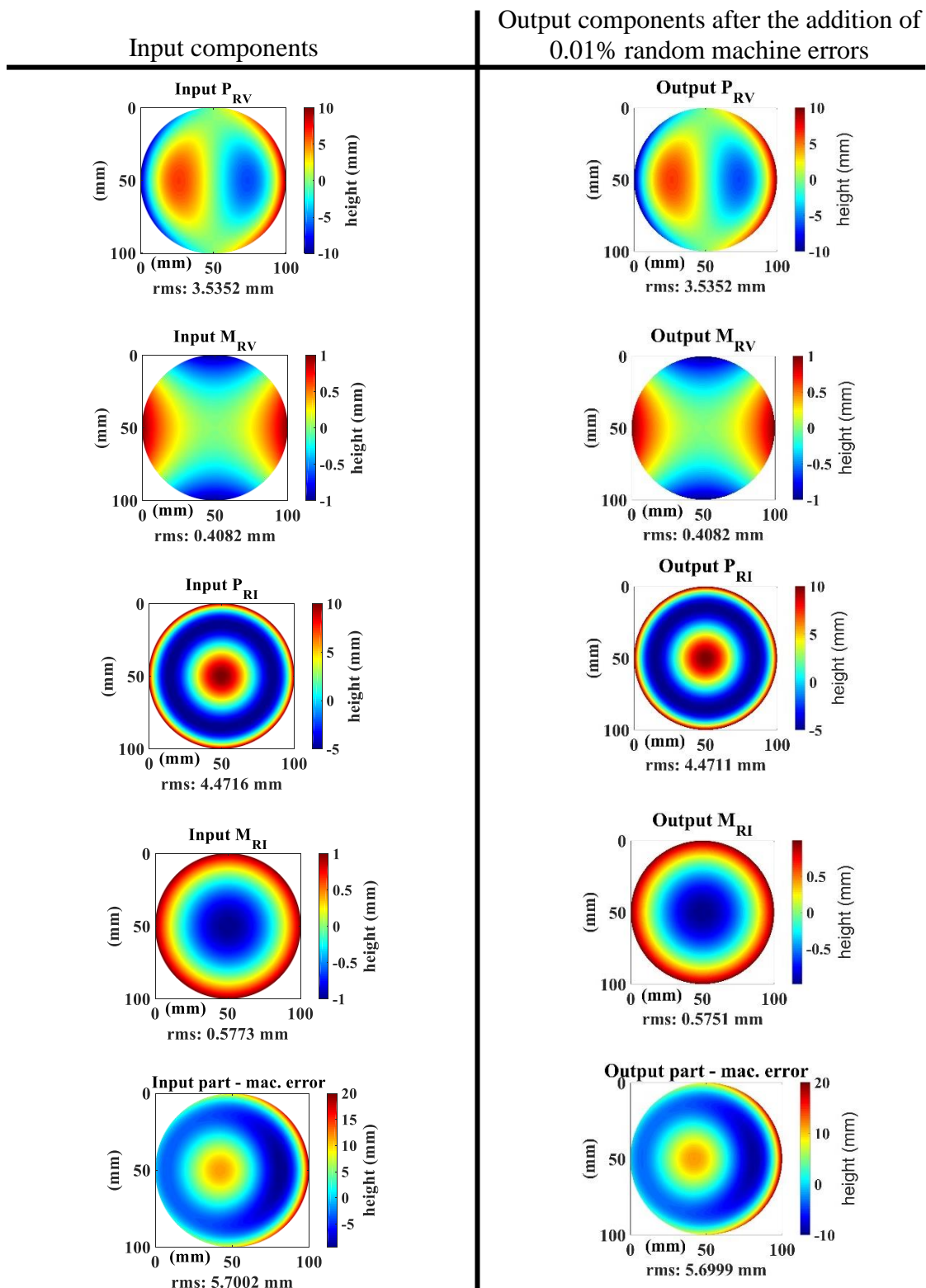
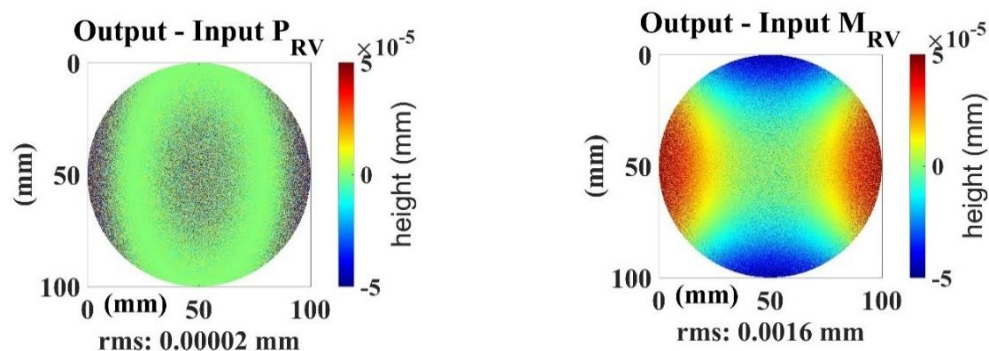


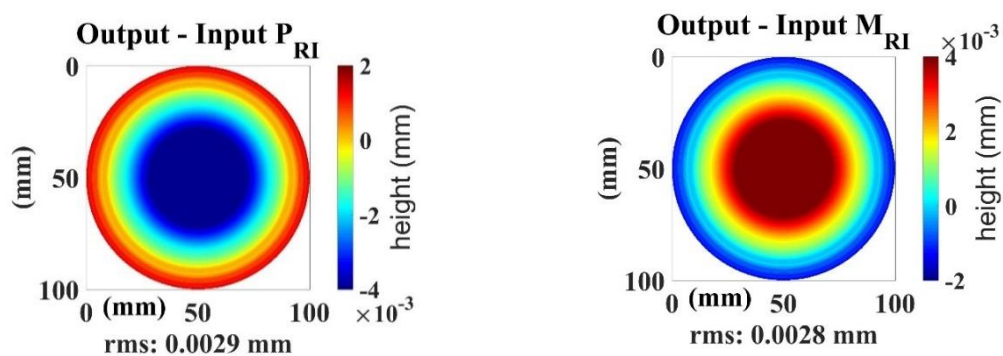
FIGURE B.8 Input components to the Shift-Rotation technique (*left*). Output components obtained after the addition of random z-axis machine errors with maximum amplitudes of 0.01% deviation from the nominal (*right*).

Differences between output and input surface components, after the addition of 0.01% random machine z-axis errors

Differences between rotationally varying components



Differences between rotationally invariant components



Difference between output and input best estimates of the part

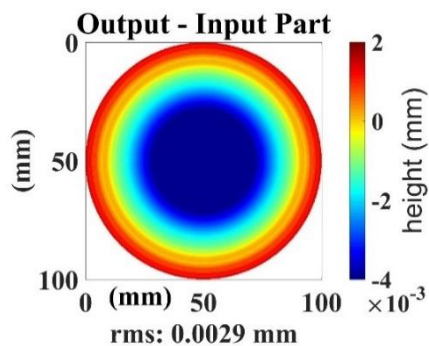


FIGURE B.9 Differences between output and input surface components, after the addition of 0.01% random machine z-axis errors.

APPENDIX C: ERROR SEPARATION OF ON-AXIS MSF ERRORS

In Chapter 4.2, the circular mid-spatial frequencies were comprised of one amplitude and frequency. In this chapter, the on-axis circular mid-spatial frequency error comprised multiple random frequencies and amplitudes. Figure C.1 (*left*) shows this simulated MSF error to be added to the simulated freeform surface in Figure C.1 (*right*).

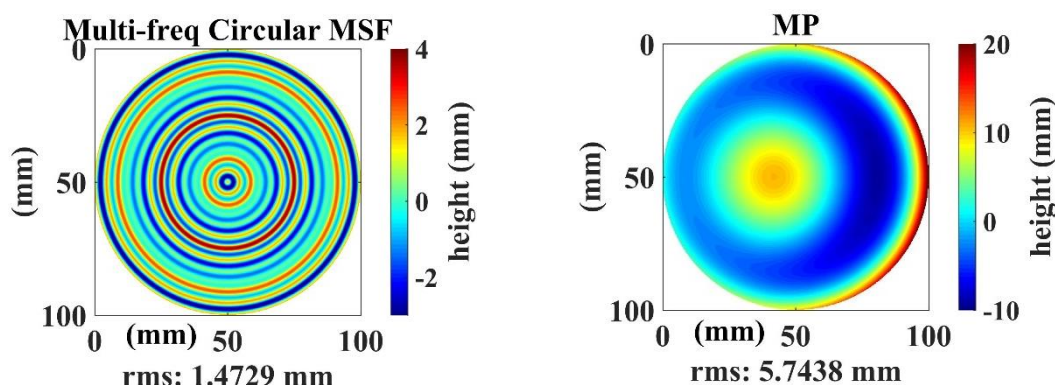


FIGURE C.1 A simulated on-axis circular mid-spatial frequency error comprised of multiple frequencies and amplitudes (*left*). The simulated freeform surface without mid-spatial frequency errors (*right*).

After adding the multiple-frequency circular MSF error in Figure C.1 (*left*) to the freeform surface in Figure C.1 (*right*), the resulting surface was shown in Figure C.2. These mid-spatial frequency errors can be noticed in the frequency domain, after calculating the PSD of a central horizontal profile extracted from Figure C.2. This PSD graph is shown in Figure C.3.

The PSD graph shows multiple mid-spatial frequency peaks around spatial frequencies of 0.16 cycles/mm and 0.2 cycles/mm which arise from the added MSF errors. Using the Shift-Rotation technique, the freeform height map in Figure C.2 was

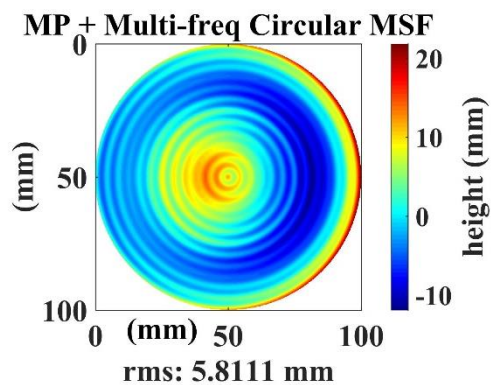


FIGURE C.2 The simulated freeform surface with multi-frequency circular mid-spatial frequency errors.

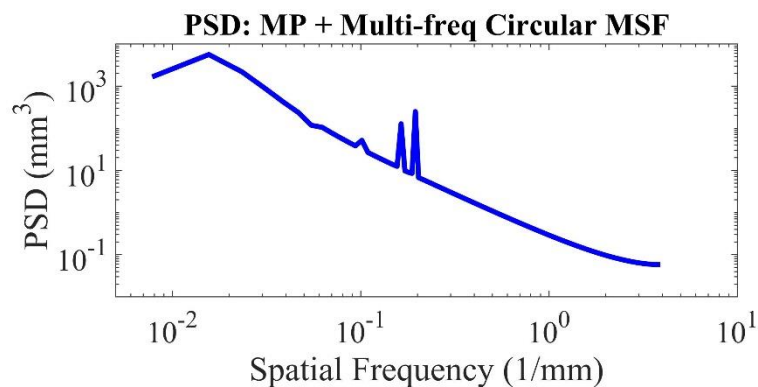


FIGURE C.3 The power spectral density of the central horizontal profile extracted from the freeform surface with multi-frequency circular mid-spatial frequency errors.

decomposed into four surface components: output P_{RV} , output M_{RV} , output P_{RI} , and output M_{RI} . Since the multi-frequency circular MSF errors were on-axis and rotationally invariant, they should show up as convolved with the RI components of the freeform surface.

The Shift-Rotation error separations of the surface in Figure C.2, into four components, are shown in Figure C.4.

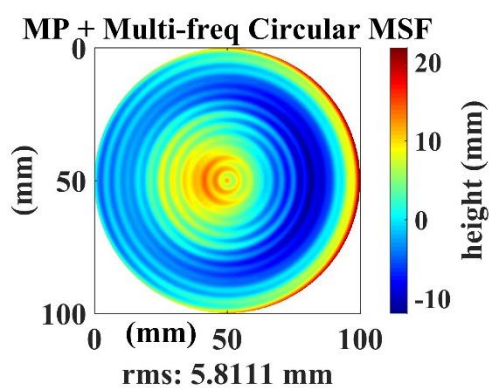
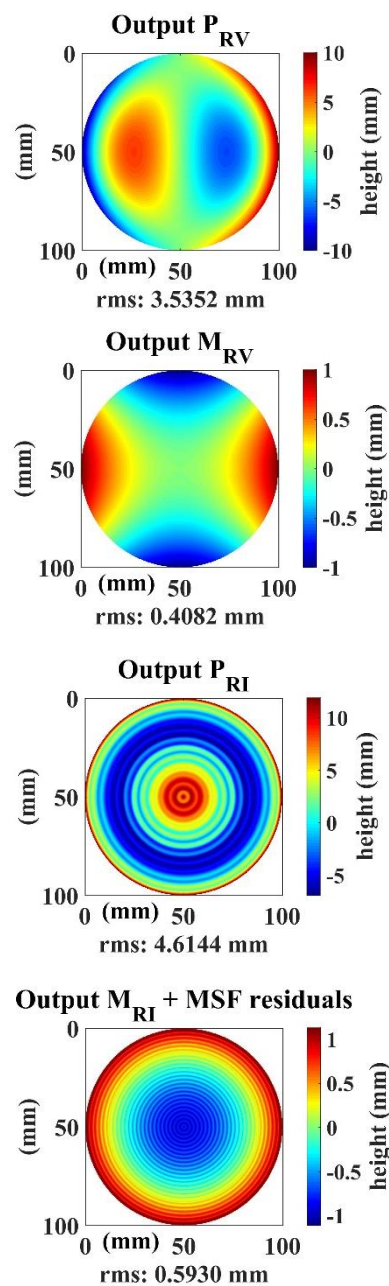
Freeform surface with multi-frequency circular MSF errors**Separated components**

FIGURE C.4 The freeform surface with multi-frequency circular mid-spatial frequencies (*left*). The Shift-Rotation separation of the freeform into four components (*right*).

Figure C.4 shows the decomposition of the freeform surface with on-axis multi-frequency MSF errors, into four surface components. The separated RV components are not influenced by the MSF errors since these MSF errors are comprised solely of rotationally invariant components. The RI components of the MSF errors are convolved with the separated RI component of the part. The residual MSF errors appear convolved with the RI component of the machine. If these types of multi-frequency circular MSF errors are present on a part, after error separations of the measurement data, the bulk of the multi-frequency circular MSF errors would correctly be separated as convolved with the rotationally invariant components of the part, while any residual MSF errors would be indistinguishable from the machine's RI errors. The amplitudes of these residuals can be

Multi-frequency circular MSF errors

Separated components

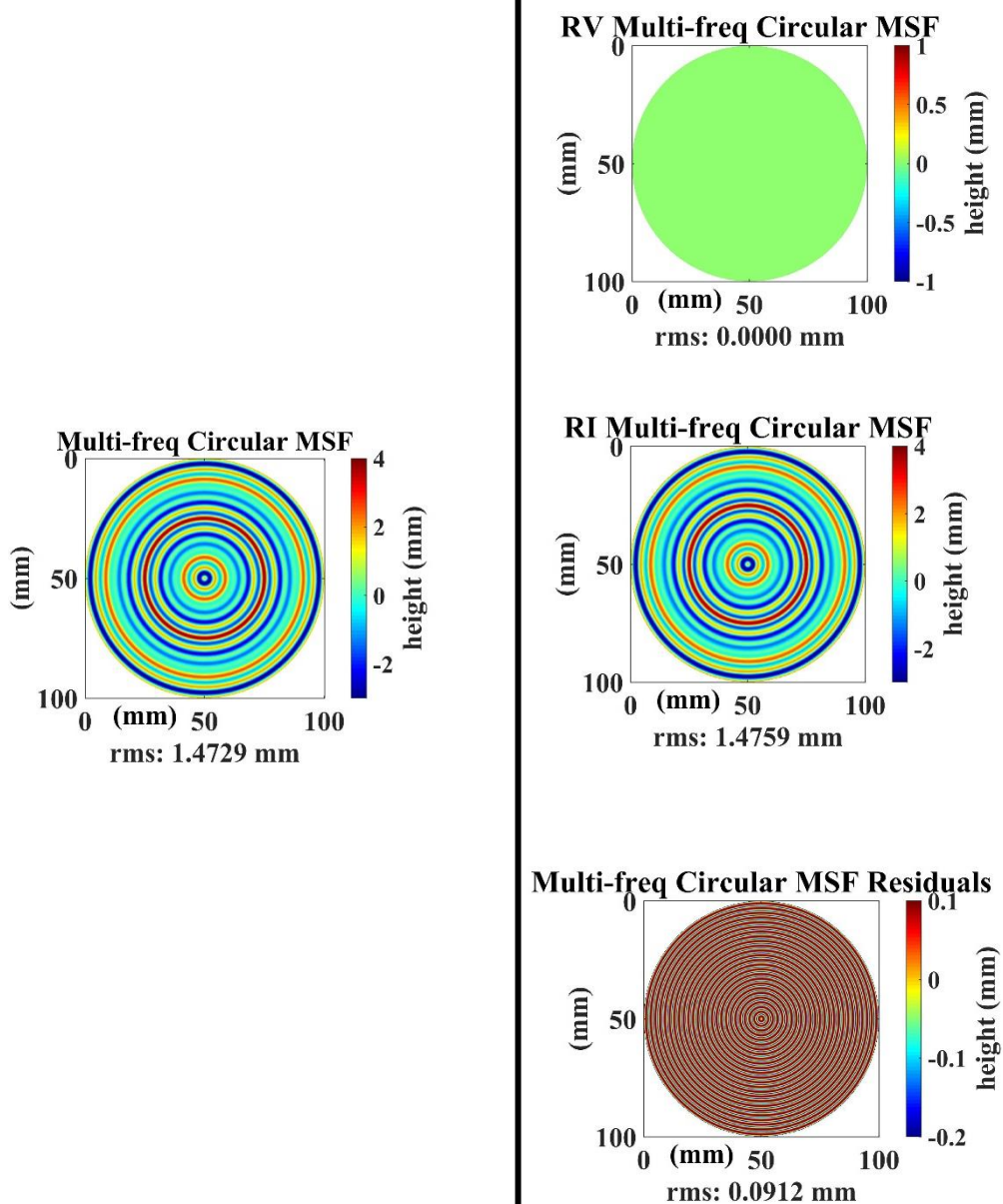


FIGURE C.5 Multi-frequency circular mid-spatial frequency errors (*left*). The Shift-Rotation separation of the mid-spatial frequency errors, into rotationally varying, rotationally invariant, and residual components (*right*).

observed after a Shift-Rotation error separation of only the multi-frequency circular MSF errors, as shown in Figure C.5.

APPENDIX D: ALTERNATE MEASUREMENT STRATEGY ON THE MAHR

In Chapter 5.3 and Chapter 5.4, a Cartesian measurement strategy was used to measure the freeform surface. In addition to this, a Polar measurement strategy was used to measure the freeform surface on the Mahr surface profiler. This alternative measurement strategy was for investigative and comparison purposes; the Shift-Rotation error separation was not applied to these measurement results.

Instead of parallel profiles (Cartesian measurement strategy), the Polar measurement model used multiple profile measurements across diameters on the freeform surface. A depiction of these profiles is shown in Figure D.1.

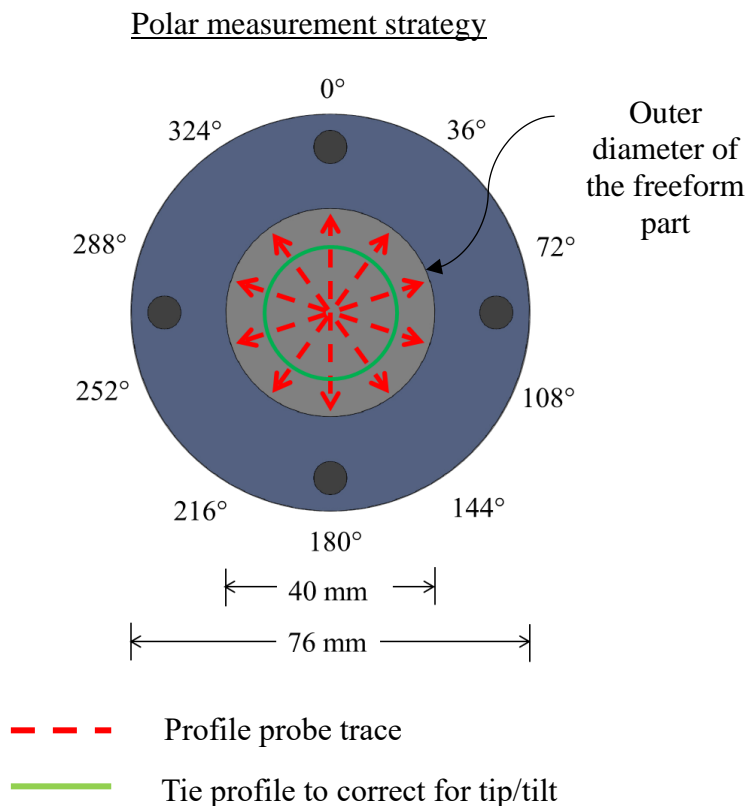


FIGURE D.1 Freeform surface measurement strategy on a Mahr surface profiler. A Polar measurement strategy that uses diametrical profile scans.

Ten profiles were measured across the freeform surface, from an arbitrary clocking angle of 0° to 324° in 36° increments. As Figure D.1 indicates, the profiles from 180° to 324° should, retrace the profiles from 0° to 144° respectively. This Polar measurement strategy has the advantage of ease of machine programming since the profile traces are of equal length and are about a common axis of rotation. On the other hand, one disadvantage of this strategy is the uneven data-point distribution. A high data density is observed around the axis of rotation, but this quickly tapers into a sparse data density towards the periphery of the part.

The Polar profiles were each 38-mm long, with point-coordinates taken every 1- μm , and measured at a probe speed of 1 mm/s. After the first profile at 0° was measured, the part was rotated clockwise by 36° and another 38-mm long profile was measured. This was repeated until the tenth profile at 324° was measured.

Between the measurements of the first and tenth profiles, tilt and piston changes could be introduced by stage drift. To correct for this, an azimuthal profile (with a 32-mm diameter) measurement was made. In this measurement, the probe contacted a point on the surface (16-mm from the rotation axis) and was set to measure the change in z -height while the part was rotated at $10^\circ/\text{s}$. From the expected intersection points between this azimuthal trace and the Polar profiles, the tilts of the Polar profiles were corrected to match those across the azimuthal profiles.

APPENDIX D.1 Measurement Results

Figure D.2 shows the ten Polar-model profiles without tilts. The profiles in Figure D.2 (*right*) are right-left retrace versions of those shown in Figure D.2 (*left*) since both sides show the same profiles measured from opposite directions.

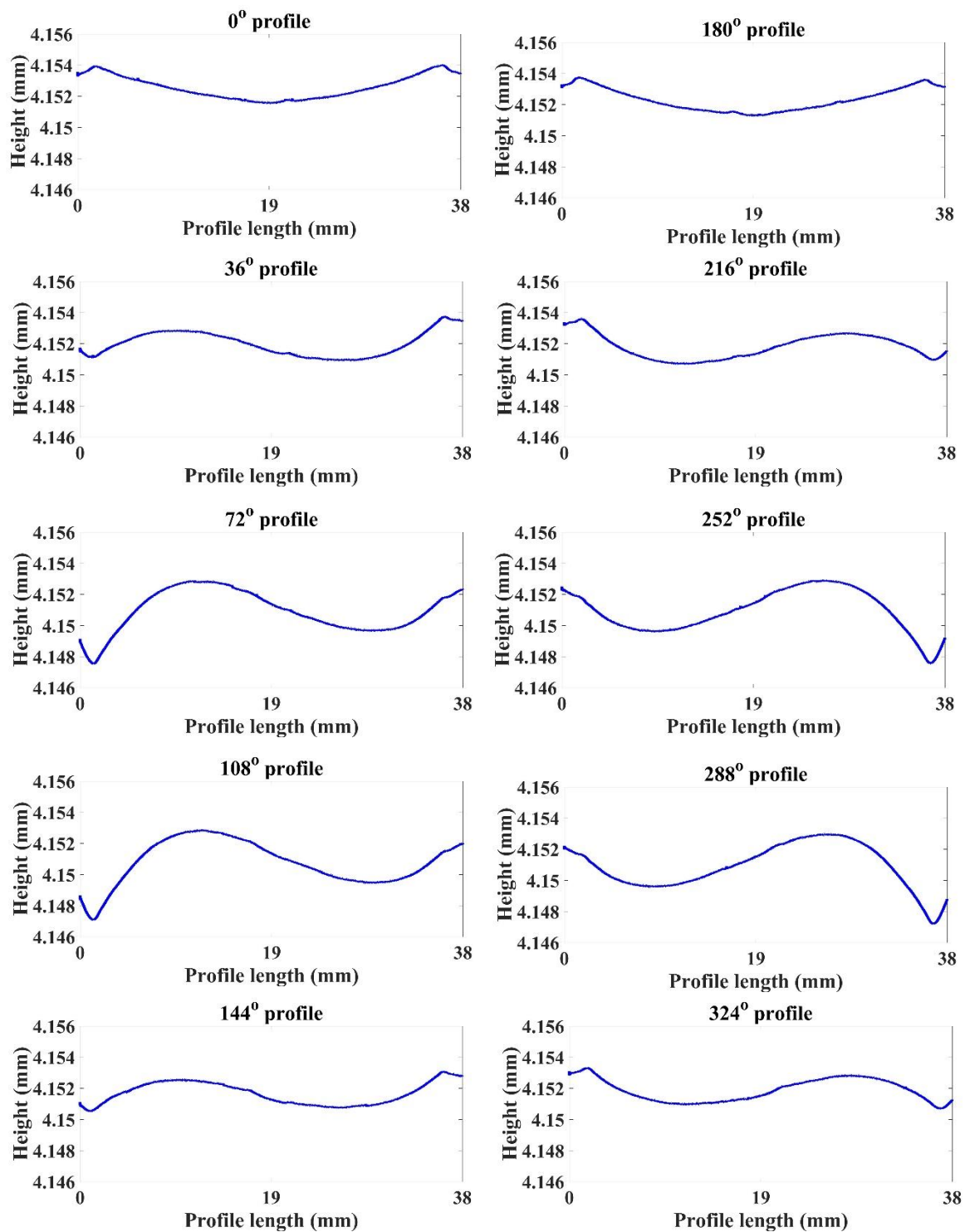


FIGURE D.2 Polar-model freeform surface profiles measured on the Mahr surface profiler.

Before generating a Zernike polynomial-fit surface from these profiles, their slopes

were corrected by using the azimuthal profile measurement shown in Figure D.3. This was a 32-mm diameter profile, measured quickly (36 seconds) to minimize the influence of stage drift. From the expected intersection points between this profile and the ten Polar profiles, the slopes from opposite points across the azimuthal profile were used to correct the slopes of the ten Polar profiles.

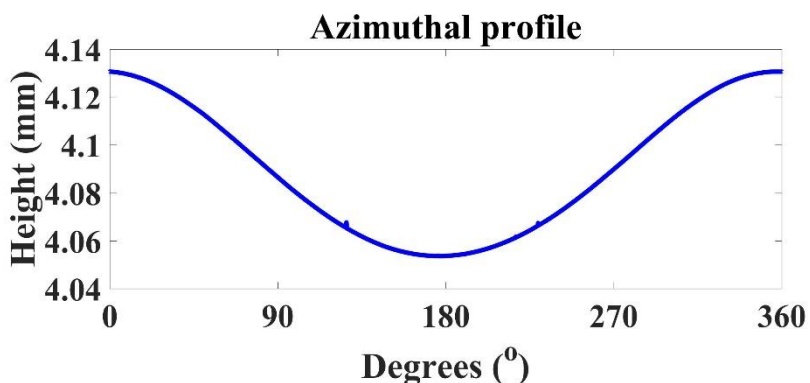


FIGURE D.3 Azimuthal profile measured to correct for tilt.

After slope-corrections of the ten profiles, the profiles from 180° to 324° were flipped to match the orientations of the 0° to 144° profiles. The 0.8-mm λ_c low-pass Gaussian filter (applied to the F-25 and previous Mahr freeform measurement results) was applied to these Polar-model measurement results. After filtering, twelve Zernike polynomials were fit to the Polar profiles and the fit was cropped down to the 35-mm clear aperture. The Zernike coefficients from this fit are listed in Table D.1, while the surface generated from these coefficients is shown in Figure D.4.

TABLE D.1 Zernike coefficients from a Zernike fit to the 10 Polar-model profiles.

	Zernike coefficients (nm)											
	Z (2, 0)	Z (2, -2)	Z (2, 2)	Z (3, -1)	Z (3, 1)	Z (3, -3)	Z (3, 3)	Z (4, -4)	Z (4, -2)	Z (4, 0)	Z (4, 2)	Z (4, 4)
Mahr: (Polar profiles)	16	853	2080	-2108	373	-29	83	61	30	-15	-157	48

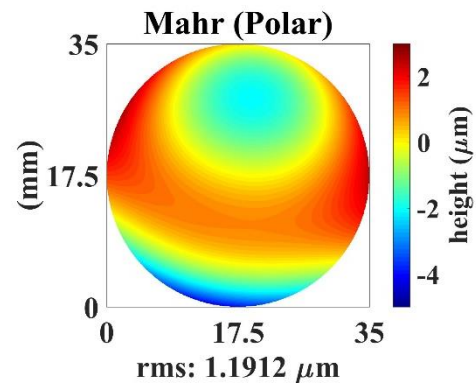


FIGURE D.4 Surface fit to the 10 Polar-model profiles measured on the Mahr profiler.

APPENDIX E: MATLAB CODES

```

%-----
%-----Program 1: Shift-Rotation Error Separation of Surface Measurement Maps-----

% A freeform surface was measured on a CMM in a predetermined order of
% part-rotations and translations. The test-surface was measured at 5 angular
% orientations (separated by 72 degrees) and at a translated position
% (1-mm translation distance).
% The purpose of this program is to separate these measurement results into
% contributions from the test-surface and those from the machine.

% The 'Shift' portion of the technique solves for the rotationally invariant (RI)
% components, while the 'Rotation' portion solves for the rotationally varying (RV)
% components. The simulation begins with the Rotation, and then proceeds to the Shift.
%-----
-----

% Separate the Rotationally Varying Components
clear all; close all; clc

% Input variables:
rotations = 5; % number of rotated positions of the test part
delta = 29; % Insert the translation distance (in pixels) here.

% Load the height maps from measurements made at multiple angular positions
load Freeform_F25_0_degrees.mat;
part_at_0_degrees = Freeform_F25_0_degrees*1000;
load Freeform_F25_72_degrees.mat;
part_at_72_degrees = Freeform_F25_72_degrees*1000;
load Freeform_F25_144_degrees.mat;
part_at_144_degrees = Freeform_F25_144_degrees*1000;
load Freeform_F25_216_degrees.mat;
part_at_216_degrees = Freeform_F25_216_degrees*1000;
load Freeform_F25_288_degrees.mat;
part_at_288_degrees = Freeform_F25_288_degrees*1000;

% Extract the RV components of the test-surface
c = cell (1,5); % place the 5 measurements in an array to find the average
c{1} = part_at_0_degrees; c{2} = part_at_72_degrees; c{3} = part_at_144_degrees;
c{4} = part_at_216_degrees; c{5} = part_at_288_degrees;
d = cat(3, c{:});

mean_part_rotate = nanmean(d,3); % average the rotated measurements to drop out
% the RV components of the rotated part.
outputPrv = part_at_0_degrees - mean_part_rotate; % the RV component of the

```

```

% test-surface

set (0,'DefaultFigureColormap', jet) % set the default colormap as "jet".

figure % plot the RV component of the test-surface
b=imagesc(outputPrv); set(b,'AlphaData',~isnan(outputPrv)); axis image; colorbar;
h = colorbar;ylabel(h,'height (\mum)','fontname','times new roman', 'fontsize', 36,
'FontWeight', 'bold'); % caxis([-5 3]);
set(gca,'fontname','times new roman','fontsize',36,'FontWeight','bold')
set(gca,'XTick',[0.5,length(outputPrv)/2,length(outputPrv)]) % sets x-axis tick locations
set(gca,'XTickLabel',{'0','17.5','35'}); % labels the x-axis
set(gca,'YTick',[0.5,length(outputPrv)/2,length(outputPrv)]) % sets y-axis tick locations
set(gca,'YTickLabel',{'35','17.5','0'});
RMS_z = (sqrt(nanmean(outputPrv(:).^2))); % Root-Mean-Square after ignoring the
% NaN values
RMS_z = sprintf('%0.4f', RMS_z); % display the rms with 4 decimal places
xlabel(['rms: ' num2str(RMS_z), ' \mum'],'fontsize',36);ylabel('(mm)','fontsize',36);
% inserts the rms value
title ('Part_R_V')

% Extract the RV components of the machine errors
mean_angle = 0:360/rotations:360-(360/rotations); % a vector containing the
% rotation angles

for i = 1 : length(mean_angle)
    machine_rotate (:,:,i) = imrotate(mean_part_rotate,mean_angle(i),'crop');

    one_machine_rotate = machine_rotate(:,:,i);
    one_machine_rotate(one_machine_rotate == 0) = NaN;
    RMS_machine_rotate(i) = sqrt(nanmean(one_machine_rotate(:).^2)); % calculate the
% rms of each machine_rotate map and store in an array
end

mean_machine_rotate = nanmean(machine_rotate,3); % average the rotated
% measurements along the 3rd dimension. This drops out the RV components
% of the machine.

outputMrv = mean_part_rotate - mean_machine_rotate; % The RV component of the
% machine errors

figure % plot the RV component of the machine errors
outputMrv(outputMrv == 0) = NaN;
b = imagesc(outputMrv); set(b,'AlphaData',~isnan(outputMrv)); axis image; colorbar;
h = colorbar;ylabel(h,'height (\mum)', 'fontname','times new roman', 'fontsize', 36,
'FontWeight', 'bold');
set(gca,'fontname','times new roman','fontsize',36,'FontWeight','bold')

```

```

set(gca,'XTick',[0.5,length(outputMrv)/2,length(outputMrv)]) % sets x-axis tick locations
set(gca,'XTickLabel',{'0','17.5','35'}); % this labels the x-axis
set(gca,'YTick',[0.5,length(outputMrv)/2,length(outputMrv)]) % sets y-axis tick locations
set(gca,'YTickLabel',{'35','17.5','0'});
RMS_z = (sqrt(nanmean(outputMrv(:).^2))); % Root-Mean-Square after ignoring the
% NaN values
RMS_z = sprintf('%0.4f', RMS_z); % display the rms with 4 decimal places
xlabel(['rms: ' num2str(RMS_z), '\mum'], 'fontsize',36); ylabel('(mm)', 'fontsize',36);
% inserts the rms value
title('Machine_R_V')

save outputPrv.mat; save outputMrv.mat

% Separate the Rotationally Invariant Components

% At least, 2 measurements are required: a measurement of the part in its initial position
% and a measurement after the part is translated by a known distance, delta.
% In these simulations, pads were added to the maps to depict translations.

load Freeform_F25_0_degrees_sheared_1mm.mat % load the height map of the
% translated measurement
sheared_part_at_0_degrees = Freeform_F25_0_degrees_sheared_1mm*1000;

Meas = mean_machine_rotate; % Depicts the height map after Prv and Mrv have
% been subtracted from a measurement of the part in its initial position.

Meas1 = padarray(Meas,[delta,0],NaN,'pre'); % Pads zero-valued columns to the
% left of Meas1. This simulates a translation of the part.

%% Remove RVs from the sheared measurement
mean_angle = 0:360/rotations:360-(360/rotations); % a vector containing the
% rotation angles

for i = 1:length(mean_angle)
    sheared_rotate(:,i) = imrotate(sheared_part_at_0_degrees,mean_angle(i),'crop');
    one_sheared_rotate = sheared_rotate(:,i);
    one_sheared_rotate(one_sheared_rotate == 0) = NaN;
    RMS_sheared_rotate(i) = sqrt(nanmean(one_sheared_rotate(:).^2)); % calculate the
    % rms of each sheared_rotate map and store in an array
end
mean_sheared_rotate = nanmean(sheared_rotate,3); % average the rotations of the
% sheared measurements along the 3rd dimension. This drops out the RV components of
% the sheared measurement.
sheared_RV_components = sheared_part_at_0_degrees - mean_sheared_rotate; % The
% RV component of the sheared

```

```

Meas2 = padarray(mean_sheared_rotate,[delta,0],NaN,'post'); % Pads zero-valued
columns to the left of RI component of the sheared measurement.

slope = (Meas2 - Meas1)/delta; % An approximate slope of the part. This difference
% drops out the machine's contributions.
l = (length(mean_machine_rotate));
g = (slope(ceil(l/2)-1:l-1,ceil(l/2))); % A profile from the approximate slope, from which
% the mean radial profile can be obtained

% Build the design matrix
H = zeros(length(g)); % H-sized matrix filled with zeros
idx = delta+1; % inserts '1' in the first row
n = length(g);
turnIdx = n * ( idx - 1 ) + 1; % 1 element after the end of the idx-1 row
H( idx:(n-1):turnIdx ) = -1;
H( turnIdx:(n+1):end ) = -1;
H = H.';

% Solve for the RI radial profile

% To solve for the radial profile by the noise-modified matrix, uncomment the next 3
% lines and comment the succeeding 2.

% H_noise = (H + 1.000000000001*eye(size(H))); % adds 1.000000000001 noise along
%% the diagonal
% f = H_noise\g;

H_pinv = H + 1*eye(size(H));
f = pinv(H_pinv)*g;

% Generate an RI surface from the RI radial profile
height = (f);
radius = length(f)-1;
[X,Y]=ndgrid(linspace(-radius,radius,l));
R=sqrt(X.^2+Y.^2);
outputPri = interp1(0:radius,f,R(:,:),'spline'); % The RI component of the test-surface
sd = find(isnan(mean_machine_rotate));
for i=(sd)
    outputPri(i) = NaN;
end

figure % plot the RI component of the test-surface
b = imagesc(outputPri); set(b,'AlphaData',~isnan(outputPri)); axis image; colorbar;
caxis([-0.004 .004]);
h = colorbar;ylabel(h,'height (\mum)','fontname','times new
roman','fontsize',36,'FontWeight','bold'); % caxis([-5 3]);

```

```

set(gca,'fontname','times new roman','fontsize',36,'FontWeight','bold')
set(gca,'XTick',[0.5,length(mean_machine_rotate)/2,length(mean_machine_rotate)])
set(gca,'XTickLabel',{'0','17.5','35'}); % this labels the x-axis
set(gca,'YTick',[0.5,length(mean_machine_rotate)/2,length(mean_machine_rotate)])
set(gca,'YTickLabel',{'35','17.5','0'});
RMS_z = (sqrt(nanmean(outputPri(:).^2)));
RMS_z = sprintf('%0.4f', RMS_z);
xlabel(['rms: ' num2str(RMS_z), '\num'], 'fontsize',36); ylabel('(mm)', 'fontsize',36);
title('Part_R_I')

```

```

best_est_part = outputPri + outputPrv; % The test-surface without the machine errors
outputMri = mean_machine_rotate - outputPri;
machine_errors = outputMri + outputMrv; % The machine error contributions

```

```

save outputPri.mat; save outputMri.mat
save best_est_part.mat; save machine_errors.mat

```

```

%-----
%-----End of Program 1-----

```

```

%-----
%-----Program 2: Monte Carlo uncertainty from the rotation angles-----

```

```

% This program estimates the standard uncertainty in the best-estimate of the surface.
% Input parameter: rotation angles.
clear all; close all; clc

```

```

load new_best_estimate_part_F25.mat; % Load the best-estimate height map
best_est_freeform_F25 = new_best_estimate_part_F25;

```

```

set (0,'DefaultFigureColormap', jet) % set the default colormap as "jet".

```

```

% An inner loop rotated the best-estimate to each uncertain angle. The average of these
% was subtracted from the best-estimate, and one possible outcome of the rotationally
% varying component was extracted.

```

```

% An outer loop repeated the inner loop multiple times and the possible outcomes from
% the iterations were stored in an array. The standard deviation down the
% array is calculated.

```

```

% Input variables:

```

```

rotations = 5; % number of rotated positions of the test-part
dev = 0.05; % upper/lower deviation from the mean rotation angle in degrees
iterations = 1000; % Number of times the Monte Carlo loop should be repeated.

```

```

nominal_angle = 0:360/rotations:360-(360/rotations); % lists out the angles of rotation
low_lim = nominal_angle - dev; % lower limit of the input parameter
up_lim = nominal_angle + dev; % upper limit of the input parameter

iterations = 1: iterations;

progressbar(0);progressbar('Prv Monte Carlo Simulation'); % Initialize and label the
single progress bar

tic
for ii = 1:length(iterations)
    for i = 1:length(nominal_angle)
        angle_uncert = low_lim + (up_lim - low_lim).*rand(1,length(nominal_angle));
        % Generates rotation angles. Each angle is a random number within low_lim
        % and up_lim. E.g., for a mean angle of 72, with limits +/- 1, a random number is
        % generated between 71 and 73.
        part_rotate(:,i) = imrotate(best_est_freeform_F25,angle_uncert(i),'bicubic','crop');
        % Depicts measurements of the part at each rotated position of the part.
        mean_part_rotate = mean(part_rotate,3); % average the rotated measurements,
        % part_rotate, along the 3rd dimension. This drops out the RV components of the
        % rotated part
        trial_Priv = best_est_freeform_F25 - mean_part_rotate; % One possible outcome of
        % the RV component of the part
        RMS_trial_Priv = sqrt(nanmean(trial_Priv(:).^2)); % rms of the Prv map
    end
    Prvnew_Uncert(:,ii) = trial_Priv;% Stacks the Prv from each loop into an array
    RMS_Privnew_Uncert(ii) = RMS_trial_Priv;% Stacks the Prv's rms from each loop in
    % an array

    % Code controlling the progress bar...
    progressbar(ii/(length(iterations))) % Update the progress bar

end
toc

% Convergence of the Monte Carlo.
tic
outputPrv = mean(Prvnew_Uncert,3); % Average of the Prv maps along the 3rd
% dimension.

RMS_outputPrv = sqrt(nanmean(outputPrv(:).^2)); % rms of the convergence
Std_Privnew_Uncert = (std(Prvnew_Uncert,0,3))/sqrt(length(iterations)); % computes
% the standard deviation down the array, along the third dimension
Std_Privnew_Uncert(Std_Privnew_Uncert == 0) = NaN;
toc

```

```
%% Plots of the convergence and standard uncertainty maps
```

```
figure%
b = imagesc(outputPrv); set(b,'AlphaData',~isnan(outputPrv)); axis image; colorbar
h = colorbar;ylabel(h,'height (\mum)','fontsize',36); % caxis([0 3]);
set(gca,'fontname','times new roman','fontsize',36,'FontWeight','bold')
set(gca,'XTick',[0.5,length(best_est_freeform_F25)/2,length(best_est_freeform_F25)])
set(gca,'XTickLabel',{'0','17.5','35'});
set(gca,'YTick',[0.5,length(best_est_freeform_F25)/2,length(best_est_freeform_F25)])
set(gca,'YTickLabel',{'35','17.5','0'});
RMS_outputPrv = (sqrt(nanmean(outputPrv(:).^2)));% Root-Mean-Square after ignoring
% the NaN values
RMS_outputPrv = sprintf('%0.4f', RMS_outputPrv); % display the rms with 4 decimal
% places
xlabel(['rms: ' num2str(RMS_outputPrv),' \mum'],'fontsize',36);
ylabel('(mm)','fontsize',36);
title('Monte Carlo P_R_V Convergence')
```

```
figure
b = imagesc(Std_Prnew_Uncert);
set(b,'AlphaData',~isnan(Std_Prnew_Uncert)); axis image; colorbar
h = colorbar;ylabel(h,'height (\mum)','fontsize',36); % caxis([0 0.002]);
set(gca,'fontname','times new roman','fontsize',36,'FontWeight','bold')
set(gca,'XTick',[0.5,length(best_est_freeform_F25)/2,length(best_est_freeform_F25)])
set(gca,'XTickLabel',{'0','17.5','35'});
set(gca,'YTick',[0.5,length(best_est_freeform_F25)/2,length(best_est_freeform_F25)])
set(gca,'YTickLabel',{'35','17.5','0'});
RMS_Std_Prnew_Uncert = (sqrt(nanmean(Std_Prnew_Uncert(:).^2))); % Root-Mean-
% Square after ignoring the NaN values
xlabel(['rms: ' num2str(RMS_Std_Prnew_Uncert),' \mum'],'fontsize',36);
ylabel('(mm)','fontsize',36);
title('u_R_o_t_A_n_g_l_e','fontsize',36)
```

```
Convergence_Rot_Angle = outputPrv; save Convergence_Rot_Angle.mat
Uncertainty_Rot_Angle = Std_Prnew_Uncert; save Uncertainty_Rot_Angle.mat
```

```
%-----
%-----End of Program 2-----
```

```
*****
```

```
%-----
%-----Program 3: Monte Carlo uncertainty from a translating axis of rotation-----
```

```
% To depict the out of centering that might occur during rotations, NaN
% pads were added around the best-estimate map. The out-of-center uncertainty
% was applied to the test part but not the machine error components
```

```

clear all; close all; clc
load new_best_estimate_part_F25.mat; % Load the best-estimate height map
best_est_freeform_F25 = new_best_estimate_part_F25;

set (0,'DefaultFigureColormap', jet) % set the default colormap as "jet".

% Input variables:
rotations = 5; % number of rotated positions of the part
dev = 0; % upper/lower deviations from the mean rotation angle
Out_of_Cen = 1; % the max. radial out-of-center deviation in pixels
iterations = 1000; % number of times the Monte Carlo loop should be repeated

nominal_angle = 0:360/rotations:360-(360/rotations); % lists out the angles of rotation
low_lim = nominal_angle - dev; % lower limit of the input parameter
up_lim = nominal_angle + dev; % upper limit of the input parameter

Out_of_Cen = 1:1:Out_of_Cen;

iterations = 1 : iterations;

best_est_freeform_F25_pad = padarray(best_est_freeform_F25,[length(Out_of_Cen),
length(Out_of_Cen)], NaN);

progressbar(0);progressbar('Prv Monte Carlo Simulation'); % Initialize and label the
single progress bar

tic
for ii = 1:length(iterations)
    for i = 1:length(nominal_angle)
        angle_uncert = low_lim + (up_lim - low_lim).* rand (1,length(nominal_angle));
        % generates rotation angles where each angle is a random number within
        % low_lim and up_lim.

        Out_of_Cen_left = round(rand.*(2*length(Out_of_Cen))); % generates a random
        % integer between 1 and Out_of_Cen
        partPad = padarray(best_est_freeform_F25,[0,Out_of_Cen_left],NaN,'pre'); % Pad
        % the left side of the part with NaN
        partPad = padarray(partPad,[0,(2*length(Out_of_Cen) - Out_of_Cen_left)],...
        NaN, 'post'); % Pad the right side of the part with NaN

        Out_of_Cen_up = round(rand.*(2*length(Out_of_Cen))); % generates a random
        % integer between 1 and Out_of_Cen
        partPad = padarray(partPad,[Out_of_Cen_up,0],NaN,'pre'); % Pad the top side of the
        % part with NaN
        partPad = padarray(partPad,[0,(2*length(Out_of_Cen) - Out_of_Cen_up),0],...
        NaN, 'post'); % Pad the bottom side of the part with NaN
    end
end

```

```

part_rotate(:, :, i) = imrotate(partPad, angle_uncert(i), 'bicubic', 'crop'); % depicts
% measurements of the part at each rotated position of the part.
mean_part_rotate = mean(part_rotate, 3); % average the rotated measurements along
% the 3rd dimension. This drops out the RV components of the rotated part.
trial_Priv = best_est_freeform_F25_pad - mean_part_rotate; % the RV component of
% the test surface
trial_Priv(isnan(trial_Priv)) = 0; % replaces empty cells with zero
RMStrialPrv = sqrt(nanmean(trial_Priv(:).^2)); % rms of the Prv map
trial_Priv(trial_Priv == 0) = NaN;
end
Prvnew_Uncert_O_o_C(:, :, ii) = trial_Priv; % Stacks the Prv from each loop into an
% array
Prvnew_Uncert_O_o_C(Prvnew_Uncert_O_o_C == 0) = NaN;
RMS_Privnew_Uncert_O_o_C(ii) = RMStrialPrv; % Stacks the Prv's rms from each
% loop into an array

% Code controlling the progress bar...
progressbar(ii/(length(iterations))) % Update the progress bar

end
toc

tic
mean_Priv_O_o_C = nanmean(Prvnew_Uncert_O_o_C, 3); % Monte Carlo convergence
RMS_mean_Priv_O_o_C = sqrt(nanmean(mean_Priv_O_o_C(:).^2));
Prvnew_Uncert_O_o_C(isnan(Prvnew_Uncert_O_o_C)) = 0;
Std_Privnew_Uncert_O_o_C = (std(Prvnew_Uncert_O_o_C, 0, 3))/sqrt(length(iterations));
Std_Privnew_Uncert_O_o_C(Std_Privnew_Uncert_O_o_C == 0) = NaN;
toc

xmin = 1 + length(Out_of_Cen); ymin = 1 + length(Out_of_Cen);
xwidth = length(best_est_freeform_F25) - 1;
yheight = length(best_est_freeform_F25) - 1;
mean_Priv_O_o_C = imcrop(mean_Priv_O_o_C, [xmin ymin xwidth yheight]);
Std_Privnew_Uncert_O_o_C = imcrop(Std_Privnew_Uncert_O_o_C, [xmin ymin...
xwidth yheight]);
mean_part_rotate = imcrop(mean_part_rotate, [xmin ymin xwidth yheight]);
mean_Priv_O_o_C(sd) = NaN; Std_Privnew_Uncert_O_o_C(sd) = NaN;
%% Plots of the convergence and standard uncertainty
figure % plot of the best estimate (average) of the 1000 Prv trials
b = imagesc(mean_Priv_O_o_C); set(b, 'AlphaData', ~isnan(mean_Priv_O_o_C));
axis image; colorbar; % caxis([-1 1]);
h = colorbar; ylabel(h, 'height (\num)', 'fontname', 'times new roman', 'fontsize', 36, ...
'FontWeight', 'bold'); caxis([-5 3]);
set(gca, 'fontname', 'times new roman', 'fontsize', 36, 'FontWeight', 'bold')

```

```

set(gca,'XTick',[0.5,length(best_est_freeform_F25)/2,length(best_est_freeform_F25)])
set(gca,'XTickLabel',{'0','17.5','35'});
set(gca,'YTick',[0.5,length(best_est_freeform_F25)/2,length(best_est_freeform_F25)])
set(gca,'YTickLabel',{'35','17.5','0'});
RMS_mean_Priv_O_o_C = (sqrt(nanmean(mean_Priv_O_o_C(:).^2)));
RMS_mean_Priv_O_o_C = sprintf('%0.4f', RMS_mean_Priv_O_o_C);
xlabel(['rms: ' num2str(RMS_mean_Priv_O_o_C), ' \mum'],'fontsize',36);
ylabel('(mm)','fontsize',36);
title('Monte Carlo Convergence')

```

figure

```

b=imagesc(Std_Privnew_Uncert_O_o_C);
set(b,'AlphaData',~isnan(Std_Privnew_Uncert_O_o_C)); axis image; colorbar;
h = colorbar;ylabel(h,'height (\mum)','fontname','times new roman', 'fontsize',36,...
'FontWeight','bold'); % caxis([-5 3]);
set(gca,'fontname','times new roman','fontsize',36,'FontWeight','bold')
set(gca,'XTick',[0.5,length(best_est_freeform_F25)/2,length(best_est_freeform_F25)])
set(gca,'XTickLabel',{'0','17.5','35'});
set(gca,'YTick',[0.5,length(best_est_freeform_F25)/2,length(best_est_freeform_F25)])
set(gca,'YTickLabel',{'35','17.5','0'});
RMS_Std_Privnew_Uncert_O_o_C =
(sqrt(nanmean(Std_Privnew_Uncert_O_o_C(:).^2)));
RMS_Std_Privnew_Uncert_O_o_C = sprintf('%0.4f',...
RMS_Std_Privnew_Uncert_O_o_C);
xlabel(['rms: ' num2str(RMS_Std_Privnew_Uncert_O_o_C), ' \mum'],'fontsize',36);
ylabel('(mm)','fontsize',36);
title('u_R_o_t_A_x_i_s','fontsize',36)

```

Convergence_Rot_Axis = mean_Priv_O_o_C; save Convergence_Rot_Axis.mat

Uncertainty_Rot_Axis = Std_Privnew_Uncert_O_o_C_resized;

save Uncertainty_Rot_Axis.mat

```

%-----
%-----End of Program 3-----

```

```

%-----
%-----Program 4: Monte Carlo uncertainty from the translation distance-----

```

clear all; close all; clc

load new_best_estimate_part_F25.mat;

best_est_freeform_F25 = new_best_estimate_part_F25;

set(0,'DefaultFigureColormap',jet) % set the default colormap as "jet".

```

% Input variables:
rotations = 5; % number of rotated positions of the part
iterations = 1000; % Number of times the Monte Carlo loop should be repeated.

mean_angle = 0:360/rotations:360-(360/rotations); % lists out the angles of rotation

for i = 1:length(mean_angle)
    part_rotate(:,i) = imrotate(best_est_freeform_F25,mean_angle(i),'crop');
    one_part_rotate = part_rotate(:,i);
    RMS_part_rotate(i) = sqrt(nanmean(one_part_rotate(:).^2));
end

mean_part_rotate = mean(part_rotate,3); % average the rotated measurements along the
% 3rd dimension. This drops out the RV components of the rotated part.
outputPrv = best_est_freeform_F25 - mean_part_rotate; % the RV component of the part

iterations = 1:iterations;
delta_spread = randi([26,32],[1,length(iterations)]); % edit the upper and lower limits of
% the translation distance in randi([mini,maxi]

progressbar(0);progressbar('Monte Carlo Simulation: translation distance'); % Initialize
% and label the single progress bar

tic
for i = 1:length(iterations)
    delta = delta_spread(i);

    Meas1_ri = padarray(mean_part_rotate,[0,delta],NaN,'pre'); % Pads zero-valued
    % columns to the left of Meas1. This helps simulate a translation of the part.

    Meas2_ri = padarray(mean_part_rotate,[0,delta],NaN,'post'); % padding to the right
    %side of the part depicts a translation to the left

    slope = (Meas2_ri - Meas1_ri)/delta; % approximate slope of the part. This difference
    % drops out the machine's error contributions

    l = (length(best_est_freeform_F25));
    g = (slope(ceil(l/2),ceil(l/2):l));

    % Build the design matrix:
    H = zeros(length(g));
    idx = delta+1;
    n = length(g);
    turnIdx = n * ( idx - 1 ) + 1;
    H( idx:(n-1):turnIdx ) = -1;
    H( turnIdx:(n+1):end ) = -1;

```

```

H = H.';
H = H + 1*eye(size(H));
f = pinv(H)*g; % calculate f from the pseudo-inverse
% Generate an RI surface from the RI radial profile
height = (f);
radius = length(f)-1;
[X,Y]=ndgrid(linspace(-radius,radius,1));
R=sqrt(X.^2+Y.^2);
outputPri = interp1(0:radius,f,R(:,:),'spline');
sd = find(isnan(mean_part_rotate));
for ii=(sd)
    outputPri(ii) = NaN;
end

outputPri_array(:,i) = outputPri;
% Code controlling the progress bar...
progressbar(i/(length(iterations))) % Update the progress bar
end
toc

Convergence_Trans_Dist = mean(outputPri_array,3);
Uncertainty_Trans_Dist = (std(outputPri_array,0,3))/sqrt(length(iterations));

save Convergence_Trans_Dist.mat
save Uncertainty_Trans_Dist.mat
%-----
%-----End of Program 4-----

```